

Progressive failure analysis of continuous fiber additive manufacturing composites

Juan Sebastián León Becerra

Tesis para Optar al Título de Doctor en Ingeniería Mecánica

Director

Octavio Andrés González Estrada

PhD en Ingeniería Mecánica y de Materiales

Codirectores

Alberto David Pertuz Comas

PhD en Ingeniería Mecánica

William Pinto Hernández

PhD en Ingeniería Mecánica

Universidad Industrial de Santander

Facultad de Ingenierías Físico-mecánicas

Escuela de Ingeniería Mecánica

Doctorado en Ingeniería Mecánica

Bucaramanga

2022

Acknowledgments

I want to thank Professor Octavio Andrés González-Estrada for his kind guidance and support in every stage of this thesis. To my co-advisors, Professors William Pinto Hernandez and Alberto David Pertuz, my sincere gratitude for their time and collaboration, particularly Prof. Pinto, to guide the material modeling of polymers and additive manufacturing advice. To prof. Pertuz his experimental and fractographic knowledge was beneficial. I am deeply grateful for the support of Jorge Guillermo Diaz, a post-doctoral researcher at the Universidad Industrial de Santander, for the fruitful conversations and ideas we share.

To Universidad Industrial de Santander for providing financial support in this research and funding for publishing and attending conferences. To the School of Mechanical Engineering for providing the funding for the materials employed in this research. Thanks to Tecnoparque Nodo Bucaramanga for the supporting material and the permission to use their equipment.

My profound gratitude to Dr. Juan Pablo Correa Aguirre and Prof. Miguel Angel Hidalgo Salazar, with whom I collaborate at GITEM in Universidad Autónoma de Occidente, to develop the last part of this thesis. Their knowledge of polymers and the dynamic behavior of materials reshape my understanding of composite materials. Finally, to all GIEMA members: professors, researchers, alumni, and students, their contributions played a significant role in my professional development. Thanks to Jeffrey Corzo, my Ph.D. adventure friend, we share ideas, coffee breaks, office space. Also, Carlos Florez, Carlos Barrera, Nohemy Gomez, and Robin Delbart, with whom days were enjoyable. Thanks to my family and my girlfriend for their emotional support when things did not go well and for celebrating with me when they do.

Content

Introduction.....	18
1. Objectives	22
1.1 General Objective	22
1.2 Specific Objectives	22
2. Literature Review.....	23
2.1 Fused Filament Fabrication of Continuous Fibers.....	28
2.2 3D Printing of Continuous Fiber-Reinforced Additive Manufacturing Composites.....	31
2.3 Material Modeling and Simulation of Fiber-Reinforced Additive Manufacturing Composites	35
2.4 Mechanical Testing and Failure Mechanisms in Fiber-Reinforced Additive Manufacturing Composites.....	40
3. Methodology.....	44
3.1 Materials and Fabrication Method	45
3.2 Characterization Techniques and Equipment	46
3.2.1 Tensile, Compressive, Shear, and Flexural Testing.....	46
3.2.2 Scanning Electron Microscopy	47
3.2.3 Dynamic Mechanical Analysis	48
3.3 Experimental Setup.....	50
3.4 Analysis, Validation and Verification.....	51

4. Material Modeling	51
4.1 Geometrical and Mechanical Characterization of the Composed Regions	52
4.2 Infill Regions	54
4.2.1 Honeycomb or Hexagonal	55
4.2.2 Rectangular or Grid.....	56
4.2.3 Triangular.....	57
4.3 Solid and Shell Regions	57
4.4 Fiber-Reinforced Region	58
4.5 Stiffness Characterization: Numerical, Micromechanical, and Experimental.....	60
4.5.1 Analytical Formulation	61
4.5.2 Two Steps Numerical Homogenization	65
4.6 Strength Characterization.....	71
4.7 Ply and Laminate Mechanics	74
4.8 Performing Volume Average Stiffness Method	77
4.9 Conclusions of the material modeling	81
5. Manufacturing Process Parameters Effects on the Mechanical Response.....	82
5.1 Data-Driven Models.....	84
5.1.1 Decision Trees	86
5.1.2 Linear Regression	86
5.1.3 Support Vector Machines	87
5.1.4 Gaussian Process Regression.....	88
5.1.5 Artificial Neural Networks	88

5.2 Experimental Methodology and Design of Experiments.....	90
5.3 Experimental Results and Model Comparison	92
5.4 Fractographic and Microstructural Analysis.....	106
5.4.1 Generalities of Fractographic Analysis.....	106
5.4.2 Short Fiber Composite Fractography.....	115
5.4.3 Fractographical Analysis and Process Parameters Influence.....	117
5.5 Conclusions of the effects of process parameters	133
6. Progressive Damage Model, Validation, and Verification	135
6.1 Damage Models	136
6.1.1 Damage Model Definition	140
6.1.2 Simple Instant Material Stiffness Reduction	141
6.1.3 Matzenmiller Damage Model	142
6.1.4 Maimí Damage Model	146
6.2 Verification and Validation.....	146
6.3 Experimental Validation and Experimental Stress Analysis	149
6.4 Results.....	155
6.4.1 Numerical Results.....	155
6.4.2 Experimental Results	158
6.4.3 Model Validation	160
6.5 Source of Errors	165
6.6 Dynamic Mechanical Analysis	167
6.7 Conclusions of the progressive damage.....	172

7. Conclusions and Future Work	173
7.1 General Conclusions	173
7.2 Impact of the Research and Contributions.....	175
7.3 Future Work	175
7.4 List of Publications and Conference Participations	176
7.4.1 Published Journal Papers	176
7.4.2 Conferences.....	177
References.....	179
Annexes.....	202
Appendix A. Python script for composite mechanics and data repository.	202
Appendix B. Histograms of the selected micrographs.....	203
Appendix C. Markforged materials datasheet	205
Appendix D. List of symbols by chapter	207

Table List

Table 1 Principal FFF process parameters, typical values, and effects in parts	34
Table 2 Experimental test needed to characterize a composite	50
Table 3 Infill density range for different patterns	54
Table 4 Micromechanical models and the associated property	63
Table 5 Properties of the bulk and homogenized matrix	67
Table 6 Nomenclature and used values for the VAS method.....	78
Table 7 Information of the three factors DOE.....	91
Table 8 Specimen distribution in DOE.....	91
Table 9 Composite reinforced layers for each block and their volumetric fraction	92
Table 10 Results for continuous carbon fiber reinforced Nylon White.....	93
Table 11 Longitudinal and transversal modulus comparison: experimental and micromechanics formulation for various samples	97
Table 12 Suggested values of the engineering constants in continuous FRAM composites.....	99
Table 13 Processed data for strength comparison for FRAM.....	100
Table 14 Retrieved back-calculated constants for FRAM.....	101
Table 15 Comparison of the models performance for stiffness and strength prediction	102
Table 16 Printing parameters of the tested specimens for damage characterization	150
Table 17 Summary of the material properties used in the numerical model	156
Table 18 Damage material properties, fiber tensile, compressive, matrix tensile, and compressive for fiberglass and Kevlar.....	158
Table 19 Printing specifications for surface and dynamic mechanical analysis.....	167

Figure List

Figure 1 Classification of manufacturing techniques used for polymer matrix composites.....	25
Figure 2 Principal types of failures in laminated composites	27
Figure 3 Microstructure of an AM composite part (cCF/PA): a) overall thickness view, b) zoom in a low interlayer adhesion, c) zoom in a low inter bead adhesion	28
Figure 4 Schematic of additive manufacturing methods: a) FDM, b) SLA, c) SLS, d) direct ink printing (DIP).....	29
Figure 5 Schematic of FFF of thermoplastics and fiber-reinforced thermoplastics: a) single extruder, b) multi-material single extruder with mixing phase, c) double head extruder.....	30
Figure 6. A cross-sectional view of a FRAM carabiner in the software Eiger	32
Figure 7 Part orientations in the building bed: 1) flat, 2) on-edge, 3) upright, 4) inclined.....	33
Figure 8 Scheme of the PSPP paradigm in FRAM parts	39
Figure 9 Material regions with the identification, characterization, and analysis stages	45
Figure 10 Markforged 3D printer with filament case	46
Figure 11 Tensile test on the MTS Bionix 370.02 machine	47
Figure 12 Vesga Tecscan SEM in Tecnoparque Nodo Bucaramanga.....	48
Figure 13 DMA module TA RSG-2 and air chiller unit.....	49
Figure 14 DMA test chamber view of an Onyx sample	49
Figure 15 Cross-section view of FRAM.....	52
Figure 16 Cross-section schematic view of a typical FRAM component	54
Figure 17 Different RUC of infill patterns with three infill densities following values in Table 1	55

Figure 18 Serial and parallel arrangement of a unit cell of a composite schematic	61
Figure 19 Two-step homogenization process schematics of a transverse section of a composite filament spool.....	66
Figure 20 Mesh of the porous matrix, numerical homogenization model.....	67
Figure 21 View of the selected image sizes: a) big square region, b) medium size region, c) small region	68
Figure 22 Histogram of the different spool images: a) big-sized region, b) medium size, c) small size	68
Figure 23 Cross-section view of fiberglass reinforced AM part a) general view and magnifications, b) area where printed beads are not overlapped c) area with overlapped printed beads	69
Figure 24 Extracted micrographs and histograms of a fiberglass FRAM part	71
Figure 25 Resultants acting on a plate: a) forces per unit length, b) moments per unit length	76
Figure 26 Areas of artificial intelligence	84
Figure 27 Representation of a simple regression tree	86
Figure 28 Schematic of the artificial neural network.....	89
Figure 29 Pareto charts of the standardized effects for the angle, fiber content, and their interaction in the: a) stiffness, and b) strength.....	94
Figure 30 Interval graphs for: a) stiffness (MPa) and, b) strength (MPa) of on-edge specimens with 95% CI for mean.....	95
Figure 31 Normal residue plots for: a) stiffness, b) strength	96
Figure 32 Predicted vs. true response in stiffness (GPa) for the: a) best data-driven and, b) micromechanical models	104

Figure 33 Predicted vs true response in strength (MPa) for the: a) best data-driven and, b) micromechanical models	104
Figure 34 Absorbed energy per area in (MPa.mm) for: a) flat printed, b) on-edge printed	105
Figure 35 Surface of a FRAM part by SEM.....	107
Figure 36 Fractographic surface of 90° UD carbon fiber reinforced nylon white.....	108
Figure 37 400X zoom to a 90° UD carbon fiber reinforced nylon white	109
Figure 38 Buckling failure specimen at low magnification, the rectangles show the magnification zones	110
Figure 39 Compression failure zone of the buckle specimen:a) in low magnification, b) high magnification.	111
Figure 40 Tension failure zone of buckled specimen showing fiber and matrix damage	111
Figure 41 High magnification tension failure zone showing microscopic fiber features	112
Figure 42 Pure tension failure fractographic surface of a 0° UD carbon FRAM	113
Figure 43 400X magnification of a 0° UD carbon FRAM	114
Figure 44 Fracture surface fiber close up magnification (3000X) of 0° carbon UD FRAM.....	115
Figure 45 SEM of a failed short carbon fiber reinforced AM composite (Onyx)	116
Figure 46 SEM surface of Onyx: a) 382X, b) 793X magnification.....	117
Figure 47 Schematic of the failure topologies of AM composites: a) 0°, b) 45°, c) 90° fiber alignment.....	118
Figure 48 Wide view of a flat printed 0° FRAM 2-16 layers	119
Figure 49 Flat printed 0° FRAM 4-16 layers reinforcements.....	120
Figure 50 Flat printed 0° FRAM with four reinforcement layers.....	121
Figure 51 Flat printed 0° FRAM 6-16 showing detachment of the fiber region	122

Figure 52 Tensile breakage fractography in a flat printed 0° FRAM 6-16.....	123
Figure 53 Flat printed 0° FRAM 6-16 showing fiber pull-out	123
Figure 54 Flat printed FRAM with 45° and two layers of reinforcement	124
Figure 55 Matrix cracking in a flat printed 45° carbon FRAM (4 carbon layers).....	125
Figure 56 Ply splitting in a flat printed 45° carbon FRAM	126
Figure 57 Macroscopic view of a flat printed FRAM with 2 layers reinforcement at 90°	127
Figure 58 Extensive crack growth in a 90° reinforcement FRAM	128
Figure 59 Fractography of a six-layered flat printed 90° reinforced FRAM.....	129
Figure 60 Fractography of a six-layered flat printed 90° reinforced FRAM at 565X	130
Figure 61 Fractography of an on-edge printed reinforced FRAM with 55 reinforced layers.....	131
Figure 62 Wide view of a 70 layer on-edge printed reinforced FRAM.....	132
Figure 63 Fractography of a 70 layer on-edge printed reinforced FRAM, zoom on reinforcement region	132
Figure 64 Ply detachment on a 70 layer on-edge printed reinforced FRAM.....	133
Figure 65 Failure planes of the composite lamina	144
Figure 66 Schematic of the verification and validation process	148
Figure 67 Pseudo-cyclic test used for damage characterization in the Bionix 370.02 MTS	150
Figure 68 Reference and current configuration for DIC treatment. Coordinates of the subsets are shown as red crosses, notation at the bottom is used throughout the rest of the chapter.....	152
Figure 69 Open hole specimen speckle pattern viewed from the DIC camera.....	155
Figure 70 Stiffness degradation in a tensile test for 3D printed laminates: a) L1 [0 ₂ /90 ₄] _s , b) L8 [0 ₁ /+40 ₄ /0 ₁ /2] _s	157

Figure 71 Average stress-strain response of the open hole laminates: a) Onyx reinforced with Kevlar, b) Onyx reinforced with fiberglass	159
Figure 72 In-plane shear field of processed DIC strain results in Ncorr	160
Figure 73 Shear strain comparison at F=2500N, both results are close to zero: a) numerical model, b) experimental with DIC technique.....	161
Figure 74 Normal strain in the x direction at F=2500N: a) numerical technique, b) experimental DIC.....	162
Figure 75 Validation using normal strain in the y direction at F= 2500N: a) numerical model, b) experimental.....	163
Figure 76 Tensile matrix damage for a 0° layer in a fiberglass open hole specimen	164
Figure 77 Shear damage for a 0° layer in a fiberglass open-hole specimen.....	165
Figure 78 3D printed Onyx with different printing directions.....	167
Figure 79 Strain wave and stress wave for a dynamical test as a function of time	168
Figure 80 DMA results for a flat Onyx specimen, Tg is indicated in the graph.....	169
Figure 81 Effect of printing direction in the storage modulus of Onyx.....	170
Figure 82 Effect of printing direction in the loss modulus of Onyx.....	171
Figure 83 Effect of printing direction in the tan(δ) of Onyx	171

Appendices

	Page.
Appendix A. Python script for composite mechanics and data repository.....	202
Appendix B. Histograms of the selected micrographs.....	203
Appendix C. Markforged materials datasheet.....	205
Appendix D. List of symbols by chapter.....	207

Abbreviations list

The abbreviations are presented next, a complete list of symbols by chapter can be found in Appendix D. List of symbols by chapter

ANOVA: Analysis of variance

AM: Additive manufacturing

CAM: Cylindrical assemblage model

CDM: Continuum damage mechanics

CLPT: Classical laminate plate theory

CZM: Cohesive zone model

DoE: Design of experiments

DIC: Digital Image Correlation

DMA: Dynamic mechanical analysis

DSC: Differential scanning calorimetry

FE: Finite element

FFF: Fused filament fabrication

FRAM: Fiber-reinforced additive manufacturing

FRP: Fiber reinforced polymers

LOM: Laminated object manufacturing

LS: Lattice structure

MPDM: Material property degradation method

PDA: Progressive damage analysis

PFA: Progressive failure analysis

PSPP: Process-Structure-Property-Performance

PMC: Polymer matrix composite

PMM: Periodic microstructure model

RVE: Representative volume element

RUC: Representative unit cell

SEM: Scanning electron microscope

SL: Stereolithography

SLS: Selective Laser Sintering

TGA: Thermo gravimetric analysis

VAS: Volume average stiffness

VCCT: Virtual crack closure technique

Resumen

Título: Análisis de la falla progresiva en materiales compuestos de manufactura aditiva reforzados con fibras continuas.*

Autor: Juan Sebastian Leon Becerra.**

Palabras Clave: fabricación por filamento fundido, compuestos termoplásticos, mecánica del daño continuo, caracterización mecánica.

Descripción: La presente tesis doctoral describe el análisis de la falla progresiva en materiales compuestos de manufactura aditiva. Se propone como objetivo implementar y validar un modelo de daño progresivo para piezas de materiales compuestos de fabricación aditiva a la vista de los parámetros de proceso, mecanismos de falla, y microestructura generada. Inicialmente parte de un estudio a las propiedades mecánicas más relevantes para el diseño como son la rigidez y la resistencia usando para ello una formulación del método de promediado volumétrico de rigideces junto con expresiones micromecánicas que considera la topología de la parte. En seguida, la tesis aborda el estudio de diferentes parámetros de proceso que afectan las propiedades mecánicas, se hace énfasis en la dirección de impresión, la fracción volumétrica de fibras y en el ángulo que estas forman con la carga, basado en un enfoque con diseño de experimentos. Estos resultados son comparados con modelos basados en datos evaluando su desempeño. En un tercer tiempo la tesis analiza la falla de estos materiales al considerar laminados de varias capas en diferentes ángulos para ello propone el uso de la mecánica de daño continuo explorando su aplicabilidad a estos materiales con niveles altos de porosidades y defectos iniciales. La validación del modelo es realizada mediante la técnica de correlación digital de imágenes en un ensayo tipo open hole. Los resultados muestran que: considerar las propiedades de las estructuras celulares mejoran la exactitud de los modelos, los modelos micromecánicos predicen de mejor manera que los modelos basados en datos las propiedades mecánicas, es posible aplicar un modelo basado en la mecánica del daño continuo a piezas de fabricación aditiva, se establecen los mecanismos de daño en materiales compuestos de manufactura aditiva, y finalmente se ahonda en los factores que pueden contribuir al error en la validación.

* Tesis doctoral.

** Facultad de Ingenierías Fisicomecánicas. Escuela de Ingeniería Mecánica. Director: Octavio Andrés González Estrada, Doctor en Ingeniería Mecánica y de Materiales. Codirectores: Alberto David Pertuz Comas, Doctor en Ingeniería Mecánica. William Pinto Hernández, Doctor en Ingeniería Mecánica.

Abstract

Title: Progressive failure analysis of continuous fiber additive manufacturing composites.*

Author: Juan Sebastian León Becerra.**

Keywords: fused filament fabrication, thermoplastic composites, continuum damage mechanics, mechanical characterization.

Description: This doctoral thesis describes the progressive failure analysis in additive manufacturing composite materials. The objective is to implement and validate a progressive damage model for additive manufacturing composite parts given the process parameters, failure mechanisms, and generated microstructure. Initially, it starts by studying the most relevant mechanical properties for the design, such as stiffness and strength, using a formulation of the volumetric averaging stiffness method and micromechanical expressions that consider the topology of the part. Next, the thesis addresses the study of different process parameters that affect the response to mechanical properties. Emphasis is placed on the printing direction, the volumetric fraction of fibers, and the angle they form with the load, being carried out based on an approach using the design of experiments. The results were compared with data-driven models and evaluated their performance. In a third phase, the thesis analyzes the failure of these materials when considering laminates of several layers at different angles. For this, it proposes using continuous damage mechanics, exploring its applicability to these materials with high levels of porosities and initial defects. The model validation is performed by digital image correlation in an open hole test. The results show that: considering the properties of cellular structures improves the accuracy of the models, micromechanical models predict mechanical properties better than models based on data, it is possible to apply a model based on the continuum damage mechanics to parts of additive manufacturing, the mechanisms of damage in composite materials of additive manufacturing are established, and finally, the thesis delves into the factors that can contribute to the error in the validation.

* Doctoral thesis.

** Faculty of Physicomechanical Engineering. School of Mechanical Engineering. Advisor: Octavio Andrés González Estrada, Doctor in Mechanical and Materials Engineering. Coadvisors: Alberto David Pertuz Comas, Doctor in Mechanical Engineering. William Pinto Hernández, Doctor in Mechanical Engineering.

Introduction

Industries like manufacturing, aerospace, automotive, marine, and oil and gas employ composite materials. Composites are made with at least two distinct materials: matrix and reinforcement. Some conventional composite manufacturing technologies include hand or spray layup, filament winding, injection molding, compression molding, and resin transfer molding. These methods mentioned above are labor-intensive and typically require molds made of metallic materials such as aluminum or steel. Moreover, mold fabrication is costly due to design, testing, and tooling requirements. On the other hand, additive manufacturing (AM) processes can overcome the limitations of conventional composite fabrication methods. Besides considering the most suitable composite material, selecting the appropriate manufacturing method considers the cost, volume production capabilities, material compatibility, and quality of the finish parts.

The quality of the component establishes in the way it conforms to the intended performance. This performance results from the specific material properties and the structure generated. Thus, this paradigm can be viewed as a process-structure-property-performance (PSPP) relationship.

The process-structure relation is understood by the simulation and experimental validation of thermal history, geometry and tolerance assessment, flow profile, and associated variables. The jump from structure-property is made by quantitative and analytical methods such as micromechanics, whereas for the composite property performance, the preferred analysis is the layer-wise plates theories or a numerical approach such as the finite element (FE) method. FE simulations are widely used to perform stress analysis of fiber reinforced polymers (FRP)

composites. However, the pre-failure, onset of failure, and post-failure behaviors need to be modeled for a complete analysis of FRP composites.

In traditional manufacturing methods, the PSPP flow is being cleared, but for AM, because it is a recently introduced composite processing technology, it needs to be studied to determine its PSPP flow. Therefore, allowing engineers to design parts, predict their performance, and select the manufacturing parameters to give the intended performance.

The thesis hypothesis is that the process parameters of AM have significant effects on the mechanics of composite materials, which can be predicted using a continuum damage mechanics model. Those effects are in their stiffness, strength, and failure mechanisms.

For testing this statement, the thesis proposes the following approach: first, a division of a composite part is made based on the topology, encountering three regions: solid polymeric regions, cellular infill regions, and composite regions (continuous fiber-reinforced). Then, it analyzes separately the behavior of each region in independence of the other ones. Finally, the regions are integrated in a volumetric average stiffness method for stiffness and linear characterization and a layer-wise ply modeling for the strength and non-linear behavior.

The proposed solution relies on available theories, equations and models combining them in manner to explain the mechanical response of AM composite parts. The thesis gives the models description, their restrictions, and asses their performance based on the verification and validation metrics to determine if whether or not is applicable to fused filament fabricated composite parts.

The present thesis performs an analysis of mechanical characterization and damage behavior of fiber-reinforced additive manufacturing (FRAM) materials. It is limited to polymeric

matrices. However, it could be helpful in metal matrix composites or even ceramic if certain conditions are met. Continuum theory is used, thus, indicating that the discrete nature of some defects is ignored in the deterministic models being tested. Loads being investigated are static in most of the research. However, temporal effects and dynamical properties were discussed in chapter six as the dynamic mechanical analysis (DMA) test's significance.

This introductory chapter presented the baseline of the current composite AM issues posing the problem statement and giving the hypothesis. Later, the objectives of the current work are outlined, which have guided the development of this thesis. Chapter two presents the state-of-the-art AM composites, focusing on AM polymer matrix composites. The process parameters of the components are outlined, and their effects on mechanical properties are described. Another critical issue is damage and failure, which is also described in the chapter. Finally, it concludes by stating the relation between materials and processes in properties, performance, and failure behavior.

Chapter three is dedicated to the methodology. It helps state the general workflow of the thesis as well as the equipment, materials, procedures, and techniques used in the investigation.

Section one of chapter four presents the modeling strategy for FRAM, and it is based on previous mechanics of composite theories such as orthotropic elasticity and classical laminate plate theory (CLPT). However, one of the main features of AM is the capability of producing hollow parts in sections of lattice structures, so the thesis incorporates in section two of chapter four the mechanical models of lattice structures (LS) into consistent modeling for FRAM composites. They are divided into triangular, hexagonal, and rectangular honeycombs. Next section is dedicated to the characterization of the reinforcement phase. It starts with a physical and microstructural characterization in which the SEM images are analyzed. Then, numerical and analytical

homogenization methods are used to explain and predict the mechanical properties of FRAM and obtain the representative volume element (RVE) size of the reinforcing phase. Finally, conclusions show differing infill types and densities can respond differently in FRAM composites, also it compares how well the current micromechanics formulations are applied to assess novel polymer composite parts.

Chapter five presents the result of chapter four in a design of experiments lens. Here, the influence of process parameters in a design of experiments (DoE) methodology and a data-driven model is analyzed. It also introduces the SEM micrographs and a qualitative description and fractography of FRAM parts.

Chapter six is dedicated to the damage model. First, it presents the different formulations of the progressive damage analysis and gives the damage initiation and evolution criteria. The second section presents the numerical implementation, and the third section presents the experimental setup necessary for the damage characterization and validation of the model. Next, the model results are compared with experimental data taken from a full-field tensile test. The chapter continues by showing the influence of temperature and temporal features of the system to better acknowledge their role in the mechanical response of the FRAM parts. It concludes with a discussion of the advantages, capabilities, and drawbacks of the current work. Finally, general conclusions of the thesis are given, and future work for exploring ideas for the next generation.

1. Objectives

The objectives proposed by the thesis are presented below.

1.1 General Objective

To implement and validate a progressive damage model in additive manufacturing composite materials fabricated from fused filament fabrication, finding the manufacturing parameters effects in the mechanical behavior and the failure mechanisms.

1.2 Specific Objectives

- To develop a material modeling strategy for characterizing the stiffness and strength of a composite laminate from fused filament fabrication, considering the layup configuration, the fiber orientation, and the geometrical dimensions of each region.
- To determine the representative volume element size suitable for applying the progressive damage model, discriminating the behavior of each material region.
- To find the effects of the fabrication parameters such as printing direction, fiber reinforcement type, fiber angle, infill type, and the infill density into the stiffness, strength, and total energy dissipated using a design of experiment approach.
- To perform the tensile, compressive, and or shear test finding the mechanical properties of stiffness, strength experimentally, and the damage parameters used in the damage model, comparing the results with the predicted model.

- To perform a fractographic and microscopy analysis of the tested samples, showing the failure mechanisms and the relationship with the state of damage, the load, and the manufacturing process.
- To validate the numerical damage model through open hole type specimens, using a strain field measurement technique such as digital image correlation.

2. Literature Review

Composite materials are formed by at least two different materials: the reinforcing and the bonding phases. Polymer matrix composites (PMC) are composite materials that are made by mixing different polymer resins.. Some common uses for composites include aircraft, automotive, building, electronic, military and space applications. PMC's are lightweight, strong and can be produced in many different colors. However, PMC materials have not yet been implemented in all applicable fields.

Polymeric matrices can be thermoset or thermoplastic. Examples of thermoset polymer resins used in PMC's include epoxy, polyester, polyurethane and polyesters such as polyethylene terephthalate (PET). These resins are mixed together to create different PMC compositions.

Thermoplastic polymers are basically high-performance plastics that are found in many home and commercial appliances. The word 'thermoplastic' refers to heat and pressure acting upon plastic forming it into a material that can be molded into various shapes. There are many different types of thermoplastic materials. Some common thermoset plastics include nylon, PLA and PEEK.

These materials are also used to make many types of durable plastic and composite materials. These applications include engineering, transportation and healthcare applications. For example, thermoplastic polymers are used to make heat-resistant components in ovens, stoves and microwaves. Additionally, thermoplastic polymers are used to make plastic food containers for storage, transportation and, make medical equipment such as prosthetic limbs and artificial skin.

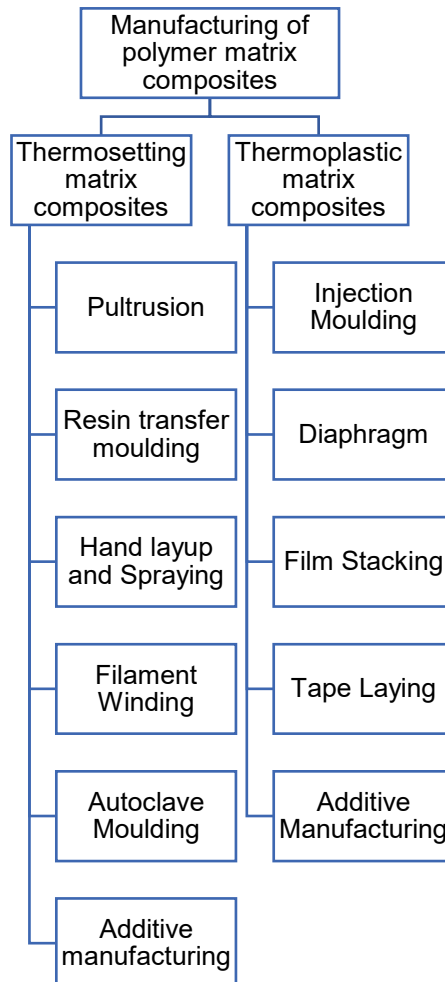
Thermoplastic polymers are durable and easy to mold. They're also non-explosive, non-corrosive, non-allergenic and non-toxic. In addition, thermoplastic polymers can be easily tinted and have a good color retention ability. Due to their versatility, thermoplastic polymers have many compelling uses.

Although their properties have yet to be fully explored, thermoplastic polymers hold many interesting possibilities for future products. These versatile materials have applications in both industry and medicine- allowing for the production of high-quality, cost effective materials capable of withstanding harsh conditions without degradation or failure.

Furthermore, Polymer matrix composites (PMC) are used in many applications where traditional composites would be too strong or expensive. For example, PMC's can be used for concrete replacement where they can absorb vibration and impact better than cement. They're also used for reinforced concrete and terrazzo applications where they can strengthen weak spots on structures. Additionally, PMC's are lighter than steel so they can reduce construction costs and weight restrictions for aircrafts and other vehicles. Further applications of PMC's include sports equipment, furniture and flooring materials. Figure 1 depicts the main types of manufacturing process for PMC.

Figure 1

Classification of manufacturing techniques used for polymer matrix composites



As show Figure 1, PMCs are one of the many materials that we have gained from 3D printing in recent years. In addition, 3D printing allows manufacturers to create many different composite parts virtually identical to each other.

As a result, composites are found in applications in various industrial sectors and, mainly, those produced by AM have found uses in the automotive (Bronz & Karaman, 2018), aerospace (Azarov et al., 2019; Brink et al., 2017; Lizut & Wojs, 2017), biomedical, sports sectors, and

industrial. Due to the multi-material nature, the composite's failure has complex mechanisms such as delamination, matrix cracking, fiber rupture, fiber buckling, and matrix crushing (Barbero, 2011).

AM, and more specifically, 3D printing, has begun a revolution by providing production capabilities for parts that were utterly utopic some years ago. AM is defined by ISO/ASTM 52900 as the '*process of joining materials to make parts from 3D model data, usually layer upon layer, as opposed to subtractive manufacturing and formative manufacturing methodologies*'. This 3D model data usually come from computer aided design software in .STL format (from stereolithography). As advantages, AM can produce high complexity, good dimensionality, and a wide range of materials, including recently composite materials. However, some drawbacks are low production volumes, small dimensions, and low manufacturing speed.

Fused Deposition Modeling is an additive manufacturing technique that creates 3D components using continuous wires of thermoplastic or composite material in the form of filaments. The extruder feeds the plastic filaments into the extruder die, where it is melted and then selectively deposited on the build platform layer by layer in a predetermined automated path.

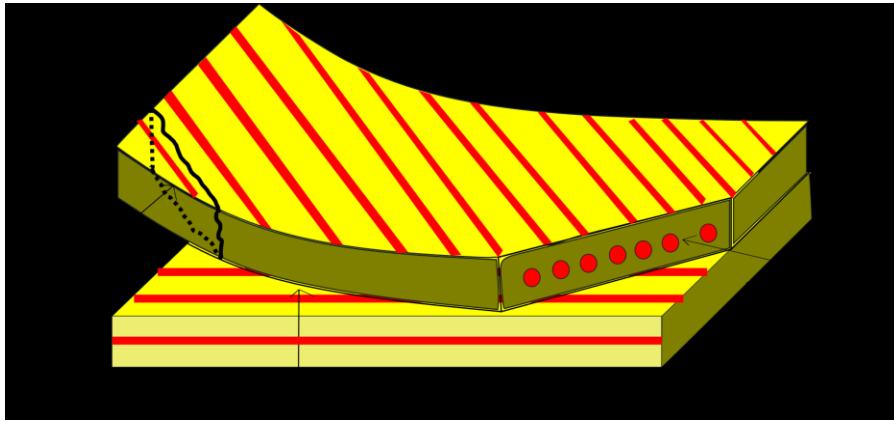
A recent technology, developed by Markforged, has raised polymer AM capabilities to a new level by printing polymer matrix composites with continuous fiber reinforcement. Being composites AM a relatively recent method, there is no consolidated model to predict the mechanical characteristics or failure modes when subjected to loads.

The failure of the composite plies can be divided into interlaminar, intralaminar, and translaminar fracture, as shown in Figure 2. Intralaminar refers to cracks in the matrix phase (Kousiatza et al., 2019). Interlaminar is the detachment of adjacent plies (Caminero, Chacón,

García-Moreno, et al., 2018), also known as delamination. Finally, translaminar implies a catastrophic failure of the lamina and cutting of the fibers (Swolfs & Pinho, 2016).

Figure 2

Principal types of failures in laminated composites



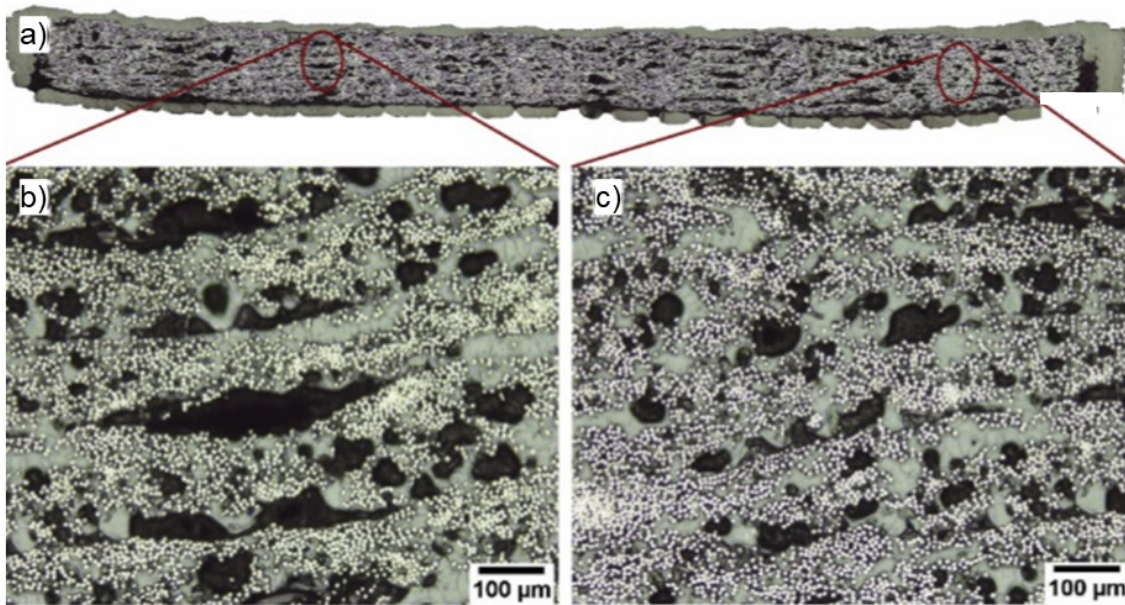
FRAM composites are classified into continuous fibers and short fibers (Blok et al., 2018). fused filament fabrication (FFF) polymers with composite materials have significantly improved the strength and stiffness of the old FFF polymer parts (Zhou & Chen, 2018). For example, chopped carbon fiber has shown improved mechanical properties with these methods, exceeding the aluminum resistance in some cases. Therefore, FRAM significantly improves the stiffness and strength of the raw polymer material, sometimes by a factor of three (Valvez et al., 2020), depending on the fiber type and its configuration.

However, the use of AM involves some unique complexities in strength determination and failure analysis. Due to the lack of a compression stage between layers (Mahajan & Cormier, 2015), voids and porosities exist between molten layers (Ciftci & Sas, 2019), see Figure 3, which decreases their mechanical performance. The failure of a material is an essential issue for engineers

and scientists because is mandatory to avoid it, or when it happens, to determine its causes, its evolution, and repair it to avoid future disasters.

Figure 3

Microstructure of an AM composite part (cCF/PA): a) overall thickness view, b) zoom in a low interlayer adhesion, c) zoom in a low inter bead adhesion



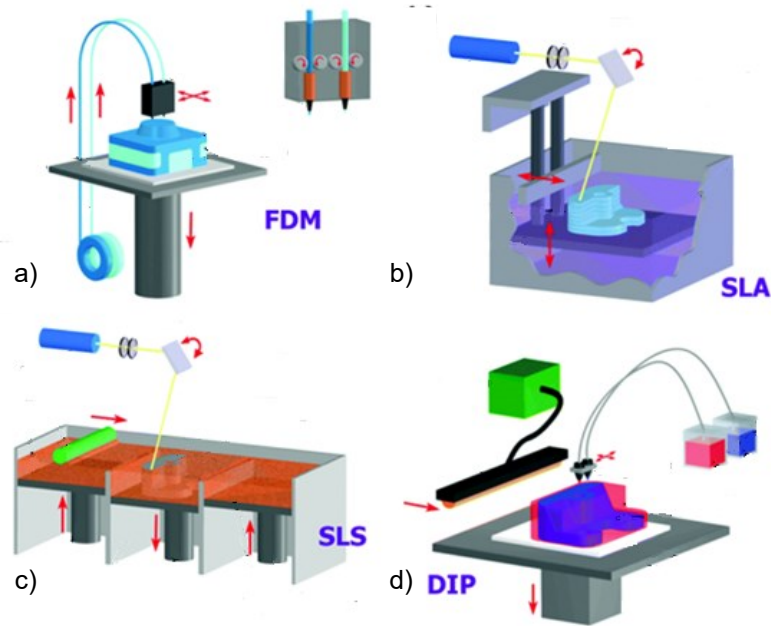
Source: (Chabaud et al., 2019)

2.1 Fused Filament Fabrication of Continuous Fibers

Different classifications of AM process are possible, one presented by (Ruiz-Morales et al., 2017) divides into dimensional order by point, line and plane. For example, inkjet is a point AM technology, while selective laser sintering (SLS) and extrusion free forming are line processes, moreover, in the plane category there are the stereolithography (SL) and laminated object manufacturing (LOM) methods. An schematic of diverse AM technologies is shown in Figure 4, in which the red arrows signals moving components.

Figure 4

Schematic of additive manufacturing methods: a) FDM, b) SLA, c) SLS, d) direct ink printing (DIP)



Source: (Ruiz-Morales et al., 2017)

Currently, the AM of fiber-reinforced composites is carried out by processes such as SL, LOM, FFF, SLS (Wei Zhu¹ et al., 2015), extrusion (Parandoush & Lin, 2017) and continuous fiber lattice fabrication (CLFL) (Eichenhofer et al., 2015). While the number of technologies is increasing, FFF is still the most common AM method for polymers and polymer composites (Brenken et al., 2018).

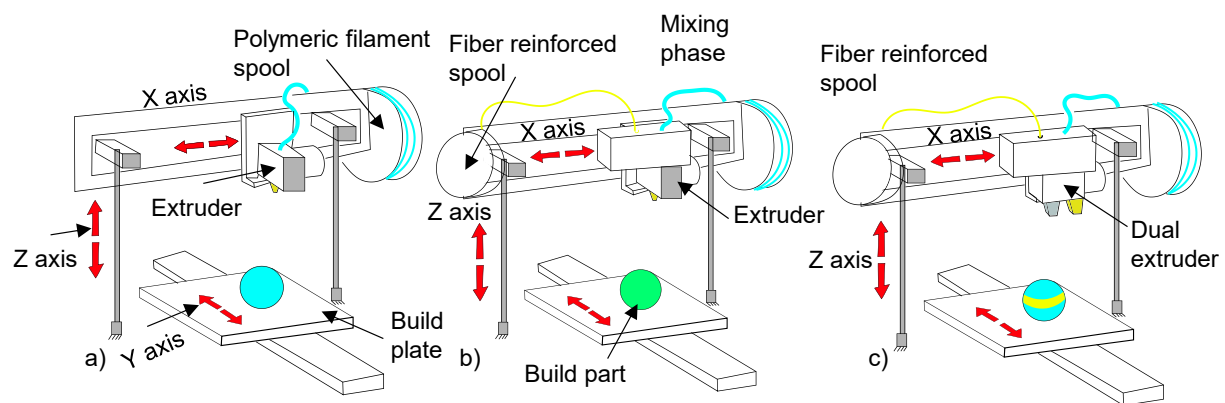
FFF is the AM process where the filament is fed into an extruder, heated above the melting point temperature, and deposited on a platform where the part is solidified and consolidated. A minimum 3-axis CNC software controls the extruder movement.

FFF technologies of fiber-reinforced polymers can be found with one (Figure 5a) or two extruders (Avdeev et al., 2019). The fiber contacts the die before extruding in the single extruder typology, as shown in Figure 5b. The use of a double extruder allows a reinforced filament and cutting system that allows a cut based on the calculation of the fiber length to be deposited (Justo, Távora, García-Guzmán, et al., 2018) in case the reinforcement is continuous, Figure 5c. The reinforcement can also be in the form of short fibers. Therefore, it is possible to use a single extruder, Figure 5a, and two extruders for its production.

Currently, AM materials range grows, expanding from polymers to metals and ceramics (Y. Hu & Cong, 2018; Parandoush & Lin, 2017). In the FFF Technology, the polymeric materials used for the matrix are thermoplastic, such as Nylon, ABS, PLA, and PEEK. These generally have lower mechanical characteristics than the thermosetting polymer matrices used in traditional manufacturing processes such as epoxy or polyester resin, but they can be recycled.

Figure 5

Schematic of FFF of thermoplastics and fiber-reinforced thermoplastics: a) single extruder, b) multi-material single extruder with mixing phase, c) double head extruder



Source: (León B. et al., 2020)

2.2 3D Printing of Continuous Fiber-Reinforced Additive Manufacturing Composites

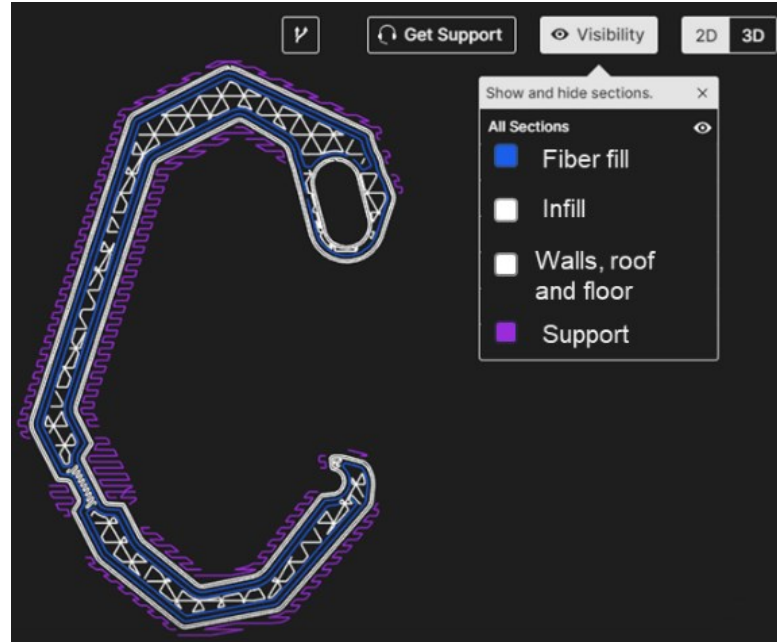
In a previous study (Warnung et al., 2019), the authors evaluate the mechanical and machinability properties of eight thermoplastic matrices. The reinforcement phase comes in short or long filaments: carbon for short filaments and long fibers of fiberglass, carbon, or Kevlar. Some authors have developed new filaments for 3D printing, highlighting the use of short carbon nanotube fibers (Calderón-Villajos et al., 2019; Isobe et al., 2018), providing parts with excellent mechanical characteristics, but at a high cost. Fiberglass and carbon in unique architectures, such as woven (Dickson et al., 2018) and prepreg (Q. Hu et al., 2018), have been developed. In addition, filaments are being produced using continuous organic reinforcing fibers, which are biodegradable and have a low cost (Matsuzaki et al., 2016; Montalvo Navarrete et al., 2018).

Each of these materials is better adapted to a given process, with certain compatibility restrictions; an example is that only photo-curable polymers can be used in stereolithography. However, many possible combinations that can be used are evident, configured by varying materials and processes. Figure 6 shows the internal part lay-up done in the Eiger software for AM of carbon fiber reinforced carabiner, displaying the high complexity and freedom in selecting materials, geometry, and process-related parameters.

Furthermore, some particular composites and fiber placement architectures have been developed for AM. For instance, in (Dickson & Dowling, 2019), they study the improvement in the load-bearing capacity of woven materials using AM, such as hemmed or bolted joints, showing the improvement in strength and the decrease of some failure modes such as delamination.

Figure 6.

A cross-sectional view of a FRAM carabiner in the software Eiger



Parts of hybrid composite material have been produced by AM (Swolfs & Pinho, 2019). They use two types of reinforcement: carbon and fiberglass, although the two fibers are not embedded simultaneously.

As in the design with traditionally produced composite materials, their mechanical behavior depends on the volumetric fraction of fibers, the angle arrangement, and the material properties of the reinforcement and matrix phases (Bandyopadhyay & Heer, 2018). In addition to the materials and the chosen process, another factor that alters the mechanical properties of composites produced by AM are the possible variations in the process parameters.

Due to the fusion and solidification of the thermoplastic polymeric matrix, the FFF process generates additional process parameters to consider (Fidan et al., 2019). It has been found that the

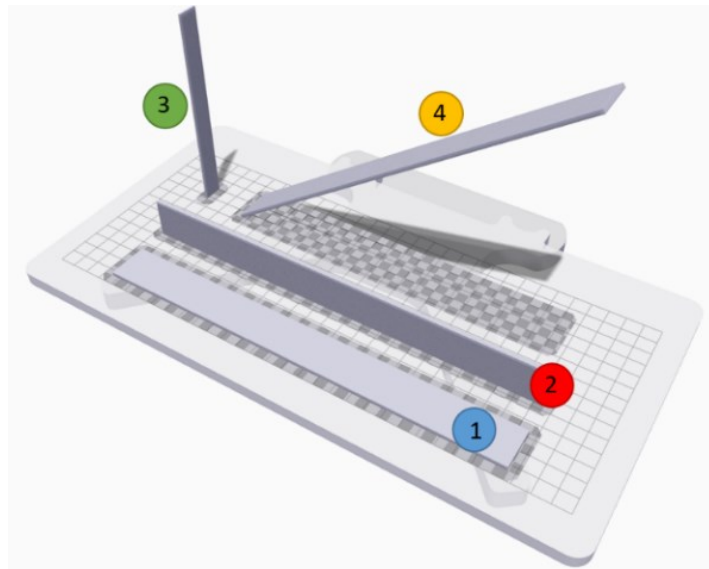
particular parameters of AM that affect the mechanical properties are: layer thickness, feed speed, construction direction, and extruder temperature (Quelho de Macedo et al., 2019), the first two being dependent.

The construction direction orientation is one of the parameters that most affect the part (Ravindrababu et al., 2018). Figure 7 shows different orientations for a proposed part; each will have distinct stiffness and strength values.

For instance, the optimal printing direction is the one causing the highest strength (Chacón et al., 2017). This case will be number 1 or 2: flat orientation with the extruder printing longitudinally or number 2 on edge.

Figure 7

Part orientations in the building bed: 1) flat, 2) on-edge, 3) upright, 4) inclined



On the other hand, the layer thickness affects the printing time, a lower thickness will require a longer printing time, but it will produce a better surface finish and greater geometric

tolerance. A lower layer thickness, in general, will produce a smaller porosity size (Rodríguez et al., 2003), which will decrease the tendency to damage progress. It can also increase interlaminar adhesion, producing more resistant parts with decreased layer thickness.

The printing temperature affects the melting and solidification process. Also, the viscosity of the polymer is a function of its temperature. A very high temperature will create more significant contractions when solidifying, generating large pores and gases from outside that could enter. A low temperature will make it challenging to consolidate the piece, but the thermal stresses will be lower. The optimal temperature will depend on the material, part size, and thermal conditions, usually within a range of values.

The fiber, both the type and the volumetric fraction, is one of the parameters that most affect the mechanical properties and failure mechanisms of an AM composite parts. The fiber orientation is the angle to the structural x-axis and is the primary source of the composites' anisotropy. A higher volumetric fraction of fibers will create stiffer and stronger pieces, higher in the fibers' direction but less ductile, and in general brittle failure can occur. Table 1 resumes the process parameters and their effects on the performance of the composite parts.

Table 1

Principal FFF process parameters, typical values, and effects in parts

Process parameters	Typical values	Affects
Layer thickness	In FFF from 0.1 mm to 0.3 mm or higher.	Interlayer bonding, geometrical tolerance, stepped geometry.
Feed rate	40 mm/s for PLA and polyamide.	The total printing time, higher feed rates can create defects such as retractions.

Process parameters	Typical values	Affects
Infill geometry	Depending on the slicer software, common architectures are grid or rectangular, triangular, hexagonal, and other honeycombs.	It can affect stiffness and strength as well as weight reduction.
Raster angle	Depends on the slicer software and the hatch strategy.	Thermal contractions, the bonding process.
Infill strategy	Usually, cross angle layers +45/-45.	Thermal contractions, the bonding process.
Temperature	Higher than the melting point of the filament material, for PLA 180 to 220 ABS 230 to 260 Nylon 255 to 270.	Lower melting temperatures may lack inter-bead and interlayer bonding, while higher temperatures imply higher void formation and residual stresses.
Fiber angle	Depending on the application, it can vary from 0° to 90°. Also, the angle can be a function of position, for instance, in concentric reinforcement.	In FRAM, the reinforce angle affects the mechanical properties such as stiffness, strength, and failure mechanisms greatly.
Volumetric fiber fraction	For Continuous fibers usually refer to the number of layers or passes of reinforced layers.	Stiffness and strength.

2.3 Material Modeling and Simulation of Fiber-Reinforced Additive Manufacturing Composites

FRAM composites can improve the material properties of polymeric AM by increasing the stiffness and strength (al Abadi et al., 2018). Nowadays, applications of the FRAM are manufacturing fixture tooling, mold equipment, biomedicine, and functional prototyping (Fidan et al., 2019). Also, depending on the layer configuration, it requires more specialized and costly equipment (Luo et al., 2019). As the application range grows, the need for correct characterization, modeling, and simulation becomes more important.

Various authors investigated the properties of polymers produced by FFF (Rodríguez et al., 2003) and have found porosities between the layers affect the mechanical properties due to the solidification process. These porosities are oriented in the extruder head's printing direction and are usually triangular (Parandoush & Lin, 2017), generating an anisotropy of the material, even when it is an isotropic polymer.

The manufacturing process creates anisotropy conditions similar to that found in fiber-reinforced composite materials (Chacón et al., 2017). Therefore, the constitutive equation is usually represented with an orthotropic model. Rodríguez et al., (2003), quantified this number of porosities based on microstructural studies with SEM micrographs. In addition, they generated models of mechanical behavior from homogenization methods, which can be numerical such as the FE method, or analytical as asymptotic homogenization.

The prevailing direction of porosities, affected by the printing direction, can lead to thinking that there is an optimal direction for printing a part. The optimal printing direction is investigated by Chacón et al., (2017, 2019), studying the influence of various parameters such as the printing direction, the layer thickness, and the filling pattern on the stiffness and strength of the models.

The AM parts of composite fibers do not usually present reinforcement throughout their cross-section but only in the areas where their use is most critical. Thus, in FRAM parts, various regions are found, such as (González-Estrada et al., 2018; Melenka et al., 2016b): i) solid matrix, 100% filled without considering the intrinsic porosities and defects of the material, ii) hollow filling patterns, which are cellular structures that support, but without resistance, lightening the part and allowing a shorter printing time and iii) regions reinforced by continuous fibers.

Melenka et al., (2016a) proposed using the average volume stiffness (VAS) method to calculate the elastic mechanical properties to determine the properties of the set formed by the three regions. In a recent study, (González-Estrada et al., 2018), the mechanical properties' results are compared with experimental values, and a micrographic analysis of the cross-section is performed. Other stress studies (der Klift et al., 2016) were performed for parts printed on MarkForged, showing that the rule of mixtures predicts longitudinal stiffness quite well for carbon fiber reinforced parts. Finally, Hart et al., (2018) reviewed the influence of some process parameters, such as printing direction and reinforcement, finding that printing direction significantly affects stiffness and strength when comparing reinforcement specimens oriented at 90 degrees. The specimen with the best performance was printed in a flat orientation and reinforced parallel to the load application.

Due to the multiplicity of manufacturing parameters, generating models capable of predicting elastic behavior for FRAM parts is a complex task. On the other hand, strength is a factor that cannot be weighted similarly. For this reason, failure criteria such as Hashin, Tsai-Hill, Hoffman, among others, have been used for composite materials (Barbero, 2013). However, the same criteria have not been developed or used with variations of the FRAM parts' process parameters. Despite the inherent difficulties of the strength prediction, in (T. A. Dutra et al., 2020), the authors developed an extended Puck-Schurmann, ExPan, applicable for AM composites.

Manufacturing process modeling can hint at structural failure and generate more efficient ways to produce AM parts. Yang et al., (2017), performed a modeling of the short fiber and long fiber extrusion process using a discrete element approach and smooth particle hydrodynamics (SPH).

Topological optimization has a strong link with AM in the design paradigm change since it allows the design and construction of highly efficient complex structures. The topological optimization processes that consider the anisotropy generated by the process have already been used (Garland & Fadel, 2018). Furthermore, according to the results by (Meneses et al., 2018), AM promises to bridge the gap between topological optimization and the final product by eliminating the constraint of geometric complexity imposed by traditional manufacturing processes. Thus, imposing more critical requirements in material selection rather than form selection to account for the desired damage onset and progressive failure behavior.

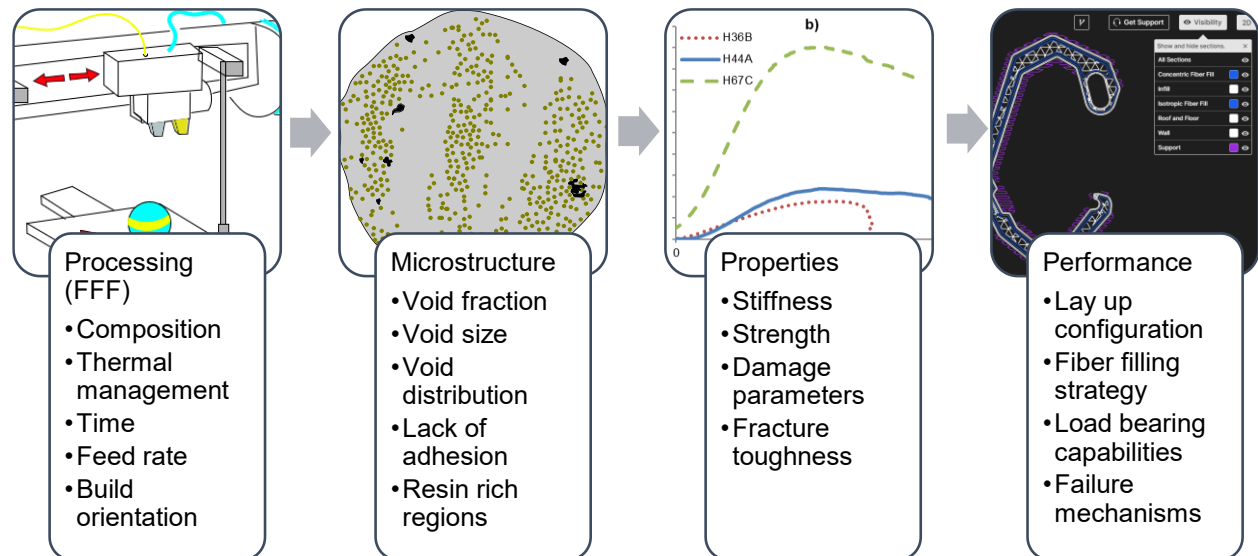
The strength of a part is linked to the failure of the first layer and the evolution of the damage when propagating through the different layers or sheets of composite material (Leon Becerra et al., 2017). Progressive damage analysis has been used in traditionally manufactured composite materials to predict this phenomenon. Furthermore, there is a scale dependency in AM composites, the performance of part is determined by the properties, which comes from a specific microstructure originated from a set of process parameters, see Figure 8.

In CDM, the damage is presented with a phenomenological variable, generally associated with changing some mechanical or geometric parameters such as stiffness or effective resistant area. It is sometimes convenient to measure internal damage in composite structures, using, for example, acoustic emission, phase array ultrasound (Caminero et al., 2019), and others to determine internal defects. Other works (Focke et al., 2018) try to close the gap between micromechanics and macrostructure using multiscale approaches. According to the above, the numerical modeling process is almost mandatory if required to know the stiffness or strength

before testing it. Several authors have proposed analysis schemes using the FE method (Papon et al., 2019; Ravindrababu & Makam, 2018) to determine the properties.

Figure 8

Scheme of the PSPP paradigm in FRAM parts



Ferreira et al., (2018) analyzed through FE, materials whose arrangement of continuous fibers are curved in the construction plane, achieving zones with variable stiffness. A design rule would be the placement of the reinforcement in the zones of maximum stress or along with the stress flow.

Al Abadi et al., (2018) compared results obtained analytically using the VAS method with numerical results using the FE method, using the damage model presented in (Lapczyk & Hurtado, 2007). Validation is performed with tensile tests on 3D composite parts. More advanced methods for predicting mechanical properties are summarized and evaluated by (Vignoli et al., 2019).

2.4 Mechanical Testing and Failure Mechanisms in Fiber-Reinforced Additive Manufacturing Composites

(Argüello-Bastos et al., 2018; Argüello-Bastos et al., 2018) also presented the compression characterization of these pieces by varying: the type of filling pattern, the orientation of the fibers, and their number of layers. Besides, they presented electron microscopy images showing compression damage mechanisms such as delamination by buckling, fiber fracture, and kink bands.

Hou et al., (2018) developed sandwich panel structures evaluated in compression, showing failure mechanisms such as local buckling, which is typical of structures of this type. However, the defects explained here are general and apply to the material rather than a specific structure.

As indicated by (Chabaud et al., 2019), the absorption of humidity by the matrix affects the properties, an effect known as hygroscopy. Regarding the volumetric fraction, Justo, Távora, & París, (2018) carried out a calcination process of the filaments to obtain the volumetric fraction of fibers, which is 40% by weight for glass fiber and 50% for carbon fiber, which represents about 30% in volumetric fraction. Different authors (Chabaud et al., 2019; Díaz et al., 2021; Mohammadizadeh et al., 2019) found similar results using image treatment in the reinforced filament micrographs. Likewise, (Justo, Távora, & París, 2018) performed compression and tension characterization processes for parts with carbon fiber and glass reinforcement; and in-plane shear for parts with fiberglass reinforcement.

Several studies of the delamination phenomenon (Caminero, Chacón, García-Moreno, et al., 2018; García Móstoles et al., 2018) have found that there is a significant effect of the thickness of the layer in the interlaminar strength. The interlaminar shear strength (ILSS) decreases with increasing thickness. Furthermore, the type and content of reinforcement were evaluated, showing

marked differences according to the nature of the fibers. In (Bitar et al., 2017), the authors performed tensile tests in the z-direction, normal to the laminate plane, as a direct method to evaluate the interlaminar tear strength (ILTS). One of the crucial factors in delamination processes is fracture toughness in Mode I. (Goh & Yeong, 2018) performed DCB (double cantilever beam) tests, finding that toughness improves with increasing extruder and platform temperature and decreasing printing speed. The decrease in interlaminar strength properties was discussed based on fractographic analysis.

On the other hand, experimental tests have determined that fracture toughness improves with localized reinforcement of carbon fibers, implying that it is possible to generate structures with target properties in different structure areas (Akasheh & Aglan, 2019). In (T. A. Dutra et al., 2019) authors evaluated the mechanical properties of the reinforced section using an asymptotic homogenization technique. They also showed that the properties of the reinforcing Nylon matrix are different from those of the 100% Nylon filament. In another study, the same authors determined the effect of some process parameters on interlaminar resistance to shear, a key parameter at the time of delamination (T. Dutra et al., 2018). Finally, (Swolfs & Pinho, 2016, 2019) propose an optimization method using finite elements to generate a microstructure that improves translaminar fracture toughness.

Several researchers (Caminero, Chacón, García-moreno, et al., 2018) studied the influence of 4 parameters such as the print architecture (construction direction), type of fiber: carbon, Kevlar, or glass, the fiber content as a volumetric fraction, and the thickness of the layer in the impact resistance of FRAM parts.

The combination of reinforcement of short fibers with long fibers can generate even more resistant pieces. In (Naranjo-Lozada et al., 2019), the influence of the volumetric fraction of fibers,

the printing architecture, the filling patterns, and their density was assessed in the tensile properties of the 3D printed parts using an experimental ANOVA design. Araya et al. studied the effect of the properties of the same four properties: reinforcement pattern, reinforcement distribution, the orientation of the print, and the volumetric fraction of the fibers (Araya-calvo et al., 2018) in compression and bending using a 3-point bending test. (Ziemian et al., 2016) characterized degradation caused by fatigue using a continuous damage mechanics (CDM) model.

(Mei et al., 2019) carried out a similar study of the variation of parameters but used three different reinforcing fibers: carbon, glass, and aramid. (Argawal et al., 2017) study the same four parameters plus the category of reinforcement: isotropic concentric, performing a Taguchi experiment design for statistical analysis. Kvalsvig et al. (Kvalsvig et al., 2017) also used Taguchi to evaluate the main parameters that affect the tensile properties. Regarding the physical characterization of defects, Ning et al. (Ning et al., 2017) studied the porosities in FRAM parts and their morphology when changing the content of fiber. These are divided according to their cause: pores generated from the filament manufacture process, pores due to the physical separation between the deposition layers, and pores due to fiber removal or defects in the fiber-matrix interface. On the other hand, it is interesting that interrupting the AM operation may affect the strength of the part. Sinha and Meisel (Sinha & Meisel, 2018) studied this phenomenon, where the change in strength is associated with cooling and the role of induced thermal stresses.

The most used experimental methods in the analyzed articles are SEM, optical micrography, digital image correlation, acoustic emission, ultrasound emission, and destructive tests. Oztan et al. (Oztan et al., 2019) were interested in the relationship between mechanical properties and the microstructure of the material, employing SEM images and finding links between both. On the other hand, Goh et al. (Goh et al., 2018) focused on the microstructure of

the failure, analyzing the damage mechanisms when the failure occurs due to tensile and bending. Dynamic properties such as creep have been studied by Mohammadizadeh et al. (Mohammadizadeh et al., 2018) using DMA; also, a microstructure analysis is presented. To monitor temperature and deformation changes both in manufacturing and in-service, (Kousiatza et al., 2019) has used Bragg sensors to effectively measure the coefficient of thermal expansion, demonstrating its high dependence on fiber orientation.

Pyl et al. (Pyl et al., 2019) carried out open-hole tests on parts of the composite material produced by AM, where the architecture of the reinforcement is investigated, which can be concentric around the hole or isotropic reinforcement and then trimmed. It is observed that the value of the ultimate resistance and the damage mechanism depend to a great extent on the chosen configuration. In (Türk et al., 2017), the authors present a different synthesis between AM and composite materials design since AM can enhance traditional composite manufacturing methods.

Being such a recent technology, the panorama of the possible applications is still limited. Work is underway to overcome the disadvantages of the method, such as low manufacturing volume and high printing time, although printing costs are virtually the same for one as for thousands of parts (Parrado-Agudelo & Narváez-Tovar, 2019). Efforts should also be made to understand the failure mechanisms better and develop models to predict them, which are complete and include the characterization of filling structures and the anisotropy of the part.

4D printing also reaches composite materials, particularly in manufacturing structures with shape memory. In this type of manufacturing, polymeric structures are produced that unfold by means such as electrical currents (Garces & Ayranci, 2018). These materials and processes will surely drive the need to build even more complex damage prediction models. The trend will be

towards increasing part dimensions, as in large area AM (BAAM) (van de Werken et al., 2020) already decreased printing time, as in HARP technologies (high speed and area rapid prototyping)

The complexities of the process, the difficulty of quantifying the properties, and evaluating the damage perhaps are on par with the possibilities of innovation and new applications that the design of composite materials with AM offers. When the process is better understood, better parts will be designed, and innovative part design will expand application boundaries and demand new, more reliable analysis methods.

3. Methodology

The thesis results impact the understanding of AM composite parts, thus allowing engineers to perform better designs. The general workflow starts with this objective in mind, from the AM composite part design is divided into regions, next an integration into FE analysis is done, and finally, the mechanical behavior is analyzed and validated.

When dividing the material regions, 3 major stages can be distinguished: identity, characterize and analyze or verify. Therefore, the identification process includes finding the principal characteristics and the correct material behavior model. The characterization involves performing the testing and applying numerical methods when needed in order to find the material properties, and finally, the analysis and verification stage checks the material properties and verifies errors. Figure 9 depicts the three major stages for each material region being considered.

Figure 9

Material regions with the identification, characterization, and analysis stages

Lattice structures	Solid polymer	Composite region
<ul style="list-style-type: none"> • Define the relative density and infill type • Characterize by FE method, tensile, compressive test, and analytical (Gibson & Ashby 1999) • Analyze stress strain curve, retrieve the mechanical properties 	<ul style="list-style-type: none"> • Define the type and bulk properties, select the constitutive equation • Characterize by homogenization methods, DMA, and tensile tests • Analyze time-temperature response 	<ul style="list-style-type: none"> • Define stack up order, the fibers, and their angle • Characterize by i) experimental test data and collected data ii) micromechanics • Analyze by DOE approach, microstructural by fractography, and validate through DIC of open-hole

3.1 Materials and Fabrication Method

Samples were 3D printed from the Markforged MarkTwo, shown in Figure 10. Also, in the infill characterization, a Prusa i3 Version Geetech A10 was used; the latter used PLA as the printed material. All the samples were prismatic in form, while the dimensions could vary concerning the applicable standard.

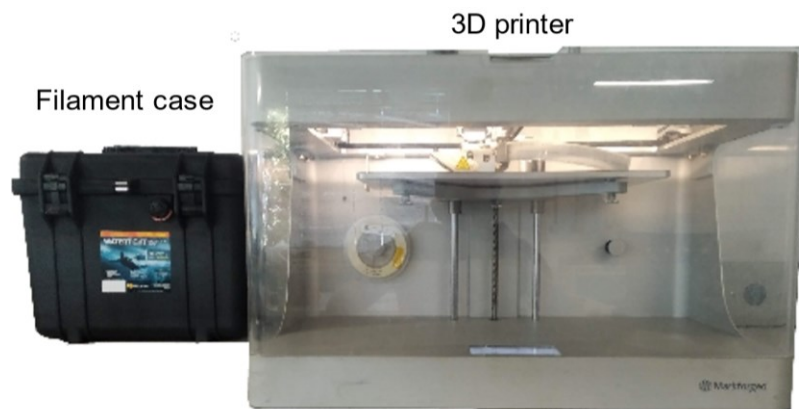
The 3D printer manufacturing company supplied the materials employed, Appendix C. Markforged materials datasheet, depicts the mechanical properties informed by the manufacturer. As seen in Figure 5, the 3D printer disposes of two head extruders: one for a thermoplastic matrix and another one for composite filament. The available thermoplastic matrices are Onyx ® and Nylon White, the manufacturer does not give much information on the composition, but according to the work of (Pascual-González et al., 2020), it could be determined that Onyx is a chopped carbon-fiber in a polyamide resin. At the same time, nylon white is a polyamide, most likely a PA-

12. The reinforcement filament materials are Kevlar, carbon-fiber, and fiberglass in standard and high-strength variants.

It is to note that the behavior of the material is independent of the polymer being allocated for the rest of the part, permitting, for instance, to characterize the composite phase and extrapolate the results to another AM part with different polymer nature. Thus, assuming that the influence of the different polymeric matrices in the interface between reinforcement and polymer is negligible.

Figure 10

Markforged 3D printer with filament case



3.2 Characterization Techniques and Equipment

The 3D printed samples were analyzed using tensile and compressive testing, scanning electron microscopy (SEM), and DMA. Following is presented a brief description of each characterization technique used.

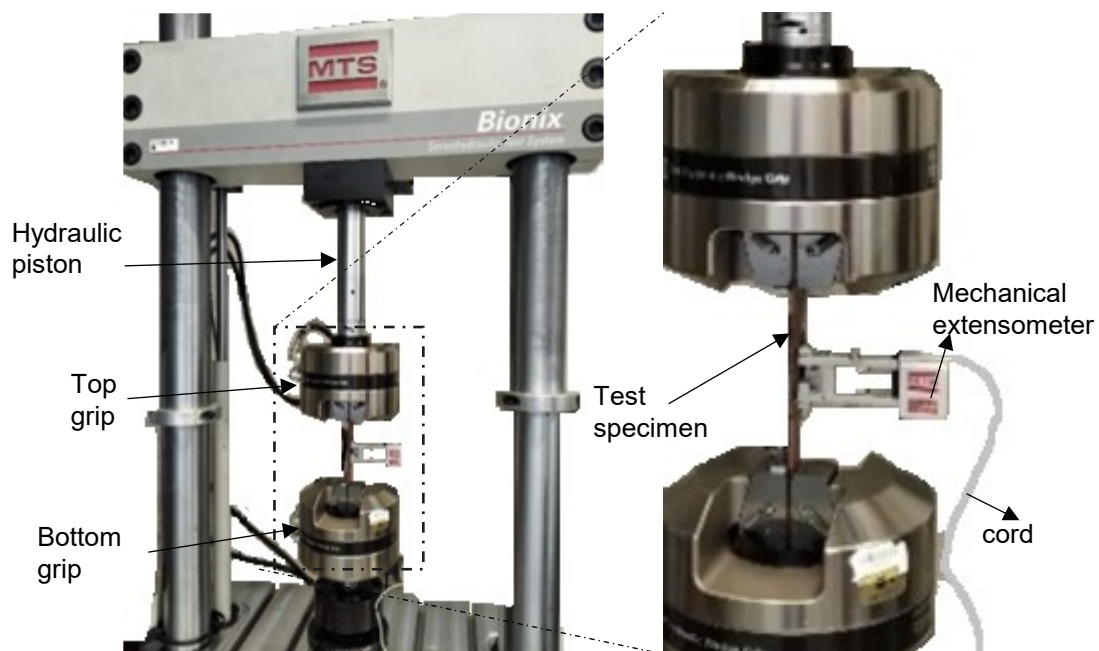
3.2.1 Tensile, Compressive, Shear, and Flexural Testing

Mechanical properties such as stiffness, strength, and ductility were obtained through tensile testing according to ASTM D3039 (ASTM, 2014). A few compressions test was carried

out using the compression fixture, and the accessory created following the ASTM D3410 (ASTM, 2016). standard the compression results are also taken from (Araya-calvo et al., 2018). Testing was performed in a MTS Bionix 370.02 with a load cell of 25 KN, see Figure 11. Shear test would be beneficial to characterize the material, however, is not fully needed as angle plies can supply the required information.

Figure 11

Tensile test on the MTS Bionix 370.02 machine

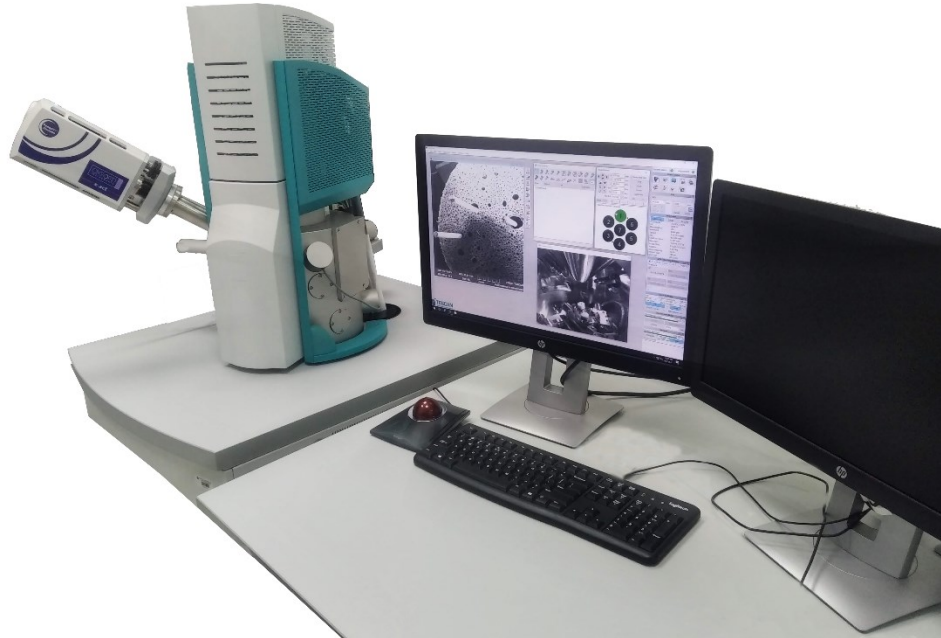


3.2.2 Scanning Electron Microscopy

Microstructural and fractographical analysis of the 3D printed samples was performed in a Quanta FEM 650 SEM and a Vega Tecscan (shown in Figure 12) located in PT Guatiguará and Tecnoparque Nodo Bucaramanga, respectively.

Figure 12

Vesga Tecscan SEM in Tecnoparque Nodo Bucaramanga

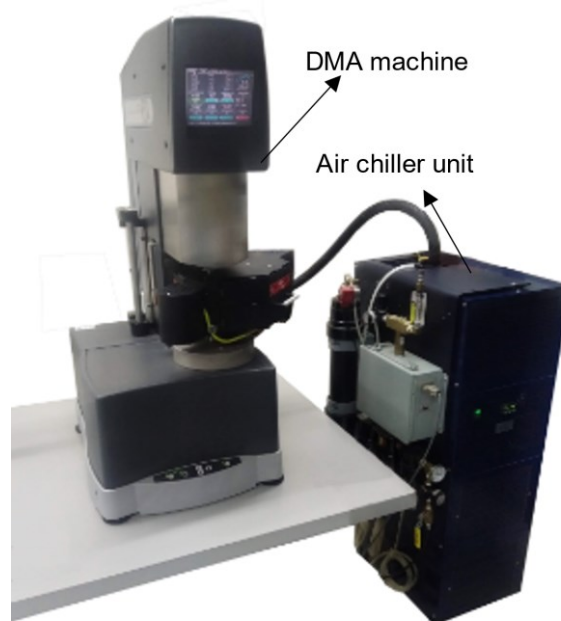


3.2.3 Dynamic Mechanical Analysis

DMA was carried out for a thermomechanical analysis. The RSA-G2, see Figure 13, is one of the most advanced platforms for mechanical analysis of solids with independent control of deformation and measurement of stress. The RSA-G2 has a temperature range of -150 °C to 600 °C. DMA was performed in a three-point bending fixture with a constant ramp temperature control, see Figure 14.

Figure 13

DMA module TA RSG-2 and air chiller unit

**Figure 14**

DMA test chamber view of an Onyx sample



3.3 Experimental Setup

The experimental campaign was performed in stages each one for each block of the Figure 9. First, characterization of infill and solid polymer structures were carried out, and then the reinforcement region.

The experimental campaign to determine the mechanical properties of FRAM was carried out considering the orthotropic model presented in composite materials. Also, strength limits are orthotropic. Therefore, an extensive set of empirical data is needed to characterize a composite fully. Table 2 shows the test type and the determined properties of the composites FRAM carried out in this thesis. The experiments were carried out on the Bionix MTS 370.02 testing machine, following ASTM D3039 (ASTM, 2014) and ASTM D3410 (ASTM, 2016). Also, where some property value was challenging to obtain, bibliographic research was carried on, validating and complementing our experimental test.

Table 2

Experimental test needed to characterize a composite

Test type	Fiber orientation	Number of samples	Determine properties
Tension	0°	5	E_1, F_{1T}, ν_{12}
Tension	90°	5	E_2, F_{2T}
Tension	45°	5	G_{12}, F_6
Compression	0°	5	E_1, F_{1C}

3.4 Analysis, Validation and Verification

Once the data is obtained it was analyzed using diverse methodological tools, the experimental data was analyzed through a design of experiment framework, using analysis of variance and the model was numerically verified using FE method with Ansys as software. Finally, the data was validated using digital image correlation, an optical full-field displacement technique.

4. Material Modeling

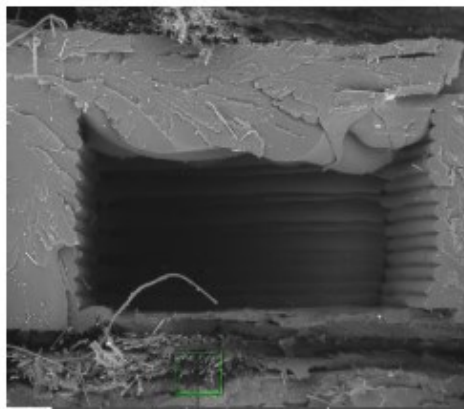
As presented in the previous chapters, FRAM can have multiple material regions, see Figure 15. The mechanical behavior or performance of the component will be one in which the material properties are affected by the boundary conditions. The loads create a specific strain and stress state, and the stress or strain state and the strength of the material will determine the security factor of the component. The material behavior can be described in the constitutive equation, which relates the stress tensor with the strain tensor. The constitutive equation classifies the materials into different kind of behavior: elastic, plastic, viscoelastic, or hyper-elastic. Furthermore, each behavior is not described in a unique model. Instead, multiple models exist that can describe a material behavior.

This chapter concerns the material modeling of FRAM. It will address the objectives of developing a material modeling strategy for characterizing a composite laminate's stiffness and strength from FFF, considering the layup configuration, the fiber orientation, and the geometrical dimensions of each region.

Recalling the microstructure of a FRAM part, see Figure 15. Depending on the design, three main regions are distinguishable: a solid thermoplastic polymer region, a cellular region, which is recognized by a low density value, and a fiber-reinforced region.

Figure 15

Cross-section view of FRAM



Source: (González-Estrada et al., 2018)

Some FFF variations can produce multi-material extrusion using double extrusion or co-extrusion methods (León B. et al., 2020). Figure 10 shows the Markforged MarkTwo (Mark & Gozdz, 2015) FFF-based composite 3D printer used for this research, a double extrusion type. A nylon matrix makes composite parts with three fiber reinforcements: carbon fiber, fiberglass, or Kevlar.

4.1 Geometrical and Mechanical Characterization of the Composed Regions

Typically, a FRAM part is formed by adding layers of a thermoplastic polymer in both the bottom and the top (called floor and ceiling) layers, and those layers help support the piece while allowing the correct remotion of the part and protecting the interior from environmental conditions.

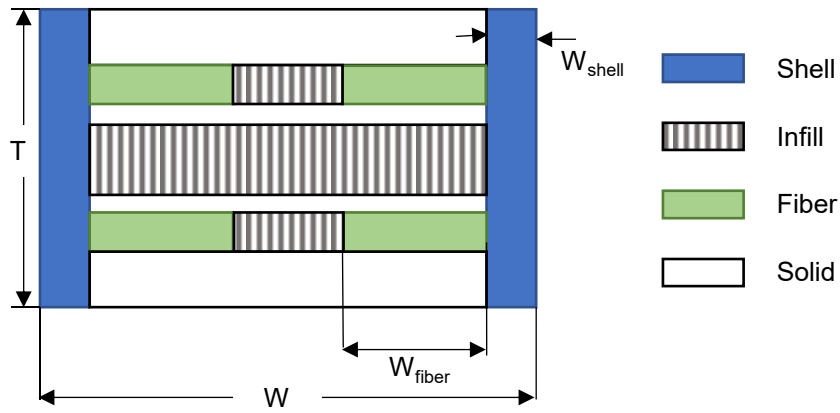
The middle layers can be a solid thermoplastic, or an infill pattern made by a lattice structure, triangular, honeycomb, gyroid or rectangular lattice with varying densities. Besides support structures, lattices can be used to reduce the weight of the part by making it less dense. This feature can be useful, for instance, in the hip-joint replacement (Ho et al., 2015) and in some parts, represent a high volume portion. Models for finding the stiffness of the infill patterns are those presented in (Gibson & Ashby, 1999).

Also, fiber-reinforced can be placed in the center layers, in the whole width, or just a section. Despite the great design freedom, this technology is 2.5D, which means fiber can be placed only in the printing plane. Figure 16 shows the most generic transverse section. The fiber-reinforced regions are continuous fibers composites that either follows the contour of the part in a disposition called “concentric” or are aligned in a specific angle and are named "isotropic". These fiber-reinforced regions are subjected to the specific capabilities of the process; for instance, the fiber length must be at least 30 mm of length and have a contour of at least 0.25 mm.

Experimental work (Justo, Távora, García-Guzmán, et al., 2018) performed the characterization of 3D printed composite parts in tension, compression, and in-plane shear test, and the results show that, as expected, the mechanical properties depend on the arrangement and the volumetric content of the individual regions. Melenka et al.(Melenka et al., 2016a) propose a Volume Average Stiffness (VAS) method for a composite with Kevlar reinforcement. However, a simplified model (Rodríguez et al., 2003) characterizes infill patterns, assuming them as a regular solid infill with a high porosity level. Leon-Becerra et al. (J. León-Becerra et al., 2021; J. S. León-Becerra et al., 2020) proposes the use of specific infills equations in the VAS method and proposes correlations for the accurate characterization of stiffness in AM.

Figure 16

Cross-section schematic view of a typical FRAM component



4.2 Infill Regions

The relative infill density refers to the ratio of the volume occupied by the printed material. Table 3 shows the minimum, maximum, and default values of the three most available infill patterns in the Markforged 3D printer: rectangular, triangular, and hexagonal or honeycomb (Argüello-Bastos et al., 2018).

Table 3

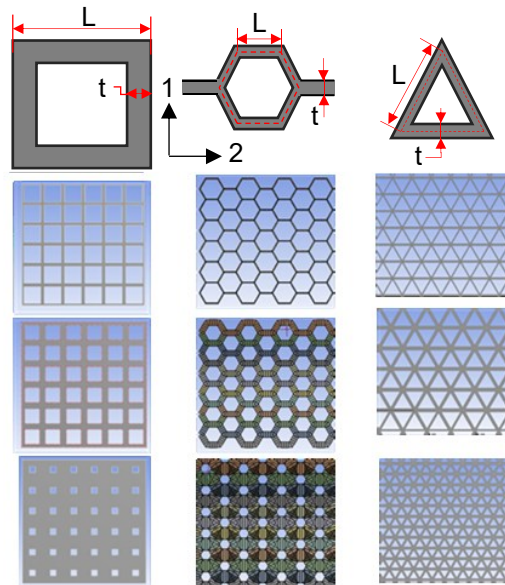
Infill density range for different patterns

Pattern	Minimum	Maximum	Default Value
Triangular	28%	55%	44%
Rectangular	>0%	92%	50%
Hexagonal	18%	62%	37%

Figure 17 shows the representative unit cell (RUC) with three infill densities for the most common patterns. RUC is the minor structure that repeats itself along the lattice region. In the next section, the equations used for the mechanical characterization of the different regions are presented.

Figure 17

Different RUC of infill patterns with three infill densities following values in Table 1



4.2.1 Honeycomb or Hexagonal

Honeycomb patterns are used mainly for compression applications, such as a sandwich core in composite panels manufacturing. It has excellent strength with fast printing times. Moreover, the geometrical characterization can be found in (Gibson & Ashby, 1999). Equation (1) to equation (3) characterize a regular hexagonal lattice:

$$\frac{\rho^*}{\rho_s} = \frac{2}{\sqrt{3}} \frac{t}{l} \left(1 - \frac{1}{2\sqrt{3}} \frac{t}{l} \right) \quad (1)$$

$$E_1 = 2.3E_s(t/l)^3 \quad (2)$$

$$G_{12} = 0.57E_s \left(\frac{t}{l} \right)^3 \quad (3)$$

Where t and l refer to the thickness and length, respectively, E_s represents the elastic modulus of the solid, E_1 the elastic modulus in the preferent fiber direction, and G_{12} the in-plane shear modulus. Furthermore, the function density is found through equation (1). In which ρ^* is the lattices density and ρ_s the solid material density.

4.2.2 Rectangular or Grid

Rectangular is the standard infill pattern of most FFF 3D printers. It represents the right balance between strength in all directions and printing time. The representative unit cell (RUC) of the square pattern is a square with side l .

If a constant thickness is assumed, the infill density expresses the ratio of the filled area to the total area. For the square pattern, it is given by equation (4) (Gibson & Ashby, 1999):

$$\frac{\rho^*}{\rho_s} = \frac{2lt - t^2}{l^2} \quad (4)$$

Where t and l stand for the thickness of the strut and, side length of the square respectively (Gibson & Ashby, 1999), equation (5) and equation (6) for the elastic moduli are:

$$E_1 = E_s(t/l) \quad (5)$$

$$E_2 = E_1 \quad (6)$$

4.2.3 Triangular

The triangular infill pattern has high strength along the direction of the wall, so it is more robust than a rectangular pattern but takes more time to print. The triangle pattern is stiffer than the rectangular (Gibson & Ashby, 1999), as can be inferred from equation (7) and equation (8).

$$E_1 = 1.15E_s(t/l) \quad (7)$$

$$E_2 = E_1 \quad (8)$$

The expression for the density is given in (Gibson & Ashby, 1999) shown in equation (9).

$$\frac{\rho^*}{\rho_s} = 2\sqrt{3}\frac{t}{l}\left(1 - \frac{\sqrt{3}t}{2l}\right) \quad (9)$$

4.3 Solid and Shell Regions

For those regions, the model employed was that proposed by Rodriguez (Rodríguez et al., 2003), here reproduced in equation (10) to equation (16):

$$E_1 = (1 - p_1)E_s \quad (10)$$

$$E_2 = (1 - \sqrt{p_1})E_s \quad (11)$$

$$E_3 = E_2 \quad (12)$$

$$G_{12} = G_s \frac{(1 - p_1)(1 - \sqrt{p_1})}{(1 - p_1) + (1 - \sqrt{p_1})} \quad (13)$$

$$G_{23} = (1 - \sqrt{p_1})G_s \quad (14)$$

$$v_{12} = v_{13} = (1 - p_1)v \quad (15)$$

$$v_{23} = (1 - \sqrt{p_1})v \quad (16)$$

Where p_1 in equation (10) to equation (16) stands for the porosity value, although this research was performed on ABS, it could be extended to other materials with similar geometrical characteristics because of the asymptotic homogenization method.

4.4 Fiber-Reinforced Region

The mechanical characterization of the fiber-reinforced region is obtained from analytical and semi-analytical expressions (Barbero, 2013) of the micromechanical model, particularly for obtaining E_1 and ν_{12} Reuss model (rule of mixtures) is employed, Voigt model (inverse rule of mixtures) for characterizing transverse modulus E_2 , cylindrical assemblage for G_{12} , semi-empirical stress partitioning parameter for G_{23} .

In a FRAM part, the reinforced phase are the layers with composite reinforcement, and those layers are the stiffest and strongest of the 3D printed part. Thus, the accurate characterization and design significantly affect the overall structural performance.

Initially, research works focused on the characterization of FRAM, mainly their static mechanical properties, usually determining the stiffness, strength, and failure behavior subjected to load types such as impact, flexural, tension, compression, and interlayer strength (Dickson et al., 2017; González-Estrada et al., 2018; Pertuz et al., 2020). As with traditional manufacturing composites, the load type affects the failure mechanisms (Caminero, Chacón, García-moreno, et al., 2018). For example, fiber rupture is a typical feature in tensional loads in the longitudinal direction, while tension in the out-of-plane direction usually causes interlayer debonding. Leon B

et al. (León B. et al., 2020) present a state-of-the-art review of continuous fiber-reinforced AM's damage and failure mechanisms. (Díaz-Rodríguez et al., 2021) present a critical review of the mechanical properties of FRAM, showing the high range of mechanical properties and process parameters are analyzed, revealing that scattering of the mechanical properties is inherent to environmental conditions, manufacturing process parameters, and constituent material properties. (Justo, Távara, García-Guzmán, et al., 2018) have shown that stiffness and strength depend on print direction, type of fiber, layer thickness, and volumetric fiber fraction. They can be adjusted to optimize a given mechanical property, as (Ahmed et al., 2020) did by optimizing the interfacial bond strength.

All the possible manufacturing parameters variations would imply a vast number of experiments to fully characterize FRAM, and researchers are interested in creating models that accurately predict the mechanical properties and failure behavior. Some models are physically based, depending on the microstructure, others could be entirely based on experimental data. One of the critical microstructural descriptors is the volumetric fiber fraction of as-received filament, obtained through thermogravimetric analysis (TGA), which can give the volumetric fiber fraction and thermal behavior of the composite, calcination uses the same principle of separating phases using temperature. Other methods involve using chemical acids by dissolving the thermoplastic (Chabaud et al., 2019). The matrix's chemical nature can be characterized using differential scanning calorimetry (DSC). The methods for characterizing the single fiber are first separate from the matrix using chemical solvents, for instance, and then subjected to a tensile test. (Chabaud et al., 2019) show the effect of environmental conditions, particularly the humidity content, on the stiffness and strength of the FRAM parts by performing thermogravimetric and image processing analysis shows that the carbon fiber filament has a volumetric fraction of 35% and the glass fiber

filament of 39%. Also, the humidity can create variations of 18% in stiffness or 25% in strength for the longitudinal direction. Via imaging analysis confronts the porosity values of FRAM, which can reach values of 15.1% for continuous carbon fiber polyamide (cCF/PA) parts and 12.3% for cGF/PA parts, which are considerably more than in traditional composite manufacturing methods such as filament winding which are in the order of 5% (Mehdikhani et al., 2019). Also, in (Pascual-González et al., 2020), the authors present an extensive experimental micromechanics characterization of AM for the single fiber properties, the fiber distribution and content, and the polymer nature. (T. A. Dutra et al., 2020) develop an expanded Puck and Schürmann (ExPan) interfiber fracture criterion, which considers the semi-brittle nature of the thermoplastic matrix. Moreover, the authors presented the failure envelopes of 3D-printed composites.

In the next sections, the mechanical characterization of the fiber-reinforced phase is made, first for the stiffness and later for strength, after, some insights on the role of the manufacturing process in the reinforce phase properties are provided.

4.5 Stiffness Characterization: Numerical, Micromechanical, and Experimental

From a micromechanical point of view, it is possible to determine the overall composite behavior from their constituents, the arrangement in which they are located, and the interface properties which unite them. Micromechanics is an extensive field of study, and a comprehensive study of their methods and techniques is out of the scope of this thesis, and the reader could refer to the review of (Raju et al., 2018). Micromechanical methods can be classified into analytical and numerical. In this section, simple analytical models such as the rule of mixture (Voigts model), inverse rule of mixture (Reuss model), cylindrical assemblage (CAM), among others, are used to provide fast and valuable data. Also, RVE size was found through a numerical homogenization

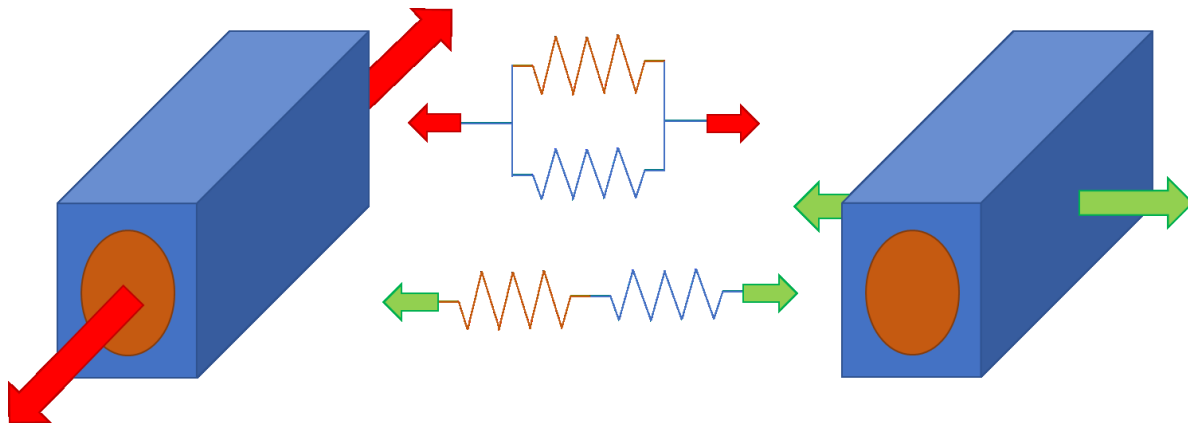
based on the FE method and combining a two-step homogenization process which considers the porosities and physical distribution of the filament.

4.5.1 Analytical Formulation

Analytical expressions are derived from simplified assumptions of the mechanical behavior of the composite. For example, the rule of mixtures is derived assuming the whole composite behaves as a consolidated material in which both fiber and matrix phase experience the same amount of strain (ε), while the inverse rule of mixtures is derived from the simplification of fiber and matrix phase are in the same stress state (σ), and this fact can be viewed in Figure 18. For the derivations shown from equation (17) to equation (21), it is noted that in the parallel arrangement of springs, the displacement is equal, and the force balance (20) is the sum of the individual forces of the matrix and fiber.

Figure 18

Serial and parallel arrangement of a unit cell of a composite schematic



$$F = F_m + F_f \quad (17)$$

$$\varepsilon = \varepsilon_m = \varepsilon_f \quad (18)$$

$$\sigma = E_{eq}\varepsilon \quad (19)$$

$$AE_{eq}\varepsilon = A_mE_mE_m\varepsilon_m + A_fE_f\varepsilon_f \quad (20)$$

$$E_{eq} = V_mE_m + V_fE_f \quad (21)$$

Rule of mixtures (ROM) and IROM (IROM) are useful because they represent the upper and lower bounds of any given mechanical property, provided that the materials are in their linear behavior region. For example, experimentally ROM model agrees with the longitudinal modulus E_1 , while iROM helps determine the value of transverse modulus E_2 . Other properties such as in-plane Poisson ratio ν_{12} are also well approximated by the ROM model.

Numerous analytical models have been proposed since the ROM and iROM first appeared, and they follow the need to give better estimates of the mechanical properties of composite materials. Such models can be based on an analytical homogenization scheme such as Mori-Tanaka, asymptotic homogenization, or simplified models such as the Cylindrical assemblage model (CAM), periodic microstructure model (PMM), Halpin Tsai. The present work uses the referred models in the following Table 4 to calculate the elastic properties.

Table 4*Micromechanical models and the associated property*

Model	Property
Rule of mixture	E_1, ν_{12}
Inverse rule of mixture	E_2, E_3, G_{12}
CAM	G_{12}, G_{23}
Halpin-Tsai	E_2
SSPP	G_{23}
PMM	All
Informed decision	ν_{13}, ν_{23}

4.5.1.1 Rule of Mixtures and Inverse Rule of Mixtures. ROM, also known as the Voigt model, assumes the strain equivalence in the fiber direction while considering the volumetric ratio of the phases. The IROM or Reuss Model is based on stress equivalence in the transverse direction. The mass balance, ROM, and IROM are depicted in equation (22) to equation (24), respectively:

$$1 = V_m + V_f \quad (22)$$

$$P = V_f P_f + V_m P_m \quad (23)$$

$$\frac{1}{P} = \frac{V_m}{P_m} + \frac{V_f}{P_f} \quad (24)$$

V_f is the volumetric fiber fraction, and V_m is the volumetric matrix fraction. The subscripts f represents the fiber fraction property value, m the matrix fraction property value, and P the composite property calculated.

In traditional manufacturing composites, ROM is used in the prediction of E_1 and ν_{12} , while IROM is used to determine the E_2 , E_3 Young's modulus as well as the In-plane Shear Modulus G_{12} .

4.5.1.2 Cylindrical Assamblage model. The CAM model proposed by Hashin and Rosen gives better estimates for the in-plane Shear Modulus (Barbero, 2011). It is depicted in equation (25)

$$G_{12} = G_m \left[\frac{(1 + V_f) + (1 - V_f)G_m/G_f}{(1 - V_f) + (1 + V_f)G_m/G_f} \right] \quad (25)$$

4.5.1.3 Semi-empirical stress partitioning parameter. This model is not a genuinely analytical method due to the dependence on an empirically adjusted parameter known as stress partitioning, which divides the stress portion into one for the fiber and another for the matrix. Its formulae are presented in equation (26) and equation (27). It is employed in the prediction of the transverse shear modulus G_{23} (Barbero, 2011).

$$G_{23} = G_m \left[\frac{v_f + \eta_4(1 - v_f)}{\eta_4(1 - v_f) + v_f G_m/G_f} \right] \quad (26)$$

$$\eta_4 = \frac{3 - 4v_f + G_m/G_f}{4(1 - v_m)} \quad (27)$$

More elaborated micromechanical analytical methods exist, as stated in the introduction. Moreover, the python script used to predict the mechanical properties is presented in Appendix A. Python script for composite mechanics and data repository

4.5.2 Two Steps Numerical Homogenization.

RVE allow us to describe a material point in a heterogeneous continuum by explicitly modeling the inhomogeneities at small scales, considering two requirements. First, the RVE must be small enough from a macroscopic view to be considered a material point, yet it must also be large enough to reveal the microscale voids, constituents (L_{const}), and average distributions.

$$L_{const} \ll L_{RVE} \ll L_{macro} \quad (28)$$

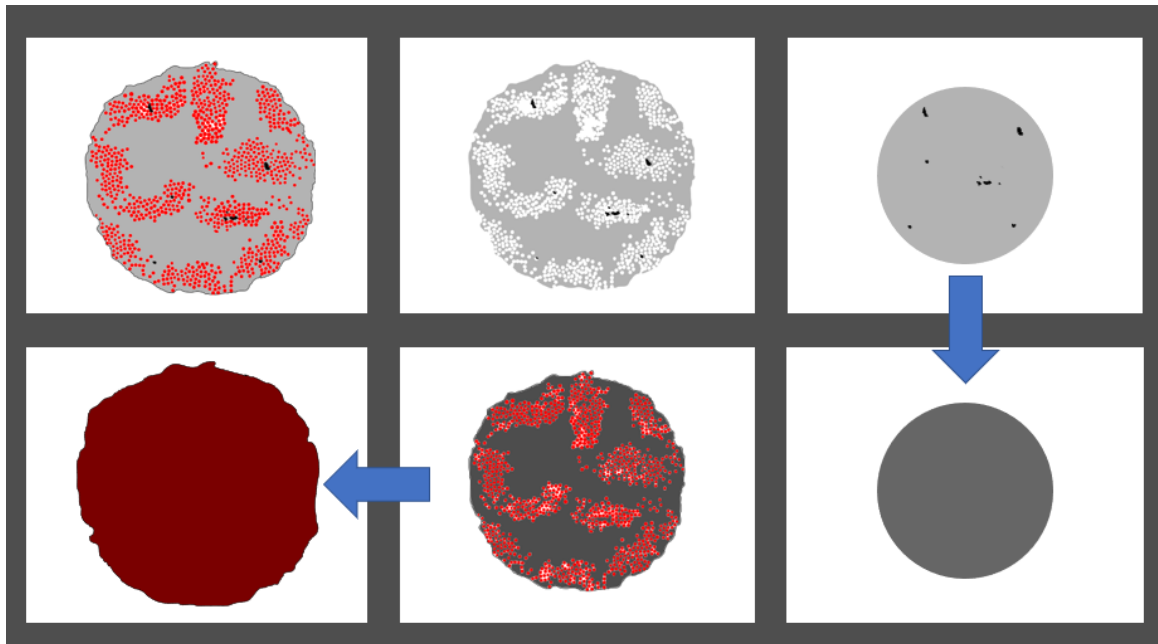
The equation (28) is known as the Hashin Inequality. If it is satisfied, then the Hill principle can be applied. Hill Principle states an equivalence in work done in the microstate integrated over the volume of the RVE and the work done in the macro scale as stated by equation (29).

$$[\bar{\sigma}]: [\bar{\epsilon}] = \frac{1}{V} \int [\sigma]: [\epsilon] dV \quad (29)$$

Therefore, macroscopic quantities can be related to microscopic quantities. From the scanning electron microscope (SEM) images, the microstructure of the filaments was obtained, as well as, the 3D printed part, and the load-tested component. However, the images usually have defects such as blur zones, out-of-focus regions, or inadequate brightness, which turn challenging to analyze by the software, so vectorized images are created from an actual image using Inkscape software. Then, MIDAS-VT (Microstructure Inelastic Damage Analysis Software-Virtual Tester) (Zare-Rami & Kim, 2019) is employed to perform the image segmentation, model extraction, and mesh generation. Finally, the mesh model is imported to ANSYS, which performs the static structural analysis of the 2D geometry. This thesis proposes a two-step homogenization scheme to find the RVE and the macroscopic properties. The process is illustrated in Figure 19.

Figure 19

Two-step homogenization process schematics of a transverse section of a composite filament spool

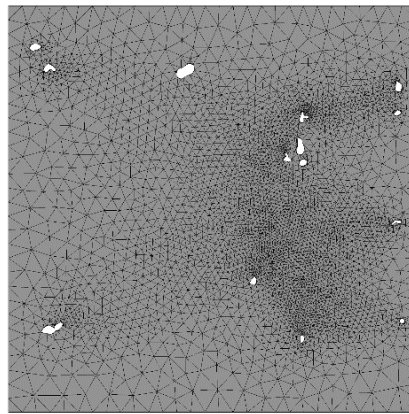


First, the general transverse section is divided into 3 phases: matrix, reinforcements, and voids. Then, the matrix and the voids are homogenized in a reduced area to account for the reinforcement area, showing a bulk material property different from the bulk matrix. Secondly, the first homogenized porous matrix and the reinforcement are homogenized in the overall behavior of the composite. The material properties of the bulk and the homogenized matrix are depicted in Table 5.

The homogenized matrix with porosities, Figure 20, is slightly more compliant and has a similar Poisson ratio. Note that the void distribution could lead to an anisotropic behavior if they have a preferred orientation. However, from SEM analysis, it is unlikely to be the case.

Table 5*Properties of the bulk and homogenized matrix*

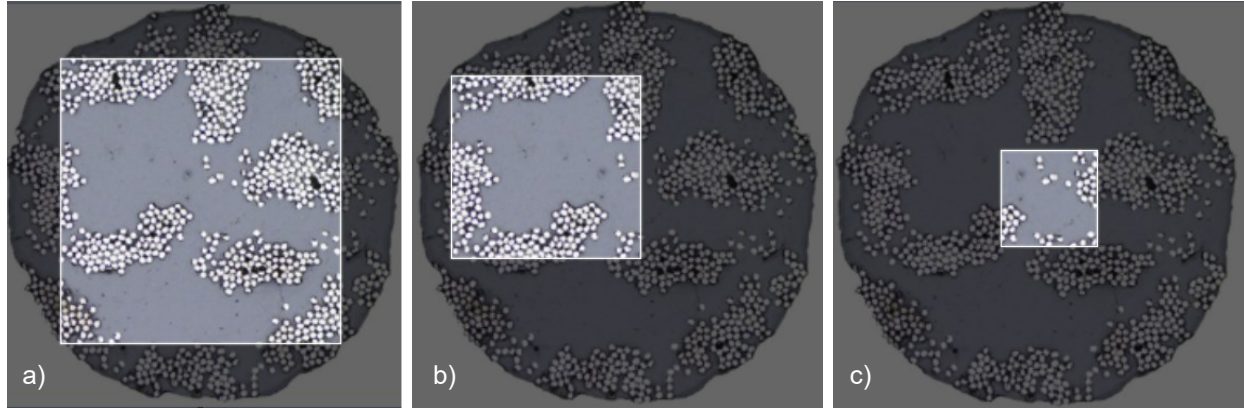
Property	Bulk matrix	First step homogenization
E (MPa)	1700	1632
ν	0.390	0.394

Figure 20*Mesh of the porous matrix, numerical homogenization model*

In the second step of homogenization, the homogenized matrix is mixed with the fibers to obtain the overall composite behavior, and it is noted that in the composite filament, the RVE would be quite large, provided that there is no repeating unit because fibers are disposed of in bundles, see Figure 21. This fact can be corroborated using the histograms of the SEM images. Therefore, the RVE must be very similar to the whole part; moreover, from Figure 22, notice that histograms are different. Also, the medium-sized histograms present overlapping regions due to the relatively big size.

Figure 21

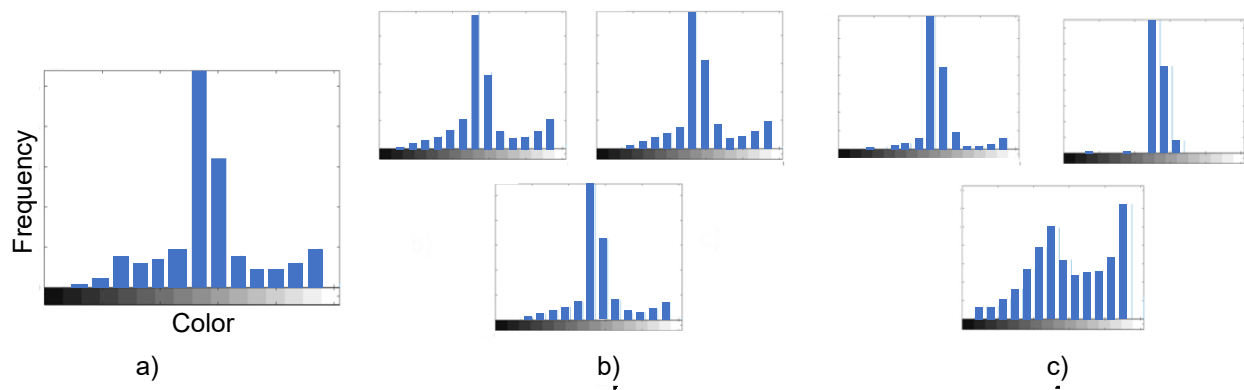
View of the selected image sizes: a) big square region, b) medium size region, c) small region



One could observe that the histograms for the medium size are similar between them and to the histogram of the big square. On the contrary, the small images present very different histograms. Therefore, the Hill principle in equation (28) is not satisfied, and the spool does not present an RVE. This analysis applies to the fiber reinforcement filament and not the printed part.

Figure 22

Histogram of the different spool images: a) big-sized region, b) medium size, c) small size

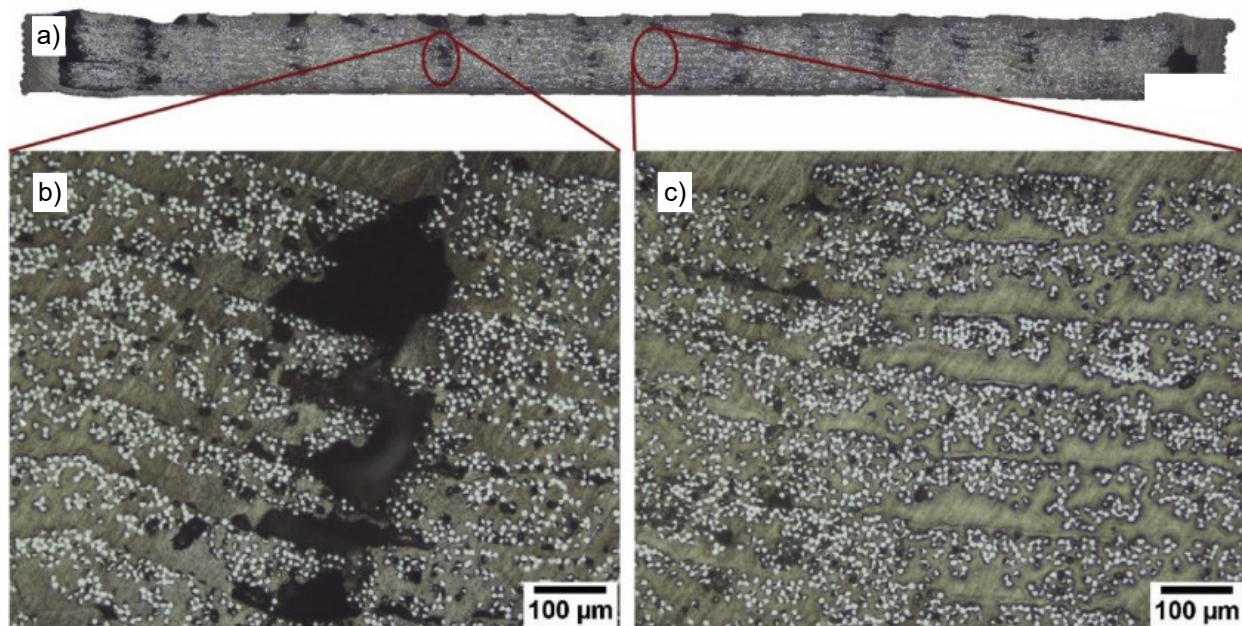


Note: The axis legend for the b) and c) graphs are identical to a), they are omitted for simplicity.

In Figure 23, the printed part microstructure (Chabaud et al., 2019) is observable. Given a high portion of porosities, when printing, the intrafilaments porosities represent a small fraction due to high inter-bead porosities.

Figure 23

Cross-section view of fiberglass reinforced AM part a) general view and magnifications, b) area where printed beads are not overlapped c) area with overlapped printed beads



Source:(Chabaud et al., 2019)

Chabaud states the process in the following manner:

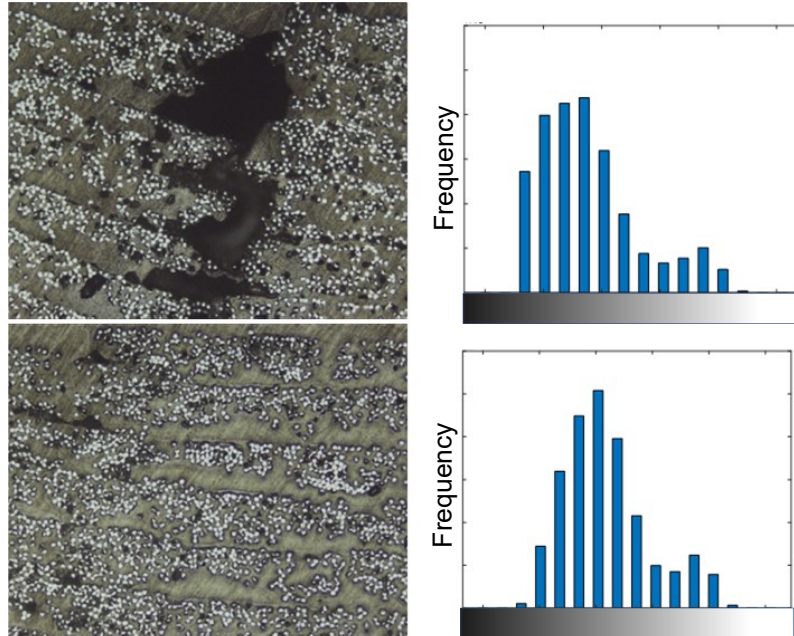
"During the printing process, the filaments underwent a flattening. As a result, the 379 μm and 332 μm wide filaments become layers with thicknesses of 127 μm and 101 μm for continuous carbon and glass fiber polyamide composites, respectively, thus dividing by three the initial filament size."

These characteristics are common to AM, such that they are characterized as singularities of the process, not as defects of manufacturing, meaning they must be considered in the design process.

Figure 24 shows the histogram of two different zones of continuous glass fiber composite. As they are very dissimilar, other pairs of images are expected to present lower differences than those presented in the figures. Following the same procedure, one could extract sub-images and evaluate them in their histograms. By making this procedure, an RVE size of the composite in the range of $[300 \mu m \times 300 \mu m]$ to $[900 \mu m \times 900 \mu m]$ was found. The details can be found in Appendix B. Histograms of the selected micrographs. However, considering that each reinforcement layer can have a different angle fiber orientation, the size of one layer would be the maximum allowable size. Thus, implying that the RVE should be a rectangle with sizes of 100 micrometers \times 900 micrometers. Once a range of valid histograms is found, it is possible to further refine the range by numerical homogenization.

Figure 24

Extracted micrographs and histograms of a fiberglass FRAM part



4.6 Strength Characterization

While the elastic properties can be calculated from model assumptions, there is no apparent relationship for strength characterization, although strength characterization shares some aspects with stiffness properties, such as:

- They are axis-oriented (anisotropic), implying that the strength in the longitudinal direction is generally not the same as in the transverse direction.
- They are usually in between the strength properties of the matrix or the reinforcements.

Contrary to the stiffness, there is no established way to calculate the strength of the materials. Also, they are bilateral, meaning strength in compression is not the same as tension.

This section presents the characterization of a single lamina strength, and multidirectional laminates are presented further.

There are numerous failure mechanisms in AM composites. Thus, predicting the strength of a single ply is a challenging problem, more demanding than the stiffness determination. Despite this fact, this work proposes to use simple equations for traditionally manufactured composites. Those formulations are also micromechanical based on the equations presented from equation (22) to equation (27). However, they generally depend on the properties of the constituent and a back-calculation parameters, thus being semi-empirical. One formulation to obtain the longitudinal tensile strength (F_{1T}) is depicted in equation (30) (Barbero, 2011), which assumes that all fibers have the same strength represented by the apparent fiber tensile strength F_{fT} , in spite, some authors have found this erroneous as the strength of the fibers presents a Weibull distribution (Pascual-González et al., 2020). Also, it supposes a linear behavior up to the point of failure.

$$F_{1T} = F_{fT} \left[V_f + \frac{E_m}{E_f} (1 - V_f) \right] \quad (30)$$

Longitudinal compressive strength (F_{1C}) can be estimated by a simple equation given in equation (31) and equation (32) (Barbero, 2011).

$$F_{1C} = G_{12} (1 + 4.76\chi)^{-0.69} \quad (31)$$

$$\chi = \frac{G_{12}\alpha_\sigma}{F_6} \quad (32)$$

Where α_σ is the standard deviation of fiber misalignment, which can be measured experimentally (Yurgartis, 1987) or calculated from equation (31) based on experimental data for F_{1C} . And apply it to extrapolate to composites of different volumetric fiber fractions.

The transverse tensile failure of a unidirectional lamina occurs after a transverse crack propagates along the fiber direction, thus, splitting the lamina. Equation (33) (Barbero, 2011) is used to predict the transverse tensile strength (F_{2T}) of a unidirectional lamina.

$$F_{2T} = \sqrt{\frac{G_{IC}}{1.12^2 \pi (t_t/4) \Lambda_{22}^0}} \quad (33)$$

Where G_{IC} is the fracture toughness in mode I, t_t the transition thickness, which can be approximated as $t_t = 0.6$ mm, 0.8 mm, for E-glass–epoxy and carbon–epoxy composites, respectively. However, G_{IC} and t_t are not well established for FRAM composites. Finally, Λ_{22}^0 is given by equation (34) (Barbero, 2011).

$$\Lambda_{22}^0 = 2 \left(\frac{1}{E_2} - \frac{v_{12}^2 E_2^2}{E_1^3} \right) \quad (34)$$

Older and simpler empirical formulas derived without consideration for fracture mechanics are also available (Barbero, 2013). For example, for the transverse tensile and compressive strength, empirical formulas are given in equation (35) and equation (36).

$$F_{2T} = F_{mT} C_v \left[\left(1 - V_f^{\frac{1}{3}} \right) \left(\frac{E_2}{E_m} \right) \right] \quad (35)$$

$$F_{2C} = F_{mC} C_v \left[1 + (V_f - \sqrt{V_f}) \left(1 - \frac{E_m}{E_t} \right) \right] \quad (36)$$

The apparent compressive strength of the matrix, F_{mC} , is back-calculated from experimental data on F_{2C} using equation (36). C_v is an empirical factor which adjust for the presence of voids (V_V), finally, E_t is the transverse modulus of the fiber.

$$C_v = 1 - \sqrt{\frac{4V_v}{\pi(1 - V_f)}} \quad (37)$$

F_6 , the in-plane shear strength can be approximated using equation (38) if more experimental data is available for determining the F_{mS} and C_v factors. G_a is the axial shear modulus of the fiber, which in the case of isotropic fibers is equal to G_{12}

$$F_6 = F_{mS} C_v \left[1 + (V_f - \sqrt{V_f}) \left(1 - \frac{G_m}{G_a} \right) \right] \quad (38)$$

Intralaminar shear strength F_4 is a property dominated by the matrix partly because the shear stress acts on a plane parallel to the fiber direction. Equation (39) (Barbero, 2011) depicts F_4 in terms of the transverse compressive strength F_{2C} and the angle of the fracture plane α_0 .

$$F_4 = F_{2C} \cos \alpha_0 (\sin \alpha_0 + \cos \alpha_0 \cot 2\alpha_0) \quad (39)$$

4.7 Ply and Laminate Mechanics

Composites plies are orthotropic in their mechanical behavior, meaning they are three planes of symmetries perpendicular to each other. Recalling the elastic behavior of an orthotropic solid given in equation (54) and giving the symmetry of the compliance and the stiffness matrices, the result is reproduced in equation (40).

$$[\mathbf{S}] = \begin{bmatrix} \frac{1}{E_1} & -\frac{\nu_{12}}{E_1} & -\frac{\nu_{13}}{E_1} & 0 & 0 & 0 \\ -\frac{\nu_{12}}{E_1} & \frac{1}{E_2} & -\frac{\nu_{23}}{E_2} & 0 & 0 & 0 \\ -\frac{\nu_{13}}{E_1} & -\frac{\nu_{23}}{E_2} & \frac{1}{E_3} & 0 & 0 & 0 \\ 0 & 0 & 0 & \frac{1}{G_{23}} & 0 & 0 \\ 0 & 0 & 0 & 0 & \frac{1}{G_{13}} & 0 \\ 0 & 0 & 0 & 0 & 0 & \frac{1}{G_{12}} \end{bmatrix} \quad (40)$$

The composite ply needs nine $(E_1, E_2, E_3, G_{12}, G_{23}, G_{13}, \nu_{12}, \nu_{13}, \nu_{23})$ independent constants to fully characterize its behavior. Usually, a reduced form of the equation (40) is presented in the assumption of a plane stress state giving the low thickness of a composite ply, and equation (41) and equation (42) state the reduced elastic law before mentioned.

$$\begin{Bmatrix} \varepsilon_1 \\ \varepsilon_2 \\ \gamma_6 \end{Bmatrix} = \begin{bmatrix} \frac{1}{E_1} & -\frac{\nu_{12}}{E_1} & 0 \\ -\frac{\nu_{12}}{E_1} & \frac{1}{E_2} & 0 \\ 0 & 0 & \frac{1}{E_3} \end{bmatrix} \begin{Bmatrix} \sigma_1 \\ \sigma_2 \\ \sigma_6 \end{Bmatrix} \quad (41)$$

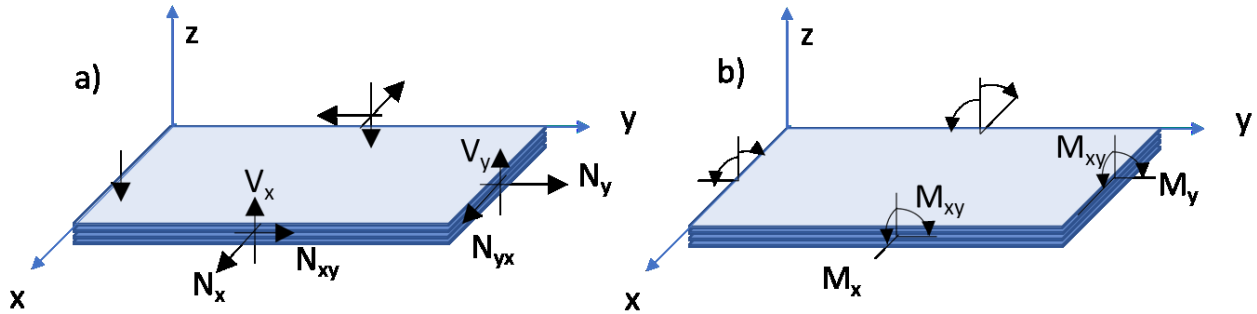
$$\begin{Bmatrix} \gamma_4 \\ \gamma_5 \end{Bmatrix} = \begin{bmatrix} \frac{1}{G_{23}} & 0 \\ 0 & \frac{1}{G_{13}} \end{bmatrix} \begin{Bmatrix} \sigma_4 \\ \sigma_5 \end{Bmatrix} \quad (42)$$

Fiber-reinforced parts are mainly reinforced in laminates, meaning with two or more plies, they can have woven, unidirectional, or not-aligned fibers forms. However, unidirectional plies stack up at different angles are mainly the way FRAM is reinforced. Stresses and strains of laminates can be found by the CLPT (classical laminate plate theory). In addition, there are other

formulations such as the FOSDT or the Second-order SDT. CLPT consists in determining an ABD matrix that can be considered analogous to the stiffness matrix, and the ABD matrix relates de forces ($\{N\}$) and moments ($\{M\}$) of a plate to its displacements ($\{\epsilon\}$) and curvature ($\{\kappa\}$), as can be inferred from equation (43) to equation (48) and Figure 25.

Figure 25

Resultants acting on a plate: a) forces per unit length, b) moments per unit length



$$\begin{Bmatrix} N_x \\ N_y \\ N_z \\ M_x \\ M_y \\ M_z \end{Bmatrix} = \begin{bmatrix} A_{11} & A_{12} & A_{16} & B_{11} & B_{12} & B_{16} \\ A_{12} & A_{22} & A_{26} & B_{12} & B_{22} & B_{26} \\ A_{16} & A_{26} & A_{66} & B_{16} & B_{26} & B_{66} \\ B_{11} & B_{12} & B_{16} & D_{11} & D_{12} & D_{16} \\ B_{12} & B_{22} & B_{26} & D_{12} & D_{22} & D_{26} \\ B_{16} & B_{26} & B_{66} & D_{16} & D_{26} & D_{66} \end{bmatrix} \begin{Bmatrix} \epsilon_x^0 \\ \epsilon_y^0 \\ \gamma_{xy} \\ \kappa_x \\ \kappa_y \\ \kappa_{xy} \end{Bmatrix} \quad (43)$$

$$\begin{Bmatrix} V_y \\ V_x \end{Bmatrix} = \begin{bmatrix} H_{44} & H_{45} \\ H_{45} & H_{55} \end{bmatrix} \begin{Bmatrix} \gamma_{yz} \\ \gamma_{xz} \end{Bmatrix} \quad (44)$$

Where

$$A_{ij} = \sum_{k=1}^N (\bar{Q}_{ij})_k t_k; \quad i, j = 1, 2, 6 \quad (45)$$

$$B_{ij} = \sum_{k=1}^N (\bar{Q}_{ij})_k t_k \bar{z}_k ; \quad i, j = 1, 2, 6 \quad (46)$$

$$D_{ij} = \sum_{k=1}^N (\bar{Q}_{ij})_k \left(t_k \bar{z}_k^2 + \frac{t_k^3}{12} \right) ; \quad i, j = 1, 2, 6 \quad (47)$$

$$H_{ij} = \frac{5}{4} \sum_{k=1}^N (\bar{Q}^*_{ij})_k \left[t_k - \frac{4}{t^2} \left(t_k \bar{z}_k^2 + \frac{t_k^3}{12} \right) \right] ; \quad i, j = 4, 5 \quad (48)$$

The \bar{Q}_{ij} are the ij coefficients of the stiffness matrix, t_k the thickness of the k th layer, and z_k the z coordinate of the k th layer.

The B matrices are the coupling behavior of the matrix, and it is why it is usual to see angle plies, symmetric laminates, or balanced laminates in load-bearing parts. They reduce the coupling factor B, thus, making the thermal stresses in the manufacturing process less prone to cause thermal deflection when curing.

4.8 Performing Volume Average Stiffness Method

The volume average stiffness (VAS) model obtains the overall mechanical response of the part. It consists first in determining each constituent volume and its corresponding volumetric fraction using equation (49) to equation (52). Table 6 depicts the nomenclature used for describing the cross-sectional view and gives the values used for the experimental characterization.

Table 6

Nomenclature and used values for the VAS method.

Name	Symbol	Value and dimensions
Height	H	258.0 mm
Width	W	12.7 mm
Thickness	T	2.5 mm
Layer Thickness	T_{layer}	0.1 mm
Number of floor layers	N_{floor}	
Shell Width	W_{shell}	mm
Volume	V	mm ³
Volumetric fraction	V_f	dimensionless

The calculation of the volumes depends upon the geometrical and process parameters.

Those are depicted in Table 6.

$$V_{tensile} = HWT \quad (49)$$

$$V_{floor} = [W - (2W_{shell})]HT_{layer}N_{floor} \quad (50)$$

$$V_{fiber} = W_{fiber}HT_{layer}N_{concentric}2N_{fiber} \quad (51)$$

$$V_{infillfiber} = W_{infillfiber} T_{layer} H N_{fiber}$$

$$\text{With, } W_{infillfiber} = [W - (2W_{shell}) - (W_{fiber} 2N_{concentric})] \quad (52)$$

Ceiling, infill, and solid volumes are found by the same equation (50) but replacing the number of layers for the corresponding region. The volumetric fractions are obtained using equation (53). In which regions of infill, shell, fiber, solid, floor, or ceiling replace subscript i .

$$V_{fi} = \frac{V_i}{V_{tensile}} \quad (53)$$

The next step is to obtain the stiffness matrix of the individual regions. For the solid and shell regions, it is given by the generalized Hooke's law in a linear elastic solid. The model gives an orthotropic solid, which stiffness matrix is then given by equation (54).

$$[\mathbf{S}] = \begin{bmatrix} \frac{1}{E_1} & -\frac{\nu_{21}}{E_2} & -\frac{\nu_{31}}{E_3} & 0 & 0 & 0 \\ -\frac{\nu_{12}}{E_1} & \frac{1}{E_2} & -\frac{\nu_{32}}{E_3} & 0 & 0 & 0 \\ -\frac{\nu_{13}}{E_1} & -\frac{\nu_{23}}{E_2} & \frac{1}{E_3} & 0 & 0 & 0 \\ 0 & 0 & 0 & \frac{1}{G_{23}} & 0 & 0 \\ 0 & 0 & 0 & 0 & \frac{1}{G_{13}} & 0 \\ 0 & 0 & 0 & 0 & 0 & \frac{1}{G_{12}} \end{bmatrix} \quad (54)$$

In this thesis, the equations presented by (Gibson & Ashby, 1999) were employed with the different infill patterns and then characterized to obtain the mechanical properties, notably the compliance and stiffness matrices for different infill density values. Employing infill mechanical behavior could give a better estimate than using the model in (Melenka et al., 2016a).

For the composite section, a micromechanical model was employed. Then, for the different layers layup, the used stiffness model for the composite section was the classical laminate theory (CLT). Once all the stiffness matrices are found, they must be on the same axis, to do so, the use of rotation matrices could be needed. This is performed as depicted in equation (55) and equation (56).

$$[\mathbf{S}_{xyz}] = [\mathbf{T}]^T [\mathbf{S}] [\mathbf{T}] \quad (55)$$

$$[\mathbf{T}] = \begin{bmatrix} c^2 & s^2 & 0 & 0 & 0 & 2cs \\ s^2 & c^2 & 0 & 0 & 0 & -2cs \\ 0 & 0 & 1 & 0 & 0 & 0 \\ 0 & 0 & 0 & c & -s & 0 \\ 0 & 0 & 0 & s & c & 0 \\ -cs & cs & 0 & 0 & 0 & c^2 - s^2 \end{bmatrix} \quad (56)$$

Where $[\mathbf{T}]$ stands for transformation matrix, s , and c for sinus and cosines of the angle. The transformation must be performed because the fibers or the raster may not be aligned with the direction of the applied force.

Finally, all stiffness matrices are summed up by considering their corresponding volumetric fractions, as shown in equation (57).

$$[\mathbf{C}^G] = V_{fshell} [\mathbf{C}_{shell}] + V_{finfill} [\mathbf{C}_{infill}] + V_{fsolid} [\mathbf{C}_{solid}] + V_{ffiber} [\mathbf{C}_{fiber}] \quad (57)$$

In order to determine the effective engineering properties, the general stiffness matrix is inverted into the general compliance matrix, and the engineering constants are then found as indicated in equation (58) and equation (59).

$$[\mathbf{S}^G] = [\mathbf{C}^G]^{-1} \quad (58)$$

$$\{E_x \ E_y \ E_z \ G_{xy} \ G_{yz} \ G_{xz} \ \nu_{xy} \ \nu_{zx} \ \nu_{xy}\} == \left\{ \frac{1}{S_{11}^g} \ \frac{1}{S_{22}^g} \ \frac{1}{S_{33}^g} \ \frac{1}{S_{66}^g} \ \frac{1}{S_{44}^g} \ \frac{1}{S_{55}^g} \ \frac{-S_{12}^g}{S_{11}^g} \ \frac{-S_{13}^g}{S_{33}^g} \ \frac{-S_{23}^g}{S_{22}^g} \right\} \quad (59)$$

Numerical values of the model were obtained with an assumed porosity of 10 % (Pascual-González et al., 2020).

4.9 Conclusions of the material modeling

The proposed model extends the capabilities of the current VAS method, which is the stiffness prediction of the AM composite part. More accurate properties could be found by considering the geometrical factors in selecting the infill. However, further work must be done in characterizing different infill architectures and different volumetric ratios.

This work presents a modification of the VAS models, which accounts for the infill architecture and density ratio. Typically, the infill region has negligible influence on stiffness values; however, if the infill volumetric fraction increases, the error committed to considering the infill as a solid model with porosity could be significant.

This chapter presented the characterization of the reinforced layers in an AM composite. Analytical formulations for characterizing the composite reinforced layers are given, and this formulation is based on well-established micromechanical formulas for traditionally manufactured composites. Also, a two-step numerical homogenization method is presented to characterize a filament spool. The homogenization shows the reduction of the properties due to the intrafilamentary porosities. Despite the defects present, the results are similar within the bulk properties, allowing more confidence to apply the micromechanical-based formulas.

The micrographs show the microstructure of the filaments and the printed part. In the printed part, the flattening of the filament cause more even distribution of the fibers bundles. Moreover, the number of porosities increases due to defects such as interbead porosities, and these interbead porosities are a factor that explains why AM composited are less performing than traditional manufacturing composite laminates.

Furthermore, the present chapter shows the size of the RVE, thus, accomplishing the objective of determining the RVE size suitable for applying the progressive damage model, discriminating each material region's behavior.

The next chapter will address the experimental campaign results and the methodology for testing and analyzing the data. The role of manufacturing parameters will also be discussed.

5. Manufacturing Process Parameters Effects on the Mechanical Response

In the previous chapter, the methods for characterizing the stiffness and strength of the reinforced region were presented, the experimental campaign was stated, and the micromechanical formulation was presented. The present chapter presents the results of the experimental setup and analyzes them in terms of an experimental design approach. Also, machine learning algorithms are used for comparison with an analytical method such as the micromechanical formulation.

Selecting the optimal construction parameters of FRAM is a difficult task, as the number of parameters on which the FRAM mechanical behavior and failure mechanisms depend grows in number. Experimental work and FE models covering all the possible spectra would not be feasible.

Consequently, one approach to solve the problem is using artificial intelligence and data-driven models to predict the properties or design optimal FRAM architectures. Machine learning is becoming a powerful tool to tackle challenging problems. As a drawback, a large amount of data is required to train a predictive model. Some authors use deep learning to predict the strength of AM parts, and this approach could be used for FRAM parts. Zhang et al. (J. Zhang et al., 2019) predict the tensile strength of FFF PLA thermoplastic, and as input data, authors have the time process variations characterized by inter-layer interactions. The model is constructed using the layerwise process signals (vibration and temperature) as inputs of a long short-term memory LSTM network, a subtype of recurrent neural networks (RNN). Later, in (Z. Zhang et al., 2020) the authors perform the strength prediction for a composite AM sample, developing different machine learning algorithms such as least absolute shrinkage and selection operator (lasso), K-nearest neighbors, and support vector machines. Their input parameters were the number of fiber layers, polymer layers, fiber rings, and infill patterns. Other authors employ deep learning to optimize fiber paths and reverse engineering of AM parts (Yanamandra et al., 2020) or enhance the mechanical strength of FFF polymers by selecting the optimum process parameters (Chohan et al., 2020), showing a highly competitive with other optimization algorithms.

As an impact of this research, micromechanical and data-driven models were compared. This labor has not been done on continuous FRAM data. The first predictive model, a micromechanical-based, employs standard formulas to predict their macroscopic response. The models are presented in chapter 4. Then, different machine learning algorithms in which trained models for regression predict the stiffness and strength are presented. After establishing the models, the data obtention and curation methodology and the available data set are introduced. Finally, an experimental tensile test was conducted on continuous carbon fiber AM composites

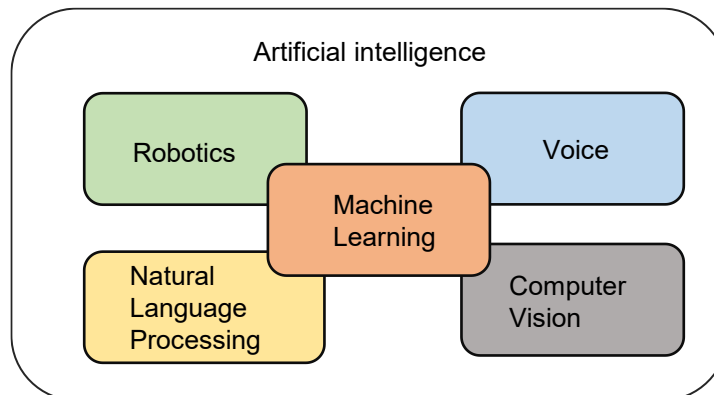
varying their reinforced fraction, printing direction, and fiber angle. Models are evaluated regarding the accuracy, ease of implementation, and generalization capabilities. The fractographic analysis also shows a qualitative view of the microstructure and failure surface topology.

5.1 Data-Driven Models

Artificial intelligence (AI) is a hard to define subject, mainly because of our understanding of intelligence. However, for a practical definition, it is possible to state that artificial intelligence is a subfield of informatics that creates machines that imitates intelligent behavior. Although this broad definition could accommodate a robot that performs a repetitive task being programmed, and it was considered an intelligent action. Nowadays, machine learning seems to be the core area of AI. Figure 26 shows the application areas of AI.

Figure 26

Areas of artificial intelligence



Machine learning is subdivided into supervised, unsupervised, and reinforced learning. Supervised learning uses labeled data to train the model, while unsupervised learning lacks labeled data. Reinforcement learning is a reward-based learning type. The present time is characterized by a dive in the information era, with the arrival of digitalization, the cost reduction of processing and

storage devices, a mind shift towards the value of data, and the tendency to accumulate large amounts of data, known as Big Data. Data-driven models represent cyber-physical systems that employ numerous data to perform predictions, classifications, or clusterization. In this aspect, a machine learning model is a data-driven model.

This thesis interest is in predicting the mechanical properties of AM composites. It is, therefore, a regression problem, which is a kind of supervised learning. Numerous regression techniques include simple linear regression models, regression trees, support vector machines, Gaussian process regression models, and neural networks (Kutner et al., 2005). These models were tested in the regression learner app from the Machine learning and statistics Toolbox of MATLAB software, version 2021. To avoid overfitting, the data set is partitioned into five cross-validations folds and estimates each fold's accuracy.

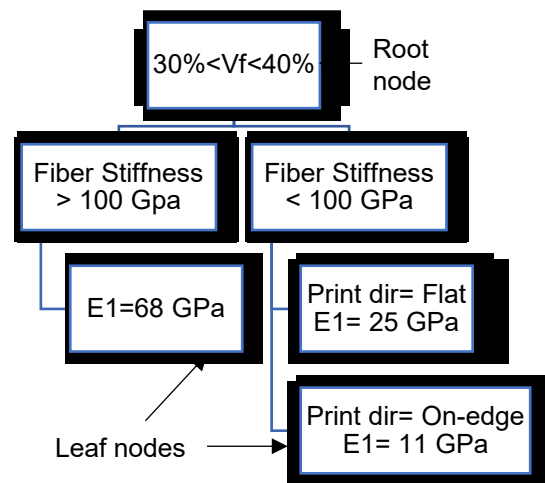
As each model has distinct notations and names for the variables, a consensus is presented here. Denoting by $[X]$ the design matrix, also called the training matrix, data matrix, or input matrix, where it contains the complete input dataset, and the columns correspond to each point in the feature space (training sample) and the rows to each factor. Therefore, it is, in a general way, a non-square matrix. The number of explanatory variables, or factors p , is the number of rows of $[X]$, while the number of points m is the number of columns. The variable y is the output, response, or predictor value. It is a column vector ($\{y\}$), in which each row is associated with the corresponding column or feature vector in the data matrix $[X]$. w are the coefficients of the variables in the model, also called weights. ε is the error associated with the model. b is a constant value, a bias which is a scalar.

5.1.1 Decision Trees

Regression trees predict responses to data by following a series of decisions in the tree, from the root (beginning) node down to a leaf. The leaf node contains the response. Figure 27 present an example of a simple regression tree.

Figure 27

Representation of a simple regression tree



5.1.2 Linear Regression

Linear regression models describe the relationship between the explanatory variables and the response variable. In general, a linear regression model can be a model of the form represented in equation (60). Note that they are linear in the unknown coefficients w_k .

$$y_i = w_0 + \sum_{k=1}^k w_k f_k(x_{1i}, x_{2i}, \dots, x_{pi}) + \varepsilon_i \quad (60)$$

Where $f(\cdot)$ is a scalar-valued function of the independent variables x_{ji} . The functions might be in any form, including nonlinear functions and polynomials. Two examples of linear models are depicted in equation (61) and equation (62).

$$y_i = w_0 + w_1x_{1i} + w_2x_{2i} + \varepsilon_i \quad (61)$$

$$y_i = w_0 + w_1x_{1i} + w_2x_{2i}^2 + \varepsilon_i \quad (62)$$

However, the following, equation (63) and equation (64) are not linear in the unknown coefficients $\{w\}$

$$\log y_i = w_0 + w_1x_{1i} + w_2x_{2i} + \varepsilon_i \quad (63)$$

$$y_i = w_0 + \frac{1}{w_1x_{1i}} + e^{w_2x_{2i}} + \varepsilon_i \quad (64)$$

5.1.3 Support Vector Machines

SVM is a nonparametric technique relying on kernel functions. Kernels are transformations of the representation plane that linear transformations of the factors can do. MATLAB regressor app implements linear ε -insensitive SVM (ε -SVM) regression. The goal is to find a function $f(x)$ that deviates from the prediction value \hat{y}_i by a value no greater than ε for each training point x_i and at the same time is as flat as possible, this can be evidenced in the primal formula for the SVM. In equation (65), to find a linear function:

$$f(x) = \{w\}^T [X] + \{b\} \quad (65)$$

And ensure that it is as flat as possible, find $f(x)$ with the minimal norm value $\{w\}^T \{w\}$ formulating a convex optimization problem that must minimize the cost function J of equation (66)

$$J(w) = \frac{1}{2} \{w\}^T \{w\} \quad (66)$$

Subject to the residuals being less than an arbitrary threshold, ε in equation (67), that is:

$$\forall n: |\hat{y}_i - (\{w\}^T [\mathbf{X}] + \{b\})| \leq \varepsilon \quad (67)$$

In regression, SVM creates the best “bands,” in which most of the points lie in that region.

It works well if there the data dispersion is low.

5.1.4 Gaussian Process Regression

It works by extending the idea of probability functions of numbers to probability distributions of functions. If the available data set is drawn from an unknown distribution. A Gaussian process regression (GPR) model addresses the question of predicting the value of a response variable \hat{y} , given the new input vector x_{new} , and the training data. A linear Gaussian regression model is of the form given by equation (68)

$$\hat{y} = \{w\}^T [\mathbf{X}] + \{\varepsilon\} \quad (68)$$

where $\{\varepsilon\}$ follows a normal distribution probability $N(0, \sigma^2)$. The error variance σ^2 and the coefficients $\{w\}$ are estimated from the data. A GPR model explains the response by introducing latent variables, $f(x)_i, i = 1, 2, \dots, n$ from a Gaussian process (GP) and explicit basis functions. A GP is a set of random variables, such that any finite number of them have a joint Gaussian distribution. If $\{f(x), x \in R^d\}$ is a GP, then given n observations x_1, x_2, \dots, x_n the joint distribution of the random variables $f(x_1), f(x_2), \dots, f(x_n)$ is Gaussian.

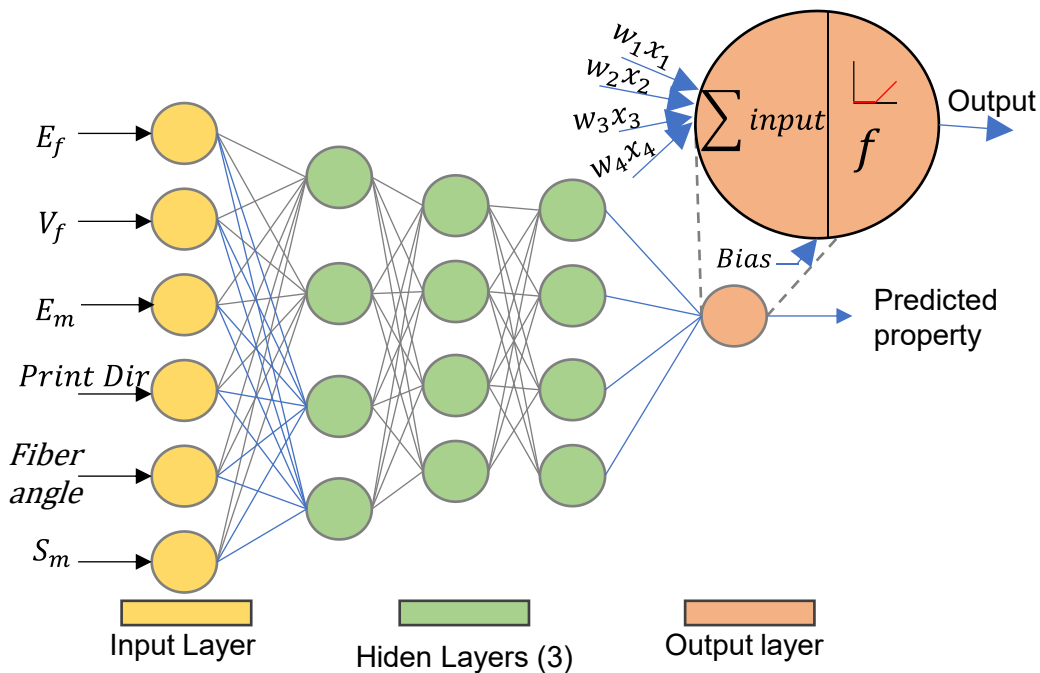
5.1.5 Artificial Neural Networks

Artificial Neural networks (ANN) get their name by the resemblance to a neuron, a biological cell, in which usually more than one stimulus enters the neuron, and the response output

connects to other neurons in the network. See Figure 28. Raw data can be used to train and test an artificial neural network. The input layer consists of a row vector of dimension 9,1 of a set of parameters, namely: {Fiber stiffness, Fiber Strength, Fiber Poisson's ratio, Fiber angle, matrix stiffness, matrix strength, matrix Poissons ration, printing direction, volumetric fiber fraction}. The output is a column vector identifying the stiffness or the tensile strength of such AM parts. The proposed Neural network has hidden layers, using ReLu (Rectified Linear Unit) for the activation function in all the hidden layers.

Figure 28

Schematic of the artificial neural network



The output of a single neuron is determined by their inputs, and the activation function as equations (69) and (70) shows

$$\{z\} = \{w\}^T[\mathbf{X}] + \{b\} \quad (69)$$

$$\{a\} = f(\{z\}) \quad (70)$$

The $f(\{z\})$ function is called the activation function of the neuron; it can be a $\tanh(z)$ or sigmoid function or a rectified linear unit function ReLU. The error function ($\mathcal{L}(\hat{y}, y)$) employed to evaluate the ANN is given in equation (71), and employed in the gradient descent formulation

$$\mathcal{L}(\hat{y}, y) = -(y \log y + (1 - y) \log(1 - \hat{y})) \quad (71)$$

While the cost function $J(w, b)$, which is the parameter to minimize, is given by equation (72)

$$J(w, b) = \frac{1}{m} \sum_{i=1}^m \mathcal{L}(\hat{y}^{(i)}, y^{(i)}) \quad (72)$$

5.2 Experimental Methodology and Design of Experiments

Data was gathered from numerous available journal papers and our experiments. The raw data used is available as an annex. Our experimental test was performed using ASTM D3039 (ASTM, 2014) to determine tensile behavior. A design of experiments is proposed as Table 7 shows the experimental Latin square.

The design of the experiment table was proposed with three factors, with various levels at each factor. Although a standardized design of the experiment was not suitable due to the uneven distribution of levels in each factor from manufacturing constraints, at least four specimens per point were tested, accounting for 52 samples, see Table 8.

Table 7*Information of the three factors DOE*

Factor	Levels	Values
Print direction	2	Flat and on-edge
Fiber type	1	Carbon fiber, continuous aligned fibers
Fiber fraction	3 (flat) or 4 (on-edge)	Low, medium, high, see Table 9
Orientation	3 (flat), 1 (on-edge)	Depending on the print direction

Table 8*Specimen distribution in DOE*

Print Direction	Fiber type	Fiber fraction	Orientation	Total test
Flat	Carbon iso	3	0°, 45°, 90°	9
On-edge	Carbon iso	4	0°	4
Total				13 * 4 replica

MarkTwo desktop printer fabricates the specimens of dimensions 150 mm × 15 mm × 2 mm with a Nylon white matrix and a continuous carbon fiber reinforcement. The total number of layers is 16 in the flat direction and 110 in the on-edge direction. Each layer has 1.25 mm in thickness. The fiber fraction levels are divided into three levels, as depicted in Table 9.

Table 9*Composite reinforced layers for each block and their volumetric fraction*

Print direction	Number of reinforced layers	Volumetric fiber fraction (%)
Flat	2, 4, 6	3.75, 7.50, 11.25
On-edge	28, 42, 55, 70	2.60, 3.90, 5.22, 6.53

Samples are then tested in an MTS Bionix 370.02 with a mechanical extensometer for determining the elastic response accurately. The chosen gripping method was cloth, as (Pyl et al., 2018) show the low variance of the results. The testing test speed was 2 mm/min.

5.3 Experimental Results and Model Comparison

The average results and coefficient of variation of our experimental data can be observed in Table 10. The data was analyzed through factorial DOE analysis and ANOVA. As a result, the following hypothesis were found: in the flat printing direction, the fiber angle, fiber content, and their interaction affect the average stiffness response (p-value 1.32 E-11). In the on-edge printing direction, the fiber content affects the average strength response (p-value 0.34) and stiffness response (p-value 0.01).

Table 10*Results for continuous carbon fiber reinforced Nylon White*

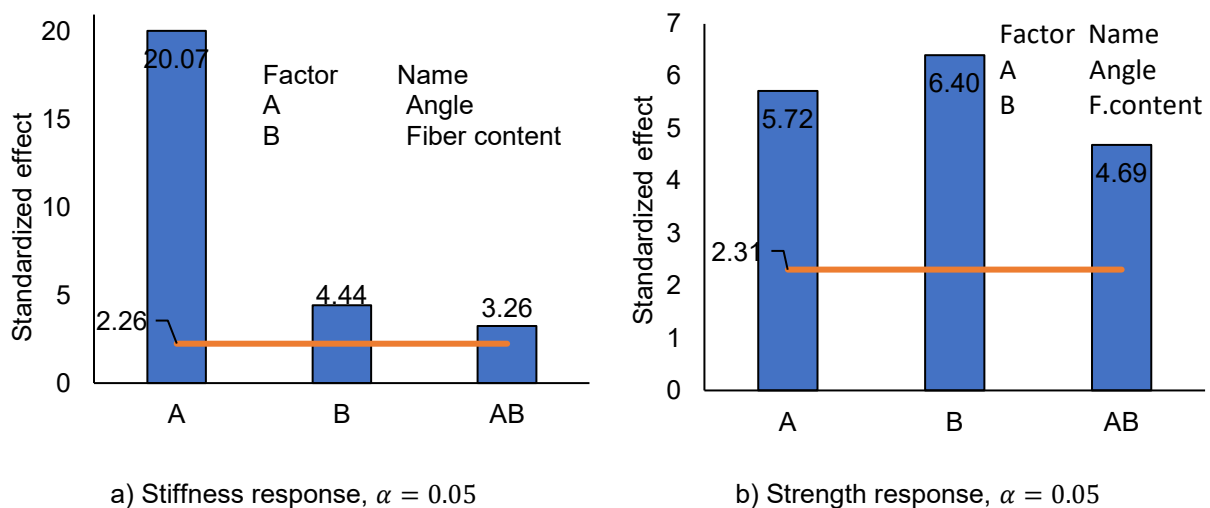
Reinforced layers - total layers	Fiber angle	Young's modulus (MPa)	COV (%)	Max. stress (MPa)	COV (%)
Carbon fiber flat					
2-16	0°	7232.5	6.7	67.57	44.4
4-16	0°	15204.0	0.5	198.83	11.9
6-16	0°	21896.5	12.7	209.35	29.2
2-16	45°	663.0	0.5	18.44	0.5
4-16	45°	969.6	14.2	19.15	4.0
6-16	45°	1789.0	24.3	19.08	18.4
2-16	90°	503.5	8.3	16.67	4.0
4-16	90°	727.3	19.3	15.39	1.8
6-16	90°	1052.3	7.9	15.85	9.9
Carbon fiber on-edge					
28-110	0°	4893.3	1.7	47.61	27.4
42-110	0°	7738.8	36.9	46.30	17.7
55-110	0°	7855.8	38.1	57.14	25.7
70-110	0°	13258.0	6.4	63.00	39.3

From the coefficient of variation (COV) column it is appreciable that the Young's modulus has a significant dispersion ranging from 0.5% to 24.3% in the flat printing direction and from

1.7% to 38.1% in the on-edge printing direction. The max stress also presented large dispersion, but in some cases it was lower than the dispersion seen in the Youngs modulus. COV for max stress ranges from 0.5% to 44.4% in the flat printing direction, and between 17.7% to 39.4% in the on-edge print direction. Figure 29 shows the Pareto diagrams of the effects angle and fiber content in the stiffness and strength, thus finding that the critical effect in the stiffness is the fiber angle, while fiber content is more determining for strength fiber content.

Figure 29

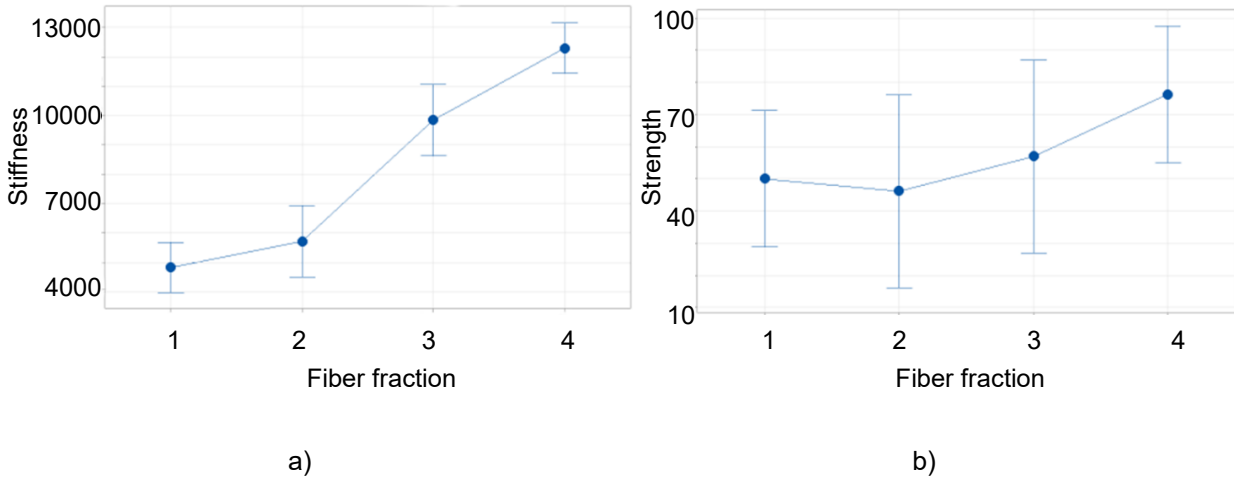
Pareto charts of the standardized effects for the angle, fiber content, and their interaction in the:
a) stiffness, and b) strength



In the On-edge printing case, the angle is not a factor because it is only possible to print a 0-degree coupon. Figure 30 shows the stiffness and strength interval graphs, while Figure 31 shows the residues plot.

Figure 30

Interval graphs for: a) stiffness (MPa) and, b) strength (MPa) of on-edge specimens with 95% CI for mean

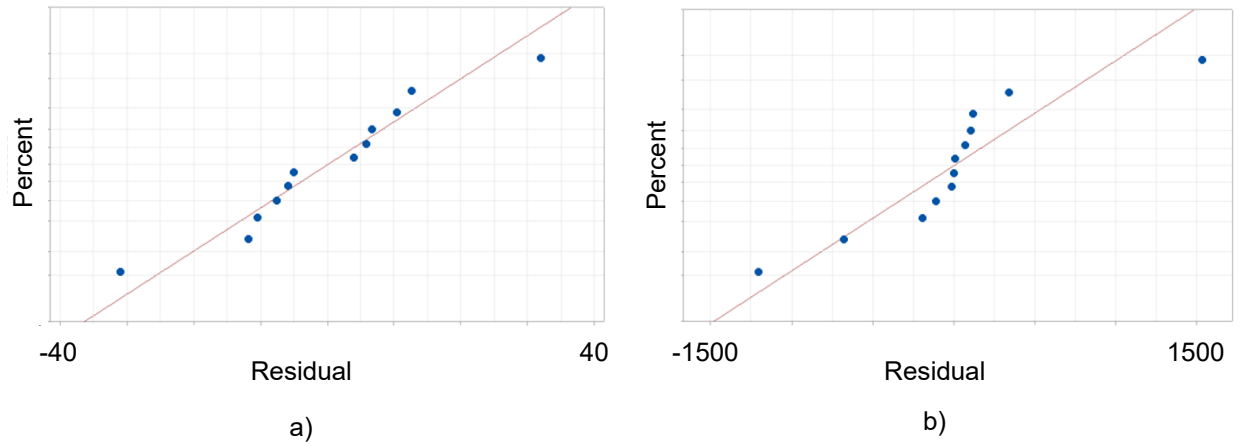


As mentioned before, the dispersion is large, thus the error bars in the graph are of a considerable size. In the on-edge printing direction, there is a tendency of increasing stiffness for the increment in the fiber fraction level, for the on-edge printing. However, it is not possible to affirm such statement for the case of the strength, provided the large dispersion and the large p-value (0.34). Comparing the two printing directions, it is possible to affirm that the flat direction is stronger than the on-edge direction, given the same fiber angle and fiber content.

The residues plot of Figure 31 shows a good agreement of the residues of error to a normal probability plot, thus indicating that the error is gaussian in his distribution. If that was not the case, transformations such as Box-Cox are helpful in converting non normal error distribution for an ANOVA analysis

Figure 31

Normal residue plots for: a) stiffness, b) strength



After analyzing the experimental data, a comparison with the micromechanical models is performed. First, the comparison of the Micromechanical model for stiffness prediction is based on the analytical formulations depicted in equation (22) to equation (27). However, the structure of the 3D printed samples is instead sandwich composites than truly fully composite structures because of the top and bottom layers that usually are printed from raw thermoplastic. In those cases, the volumetric average stiffness (VAS) method is employed to predict the overall behavior. Table 11 presents the estimation of the longitudinal and transverse modulus using micromechanical formulas and their comparison with experimental data (when available) in terms of the relative error.

Table 11

Longitudinal and transversal modulus comparison: experimental and micromechanics formulation for various samples

Coupon info	V_f fraction (%)	E_1 (VAS) model (GPa)	E_1 Exp. (GPa)	Relative error (%)	E_2 (VAS) model (GPa)	E_2 Exp. (GPa)	Source
Ccf-PA	3.8	8.60	7.23	16	1.77	0.50	This work
Ccf-PA	7.5	15.67	15.20	3	1.84	0.73	This work
Ccf-PA	11.3	22.73	21.90	4	1.91	0.99	This work
Ccf-PA ^a	2.6	6.86	4.89	29	1.74	NA	This work
Ccf-PA ^a	3.9	9.43	7.74	18	1.77	NA	This work
Ccf-PA ^a	5.2	12.05	7.86	35	1.79	NA	This work
Ccf-PA ^a	6.5	14.65	13.26	9	1.82	NA	This work
cCf-PLA	6.6	22.44	19.50	13	3.48	NA	(Melenka et al., 2016)
cJute-PLA	6.1	4.72	5.11	-8	3.43	NA	(Matsuzaki et al., 2016)
cCf-PA	6.0	15.02	14.00	7	2.98	NA	(der Klift et al., 2016)
cCf-PA	18.0	42.46	35.70	16	3.41	NA	(der Klift et al., 2016)
cCf-PLA	34.0	80.05	23.80	70	4.22	NA	(Li et al., 2016)
Ckv-PA	4.0	4.09	1.77	57	1.00	NA	(Melenka et al, 2016a)
Ckv-PA	8.0	7.25	6.92	5	1.02	NA	(Melenka et al, 2016a)
Ckv-PA	10.0	8.83	9.02	-2	1.04	NA	(Melenka et al, 2016a)
cCf-PLA	8.9	24.30	20.60	15	4.6	NA	(Tian et al., 2017)

Coupon	V_f	E_1 (VAS)	E_1 Exp.	Relative	E_2 (VAS)	E_2 Exp.	Source
info	fraction	model	(GPa)	error (%)	model	(GPa)	
	(%)	(GPa)			(GPa)		
cAramid-	8.6	9.52	9.34	2	3.55	1.53	(Bettini et al., 2017)
PLA							
Ccf-PA	27.0	63.34	62.50	1	4.44	NA	(Blok et al., 2018)
Ccf-PA	18.0	42.79	45.20	-6	3.00	NA	(Dutra et al., 2019)
Ccf-PA	27.0	63.34	NA	NA	2.32	3.53	(Dutra et al., 2019)
cCf-PLA	25.0	60.12	38.60	36	4.64	NA	(Azarov et al., 2019)
Ccf-PA	24.0	73.29	68.08	7	2.32	1.22	(Justo et al., 2018)
Cfg-PA	27.0	21.76	25.86	-18	1.28	1.22	(Justo et al., 2018)
Ccf-PA	13.5	41.97	37.00	12	1.96	NA	(al Abadi et al., 2018)
Ccf-PA	41.0	98.85	13.00	87	1.56	NA	(Goh et al., 2018)
Ccf-PA	35.0	81.10	7.20	91	1.44	NA	(Goh et al., 2018)
Ccf-PA	30.0	61.19	60.90	0	2.42	3.97	(Todoroki et al., 2019)
Ccf-PA ^b	30.0	2.42	2.40	1	NA	NA	(Todoroki et al., 2019)
Ccf-PA	21.3	50.33	47.56	5	2.16	NA	(Pyl et al., 2018)
Ccf-PA	24.8	58.32	57.09	2	2.26	NA	(Pyl et al., 2018)
Ccf-PA	7.2	18.14	31.65	-74	1.83	NA	(Pyl et al., 2018)
Cfg-PA	9.8	7.94	5.09	36	1.04	0.58	(Argawal et al., 2017)
Cfg-PA	19.5	14.87	8.92	40	1.16	1.61	(Argawal et al., 2017)
Ccf-PA	11.0	22.84	7.73	66	1.06	NA	(Dickson et al., 2017)

Coupon info	V_f fraction (%)	E_1 (VAS) model (GPa)	E_1 Exp. (GPa)	Relative error (%)	E_2 (VAS) model (GPa)	E_2 Exp. (GPa)	Source
Ckv-PA	10.0	8.45	4.37	48	1.04	NA	(Dickson et al., 2017)
Cfg-PA	10.0	8.05	3.75	53	1.04	NA	(Dickson et al., 2017)

Notes: a) on-edge printed, b) upright printed

The average relative error for the longitudinal modulus is 19%, with typical values between -18% to 70%. There are some outliers points with errors as -74% or 91%. Moreover, errors range from -38% to 71% for the transversal modulus with a 48% average error, despite the poor data availability. As the suggested values for the rest of the constants depend on the volumetric fiber fraction, look-up values are provided in Table 12.

Table 12

Suggested values of the engineering constants in continuous FRAM composites

Type	V_f (%)	E_3 (GPa)	ν_{12}	ν_{13}	G_{12} (GPa)	G_{13} (GPa)	G_{23} (GPa)
Ccf-PA	27	2.32	0.336	0.336	1.24	1.24	1.15
Cfg-PA	27	2.31	0.336	0.336	1.22	1.22	1.13
Ckv-PA	10	1.88	0.351	0.351	0.87	0.87	0.85
cCf-PLA	9	3.84	0.352	0.352	1.77	1.77	1.72
cJute-PLA	6	3.45	0.350	0.352	1.32	1.32	1.28

In the micromechanical properties, for the out-of-plane Poisson ratio ν_{23} a value between 0.28 and 0.35 for most FRAM is suitable due to the low inference in the structural response; however, a periodic microstructural model could be used to give a more precise approximation.

As a difference from the stiffness characterization, the obtention of the strength data is cumbersome as some factors can significantly influence the strength of AM composites. Different authors enunciated the effect of process parameters on the strength of the overall composite. Here, it is represented the effect of printing direction as Table 13 shows the strength comparison for our data. The predicted max. stress value was based on the equation (30) to equation (38).

It is observable a higher relative error with respect to stiffness prediction in Table 11. In addition, an apparent counter-intuitive trend is noted in the on-edge printing direction as the 28 layers version resisted a fair amount of stress, reaching close to 42 layers, a possible explanation is an effect the layer by layer adhesion has on the composite. Thus, implying that this damage mechanism is prevalent with the low volumetric fiber fraction on-edge printed composite.

Table 13

Processed data for strength comparison for FRAM

Flat printing direction				
Name	$V_f(\%)$	S_{uT} exp. (MPa)	Predicted S_{uT} (MPa)	Error (%)
0 2-16	3.75	93.24	92.34	0.96
0 4-16	7.50	198.83	171.47	13.76
0 6-16	11.25	209.35	250.59	19.70
90 2 16	3.75	16.67	17.77	6.21

90 4 16	7.50	15.39	15.95	3.50
90 6-16	11.25	15.85	14.70	7.80
On-edge printing direction				
Name	V_f (%)	S_{uT} exp. (MPa)	Predicted S_{uT} (MPa)	Error (%)
28-110	2.60	47.61	35.17	35.37
42-110	3.90	46.30	49.34	6.16
55-110	5.22	57.14	63.72	10.30
70-110	6.53	63.00	78.00	19.20

For the strength data, the retrieved back-calculated constants for use in equation (30) to equation (35) are depicted in Table 14 they came from this thesis work and the references given in Table 11.

Table 14

Retrieved back-calculated constants for FRAM

Type	F_{fT} (MPa)	F_{mT} (MPa)
Ccf-PA	2110, 1090 ^a	34.55
Cfg-PA	1185	49.10
cKv-PA	891	NA
Ccf-PLA	1749	NA

Note: a for on-edge printed

Those equations allow the calculation of the longitudinal and transversal tension strength for a given volumetric fiber fraction. However, there are limits to the practical volumetric fiber

fraction of the manufacturing method, with FFF AM of composite thermoplastic matrices employed. Furthermore, the strength and, to some extent, the stiffness of a composite can be influenced by the tabbing and grips. Wisnom (Wisnom, 1999) studied this effect extensively for traditional manufacture composites, while Pyl et al. (Pyl et al., 2019) show the influence of the architecture and gripping system on the stiffness and strength determination for FRAM.

The prediction models were compared according to three performance metrics: root mean square error (RMSE), the coefficient of determination R-squared, and the training time. Table 15 resumes the performance of the models for the stiffness and strength response. The model that predicts better the stiffness is the micromechanical-based with a RMSE of 6.81 and a R-squared of 0.74, while the second best was de Matern 5/2 GPR, a data driven model based on a Matern Kernel in a gaussian process regression, it has a RMSE of 10.91 and a R-squared of 0.66. The training time was very similar amongst the evaluated models, ranging from 0.8 to 5 seconds.

Table 15

Comparison of the models performance for stiffness and strength prediction

MODEL	Stiffness			Strength		
	RMSE (GPa)	R- Squared	Training Time(s)	RMSE (MPa)	R- Squared	Training Time (s)
Fine tree	16.859	0.19	3.76	167.53	0.55	0.835
Linear regression	14.984	0.36	3.95	183.31	0.46	0.946
Linear SVM	16.245	0.24	3.02	176.24	0.50	1.292
Gaussian SVM	13.475	0.48	0.59	162.92	0.57	0.832

MODEL	Stiffness			Strength		
	RMSE (GPa)	R- Squared	Training Time(s)	RMSE (MPa)	R- Squared	Training Time (s)
Rational quadratic	11.064	0.65	8.61	146.72	0.65	1.377
Gaussian						
Matern 5/2 GPR	10.905	0.66	1.55	142.87	0.67	1.285
Exponential GPR	11.092	0.65	1.56	140.21	0.68	1.162
Narrow Neural network	46.228	-5.12	6.81	1014.80	-15.58	5.042
Medium Neural network	30.128	-1.60	3.60	445.59	-2.20	3.990
Wide Neural Network	30.584	-1.68	4.34	481.14	-2.73	3.380
Trilayered Neural network	18.622	0.01	5.09	302.25	-0.47	4.130
Micromechanics	6.810	0.74	N.A	70.65	0.72	N.A

Figure 32 and Figure 33 show the plots of the winning model, above the perfect prediction line the model overestimates the property, and below it underestimates. Again, the better performance, in both stiffness and strength, of the micromechanical model is evident from the low scattering in comparison with the best data driven model (in terms of higher R-squared).

Figure 32

Predicted vs. true response in stiffness (GPa) for the: a) best data-driven and, b) micromechanical models

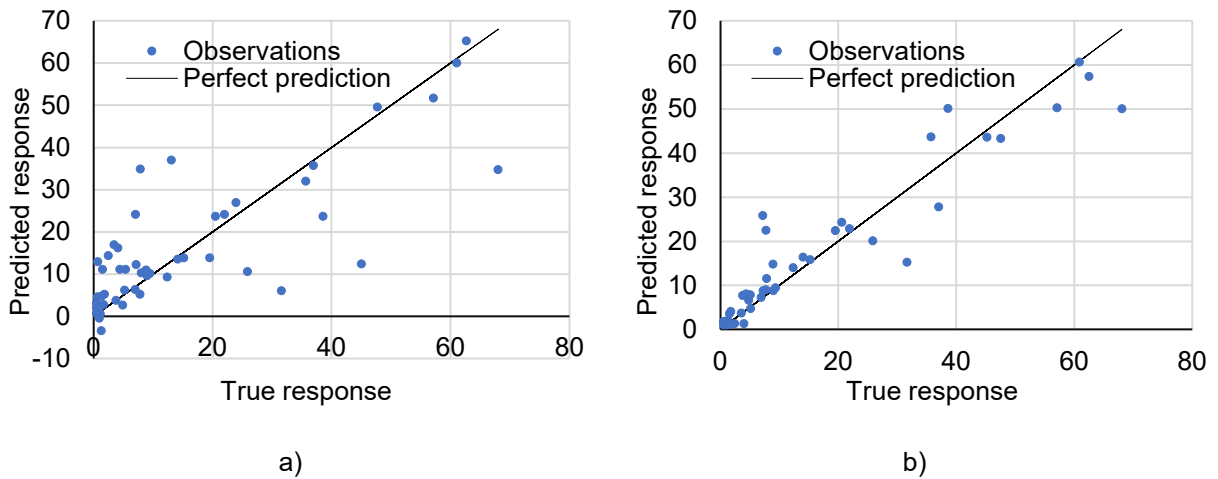
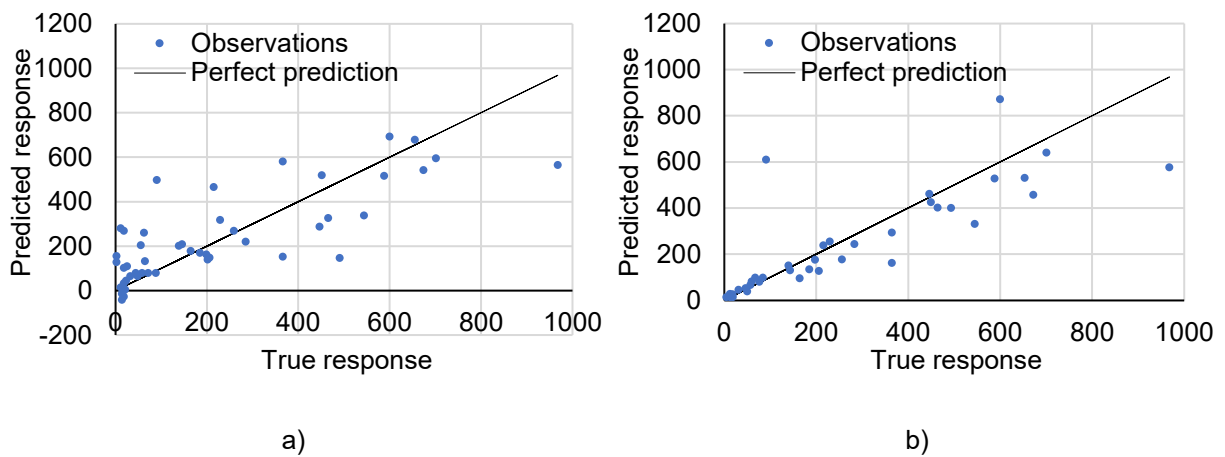


Figure 33

Predicted vs. true response in strength (MPa) for the: a) best data-driven and, b) micromechanical models



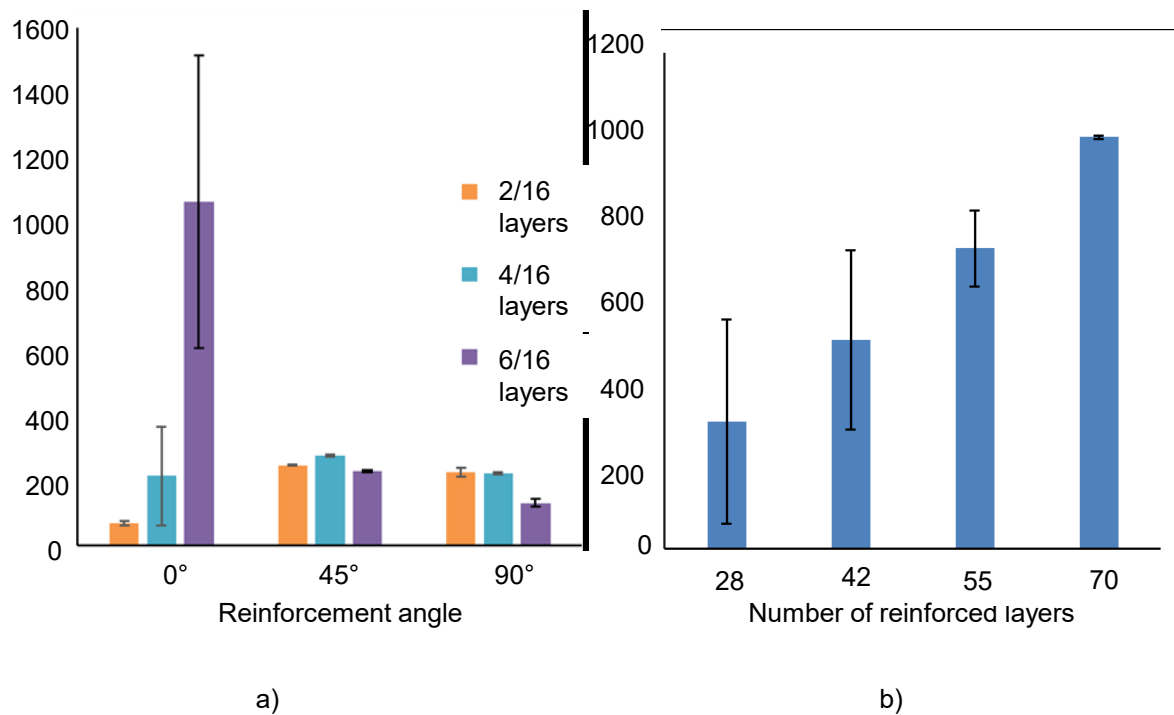
Another important parameter of FRAM are energies dissipated per unit area G_C , which could be calculated from the stress-strain response by performing integration of the curve, as equation (73) shows:

$$G_C = \int_0^{u_e^f} \sigma_e du_e \quad (73)$$

Where σ_e is the equivalent stress, that in the case of uniaxial stress state, it is the actual stress. u_e is the equivalent displacement, for the uniaxial stress state, is equal to the axial displacement. Finally, u_e^f is the ultimate equivalent displacement. Figure 34 relates the total dissipated energy in print orientation and fiber content.

Figure 34

Absorbed energy per area in (MPa.mm) for: a) flat printed, b) on-edge printed



The on-edge printed samples presents a proportional tendency to increase the absorbed energy per area with respect to the number or reinforced layers, also the scatter is lower based on the error bars, reader must recall that the total amount of samples was 4 per data point. On the other hand, in the flat printed samples, this proportional increased tendency was observed only for the 0°-degree coupons but presenting higher scattering of the values. In the 45 degrees and 90 degrees downwards tendency is present, this could be explained by the reduction in maximum elongation while maintain a close stiffness, a proper behavior of matrix dominated composite.

5.4 Fractographic and Microstructural Analysis

Fractography is the study of fracture surfaces and is a helpful tool in the failure analysis of materials. Fractography and failure analysis can provide important clues about the causes of failure and the consequent sequence of events. Scanning electron microscope (SEM) provides high resolution, good depth of field and the ease of specimen preparation for characterizing fracture surfaces and microstructure.

5.4.1 Generalities of Fractographic Analysis

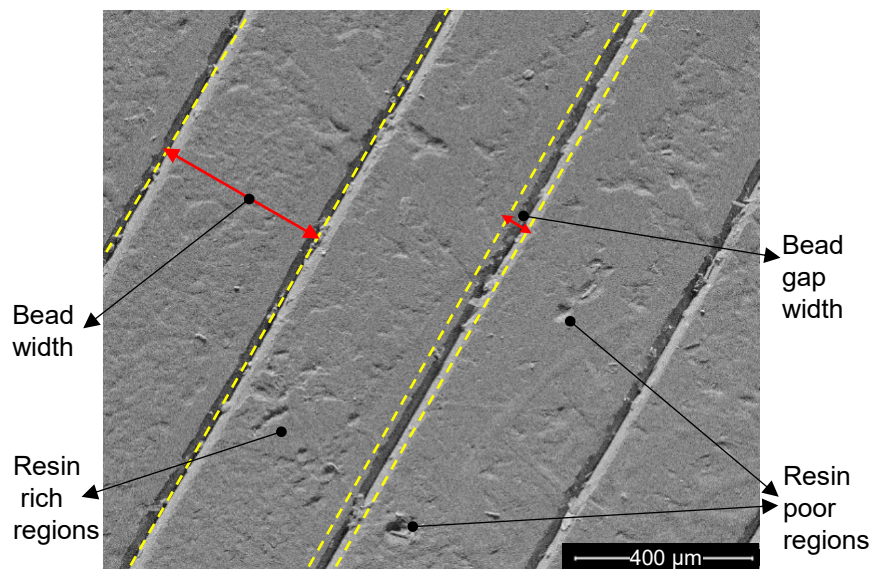
After the failure had occurred, samples of Table 10 were visually inspected, photographed, dissected, and then prepared for SEM analysis. The dissection is the cutting of the specimens into smaller pieces able to be scanned. It is performed with a fast-cutting tool. In this case, a Dremel 3000 with a cutting disk was used. Sometimes a metallographic encapsulation was needed to polish the observation surface, and the grinding process was done in an automatic grinder, starting with 200 grit paper up to 2500 grit paper. Then, a conductive layer was applied to the surface for better visualization. In this case, it was applied a gold layer in a sputtering method. Although two SEM

were used due to their availability, most of the fractography was performed in the VEGA TESCAN SEM, but a QUANTA FEG 650 SEM was also used.

In (Greenhalgh, 2009) the author presents a comprehensive study in failure analysis and fractography of PMC, a complete explanation of the stress state and their link with the microstructure is out of the scope of this thesis, and the reader is encouraged to visit the reference in this subject. The following images correspond to AM composite manufacture from carbon fiber and Nylon White, with reinforcement at 90° fiber angle. Figure 35 depicts the surface finish.

Figure 35

Surface of a FRAM part by SEM



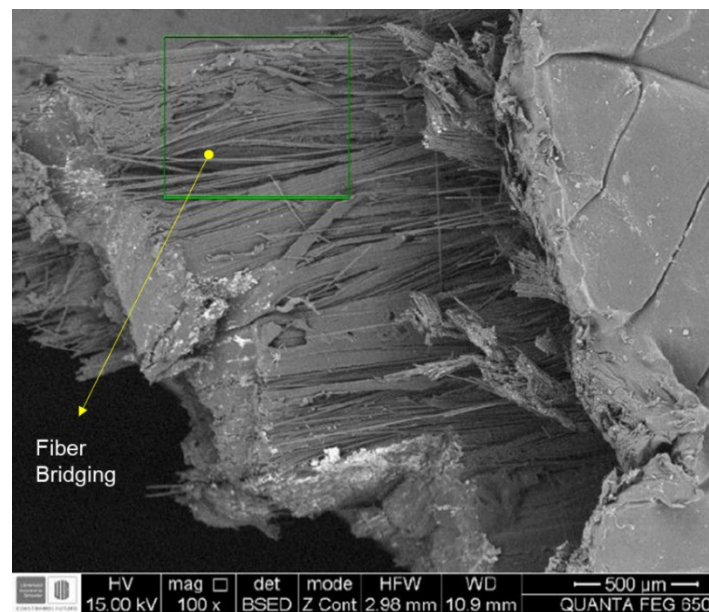
In this image, the surface of the AM part is identifiable, particularly the size of the bead, some superficial imperfections, and the interbead gaps. The bead size is around 400 micrometers, while the gap could reach dimensions of 50 micrometers. On average, some poor resin regions

being 50 micrometers in their longest dimension was observed. On the other hand, resin-rich regions are also larger in extension than resin-poor regions.

Figure 36 and Figure 37 show the fracture surface of the sample evaluated in pure tension. In Figure 36, the slip planes of 90° samples are identifiable. It is to note the relatively flat surface generated and the serrated profile. The crack path sequencing can be deduced the fiber region fails first, then the thermoplastic surface layers.

Figure 36

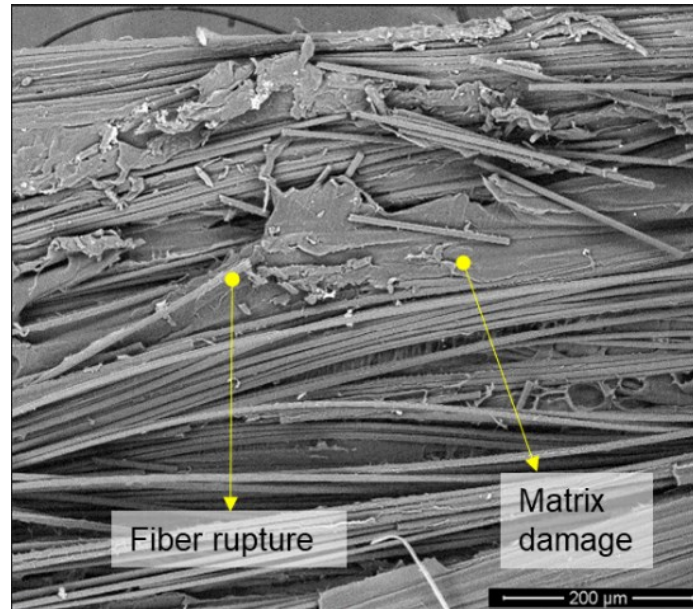
Fractographic surface of 90° UD carbon fiber reinforced nylon white



In Figure 37, a close-up region where failure features such as fiber rupture, fiber bridging, and extensive matrix damage are present.

Figure 37

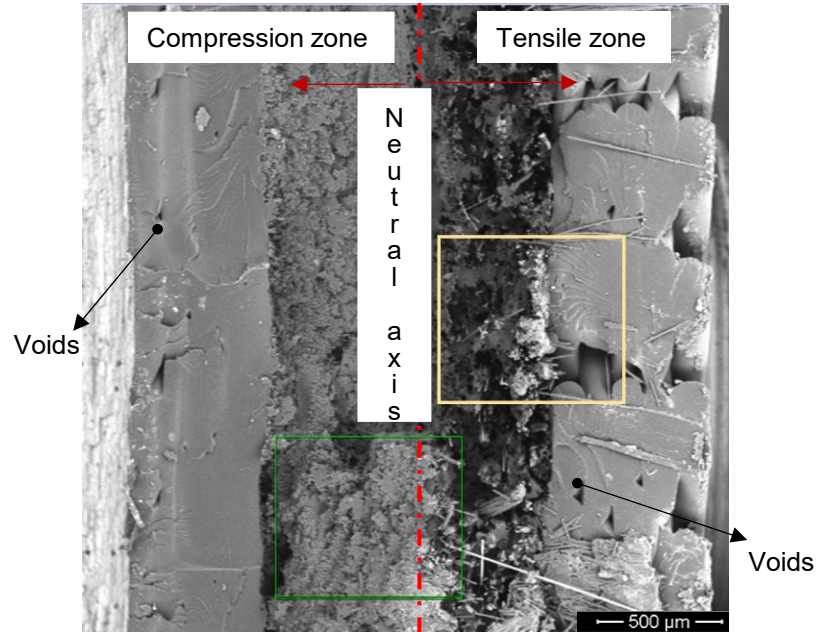
400X zoom to a 90° UD carbon fiber reinforced nylon white



When tested in compression, one must ensure that the specimen will not buckle, causing misinterpretations of the test. For example, the following images correspond to an AM composite manufactured from carbon fiber and Nylon White that failed due to compression buckling. In Figure 38, a distinction between the left zone and the right zone is shown. The left one corresponds to the compression region, while the right to the tensile region. Note that compression failure has flatter regions than tensile failure.

Figure 38

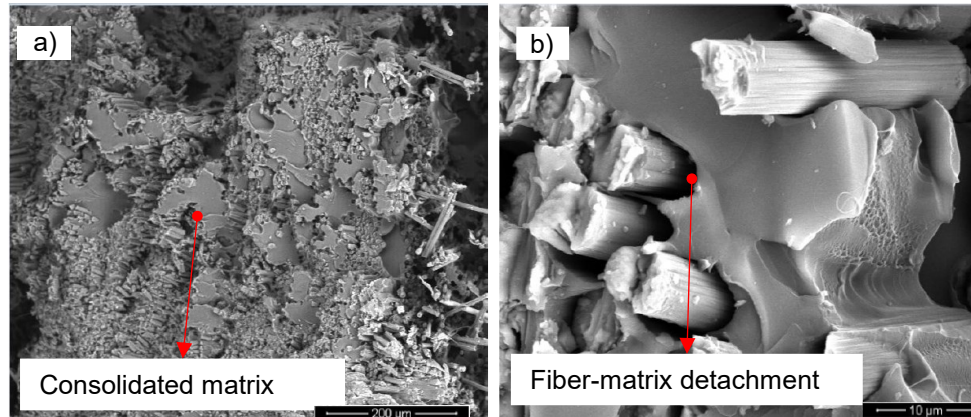
Buckling failure specimen at low magnification, the rectangles show the magnification zones



As the thermoplastic matrix is generally ductile, it is noted in Figure 39, a consolidation of some matrix regions, showing flat. However, a separation between fibers and matrix phase is detectable, consistent with a fiber micro-buckling failure mechanism.

Figure 39

Compression failure zone of the buckle specimen: a) in low magnification, b) high magnification.



In Figure 39b, and Figure 41, the microscopic tension features are presented. In Figure 40, lines in the matrix at the right zone, called river lines are presented. Figure 41 shows the extensive fiber damage suffered.

Figure 40

Tension failure zone of buckled specimen showing fiber and matrix damage

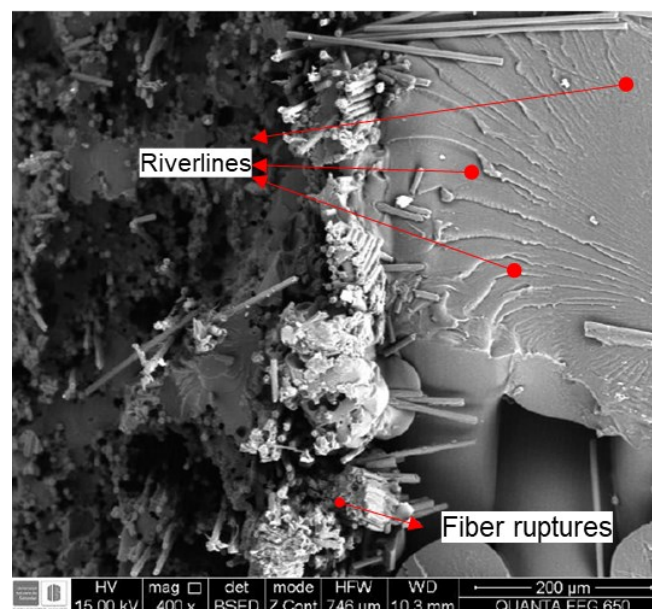


Figure 41

High magnification tension failure zone showing microscopic fiber features

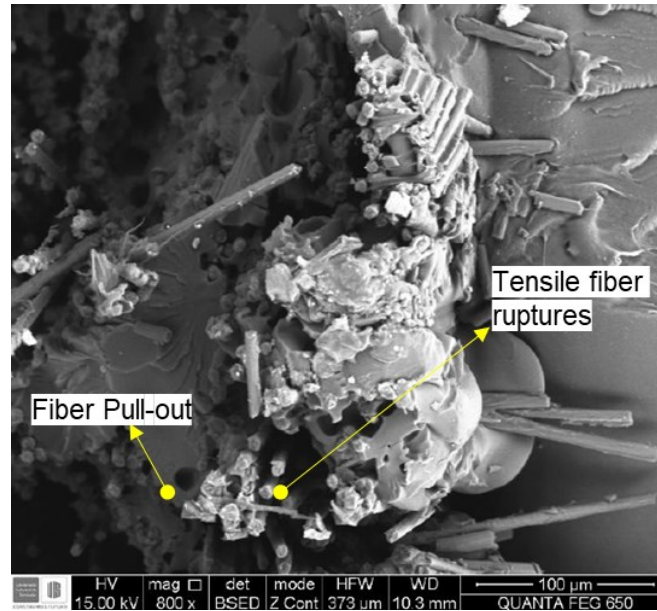
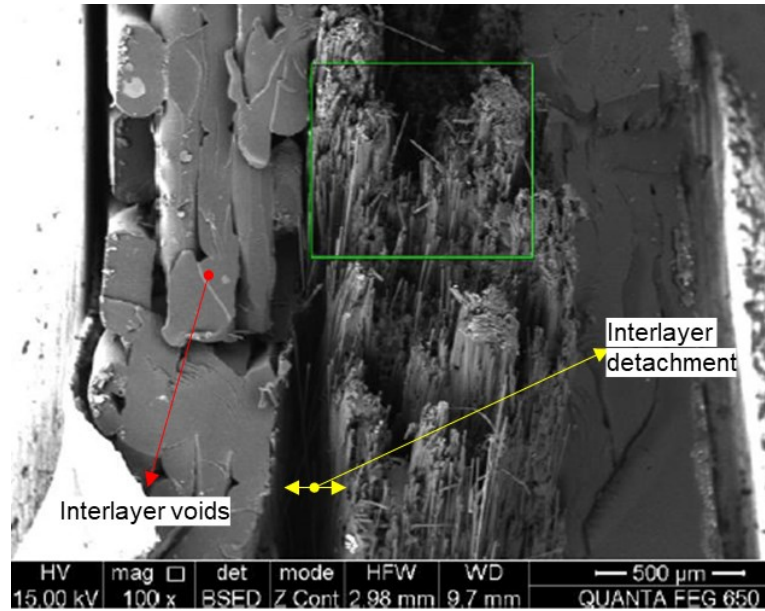


Figure 42 to Figure 44 correspond to a FRAM manufactured from carbon fiber and Nylon White, with 0° layers reinforcements. The sample was evaluated in pure tension originating a brittle fracture.

Figure 42

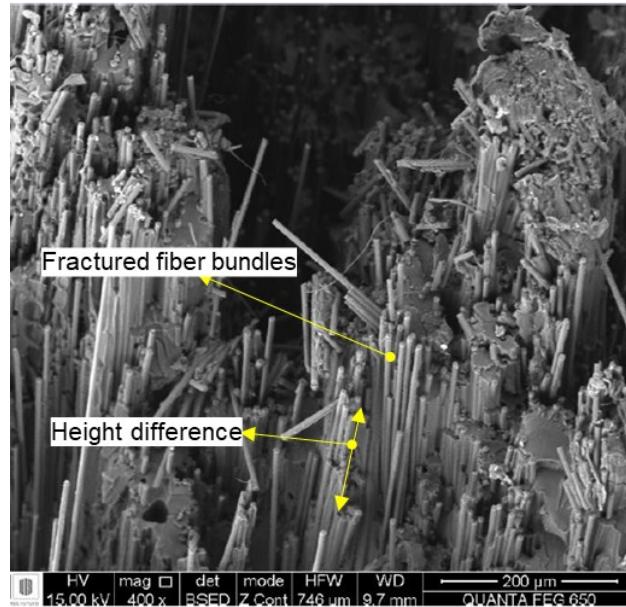
Pure tension failure fractographic surface of a 0° UD carbon FRAM



In Figure 43, different height planes of the fibers, typical of a high-energy fracture in the longitudinal direction are shown.

Figure 43

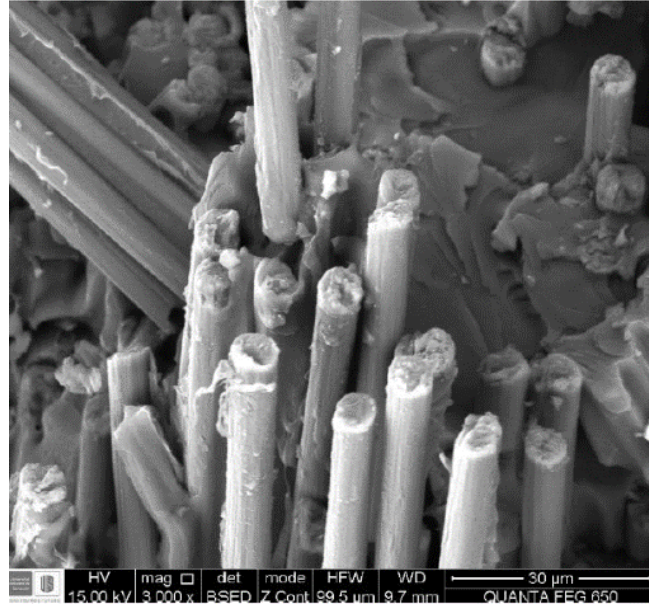
400X magnification of a 0° UD carbon FRAM



While in Figure 44, it is notable that the fiber ends, and surface finishing show traces of matrix attach in the fibers, indicating a good fiber-matrix interphase strength adhesion.

Figure 44

Fracture surface fiber close up magnification (3000X) of 0° carbon UD FRAM



5.4.2 Short Fiber Composite Fractography

Short fibers or chopped fibers are usually fewer than 30 times the diameter of the fiber. However, there is no consensus on the maximum length of short fiber. In addition, short fibers are generally dispersed randomly at the matrix. Thus, their mechanical behavior tends to be isotropic. The Figure 45 depicts a failure surface of an Onyx specimen, and the layer divisions in the microstructures are present, but they are not as evident as continuous FRAM.

Figure 45

SEM of a failed short carbon fiber reinforced AM composite (Onyx)

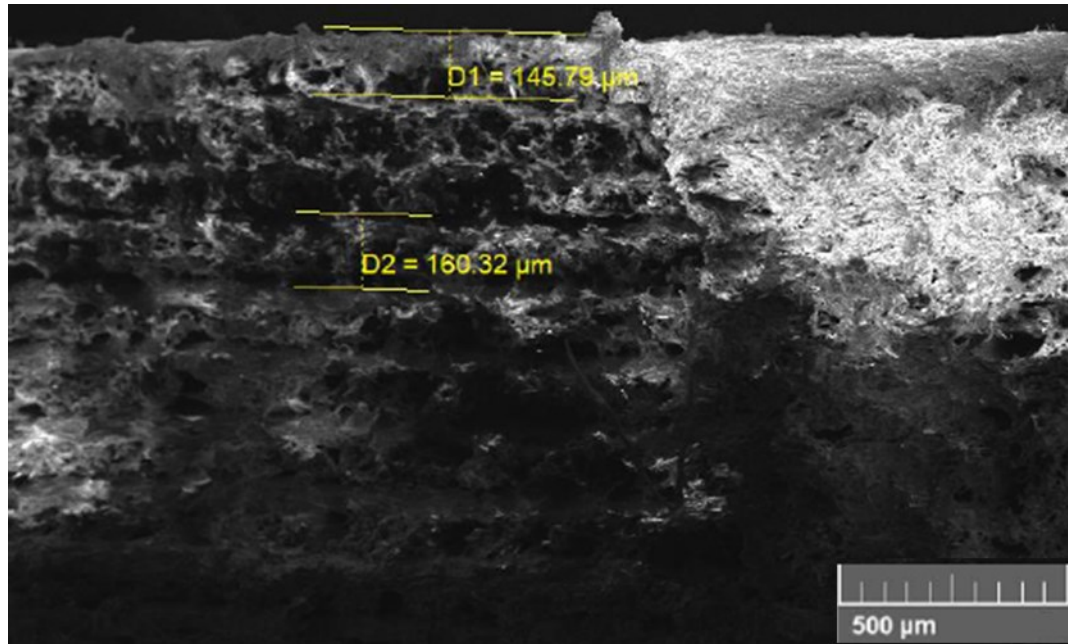
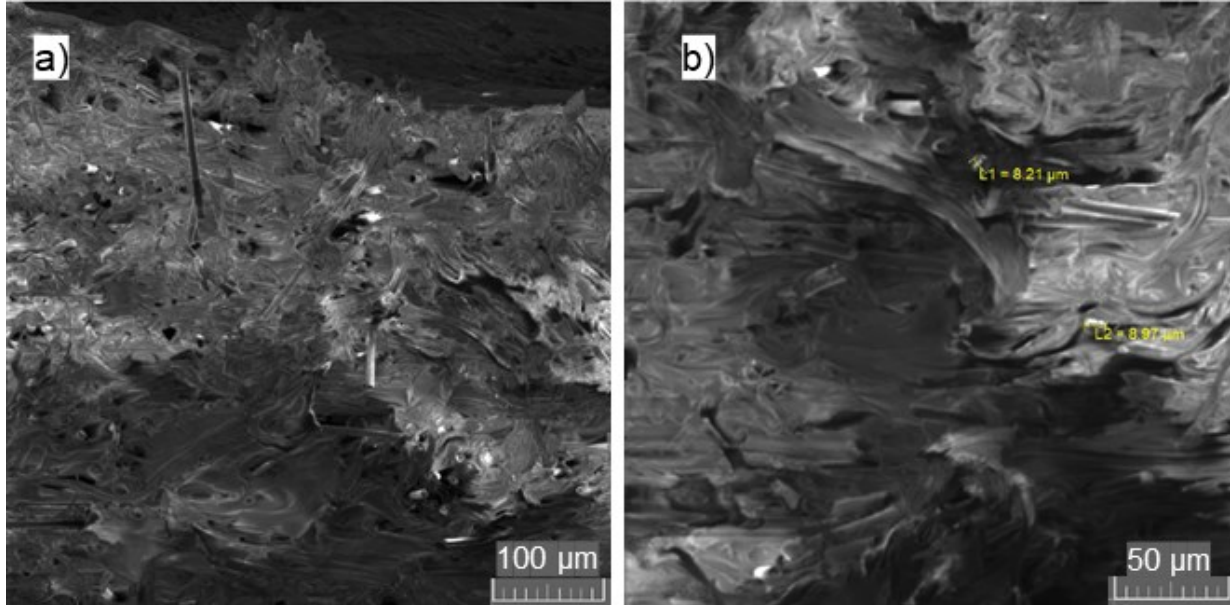


Figure 46 shows plastic microflow due to the increasing stress levels. Also, it has features such as scarps, and these characteristics are consistent with a ductile matrix behavior typical of thermoplastics. Fibers are dispersed even in the whole structure and randomly oriented.

Figure 46

SEM surface of Onyx: a) 382X, b) 793X magnification



5.4.3 Fractographical Analysis and Process Parameters Influence

A macroscopic appearance of failed specimens dependent on processing parameters such as volumetric fiber content and print direction was observed. Failure topologies could be resumed in three categories for the flat specimens, as shown in Figure 47. A zero-degree tension failure is represented in the first type depicted in a). All the zero degrees coupons failed translaminal, meaning a breakage of the fibers and splitting of the specimen into two parts. The fibers in different heights are consistent with a high energy fracture.

Figure 47

Schematic of the failure topologies of AM composites: a) 0°, b) 45°, c) 90° fiber alignment

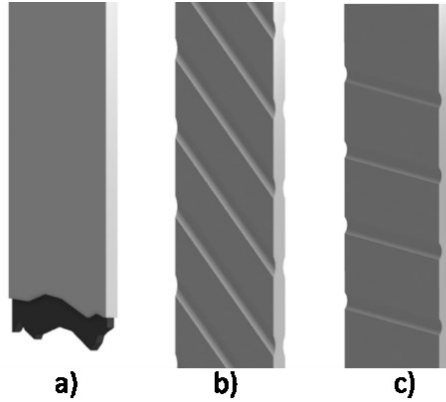


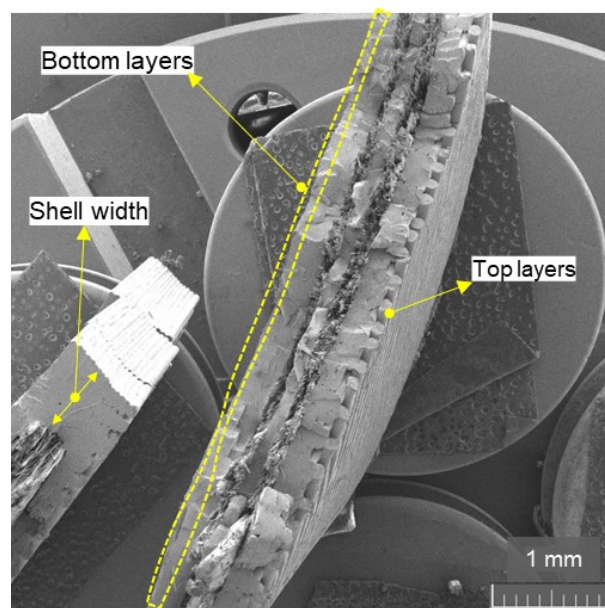
Figure 47b) and Figure 47c) are the second and third failure types for 45° and 90° reinforcement angles. The specimens did not break, and they experienced high levels of deformation that reached the end of the displacement. The failure sequence may be that the failure starts in an Intralaminar manner (Through the thickness in which only matrix and fiber/matrix interface are broken) and then Interlaminar. The reinforced region yields in multiple lengths and progresses through the nylon, causing plastic deformation with high strains, thus forming “shear bands.”

A mixture of the two modes for the on-edge printing specimens were present. In specimens with low reinforcement content, the samples failed mainly by large deformation in the nylon zone and, consequently, the intralaminar failure of the reinforced region. On the other side of the spectrum, the higher reinforcement content specimen failed by the breakage of the specimen into two pieces, which was caused by the translaminar failure of the reinforced region and the inability of the nylon to sustain the applied displacement.

Fractured specimens are dissected near the failure surface using slow cutting rates. Cross-sectional views are from failed specimens ground in increasing grit paper numbers, then stored in a desiccator. It is interesting to note the microstructural mismatch between the nylon region present in the bottom of the sample and the top surface for the flat specimens. This mismatch is due to a lack of compaction phase in the last layers of the AM process, thus, creating a rougher surface in which the raster print is more visible, Figure 48.

Figure 48

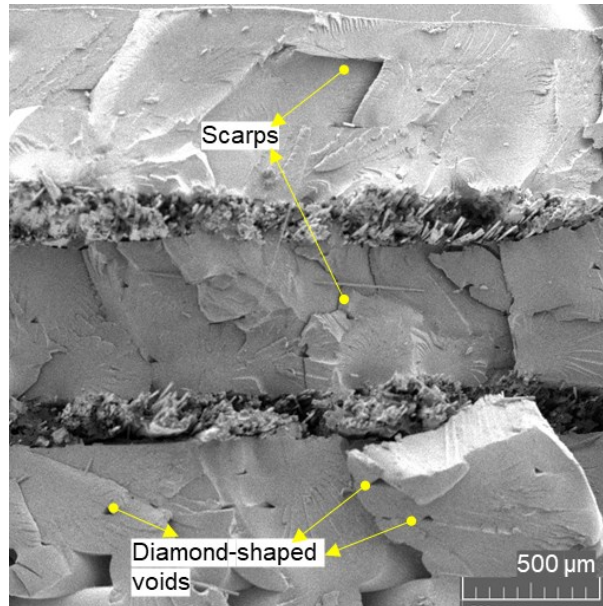
Wide view of a flat printed 0° FRAM 2-16 layers



Zero degrees carbon-reinforced nylon white tends to fail abruptly. In Figure 49, fiber rupture is evident in the macroscopic appearance of a tensile specimen.

Figure 49

Flat printed 0° FRAM 4-16 layers reinforcements

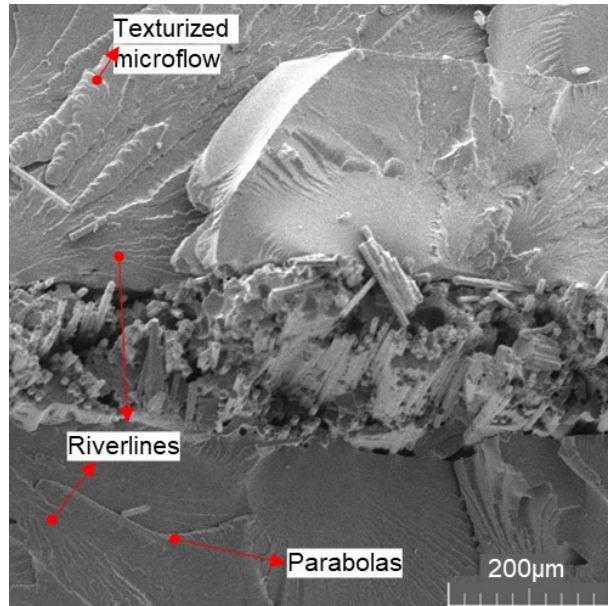


It is observable the interbead porosities created due to the contraction of the melting phase and the subsequent solidification of the adjacent layers. As indicated in (Rodríguez et al., 2003) the interbead porosities are diamond-shaped.

Failure initiates at a location of minor defects. The surface is relatively flat at the points close to it; And all the fibers in this zone fractured in the same plane, also parabolae in the nylon, and features that spread out of the possible failure zone are present. For the microscopic appearance in Figure 50, it is distinguish the matrix-related features such as parabolae, riverlines, and microflow.

Figure 50

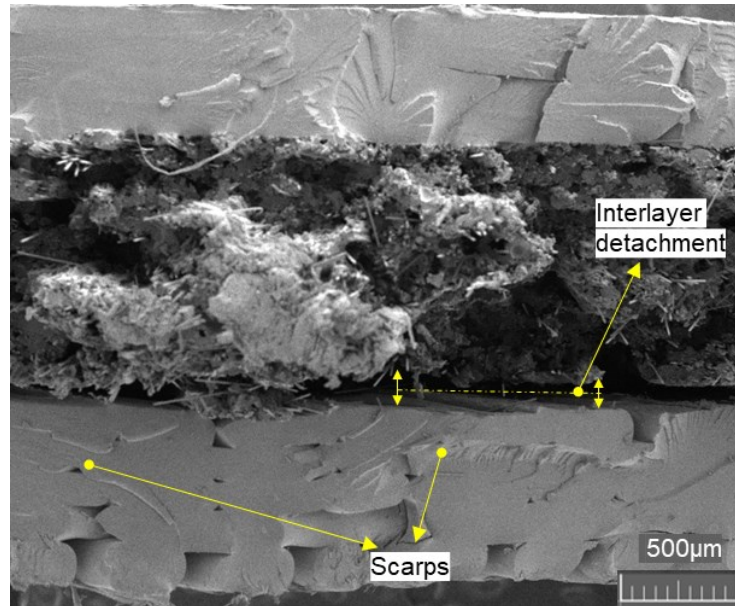
Flat printed 0° FRAM with four reinforcement layers



Diamond-shaped porosities can serve as stress concentrators in the failure process. Figure 51 distinguishes the scarps and textures close to them. Also, as this specimen has more fiber layers that resist the load, a detachment between the fiber region and the nylon is evident at the bottom of the image.

Figure 51

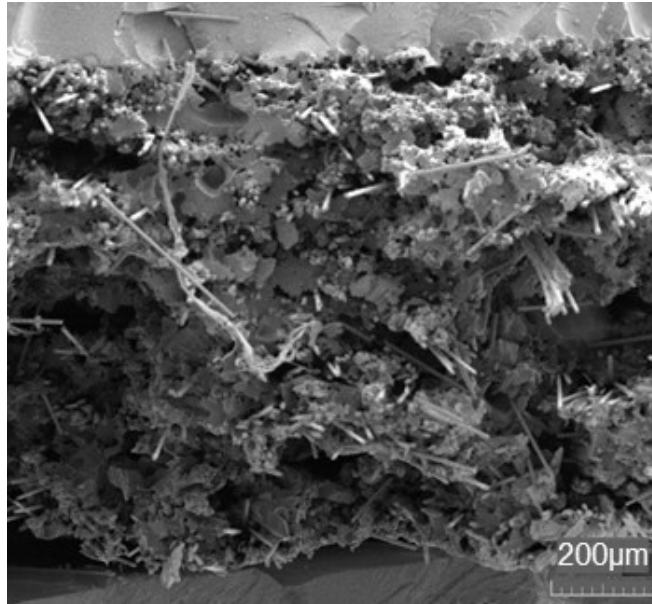
Flat printed 0° FRAM 6-16 showing detachment of the fiber region



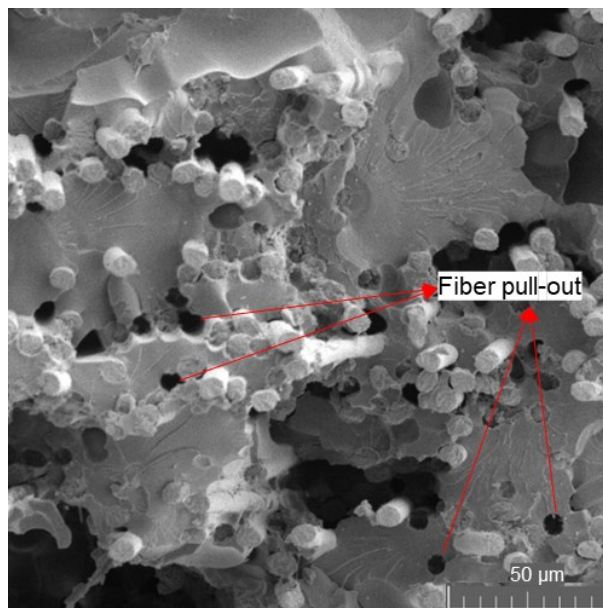
A closer look at tensile breakage in high reinforcement specimen, Figure 52, reveals severe fiber fracture separated in different heights bundles consistent with high energy and sudden failure. Thermoplastic matrices often exhibit increased fiber pullout, leading to fewer bundles of failed fibers and "directly attributable fiber failure" (DAFFS).

Figure 52

Tensile breakage fractography in a flat printed 0° FRAM 6-16

**Figure 53**

Flat printed 0° FRAM 6-16 showing fiber pull-out



It is observable in Figure 53 the fiber prints on the opposite failure side when the fiber pulls out. The fiber pull-out failure mechanism is indicative that the interface between the fiber and the matrix has failed. Figure 54 depicts a flat printed 45° fiber angle tensile specimen, has stated before, the specimen did not break, thus requiring transversal cut dissection.

For the microscopic features of unidirectional tension, the fiber ends exhibit radial features that fan out from a local source of failure on the fiber. If fibers are in contact, one can predict the sequence failure in a process called DAFFS. An additional feature of tension failure is the degree of fiber brooming, which is the degree of ply splitting developed before fiber fracture. This process has a strong influence on fracture morphology.

Figure 54

Flat printed FRAM with 45° and two layers of reinforcement

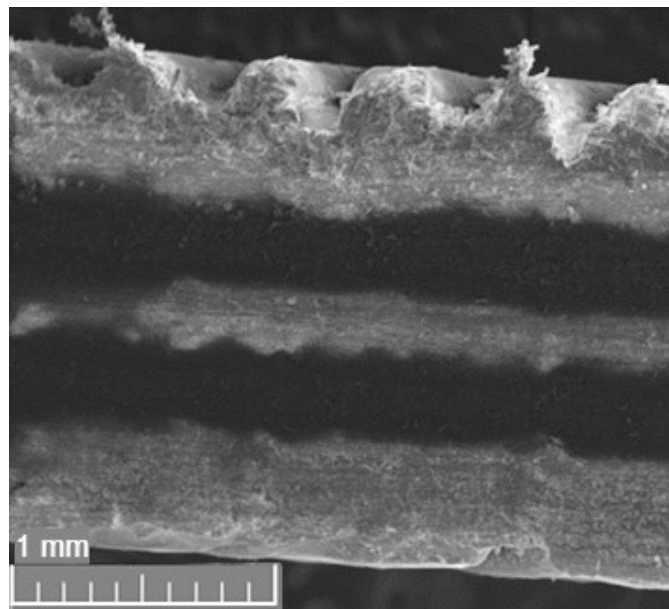
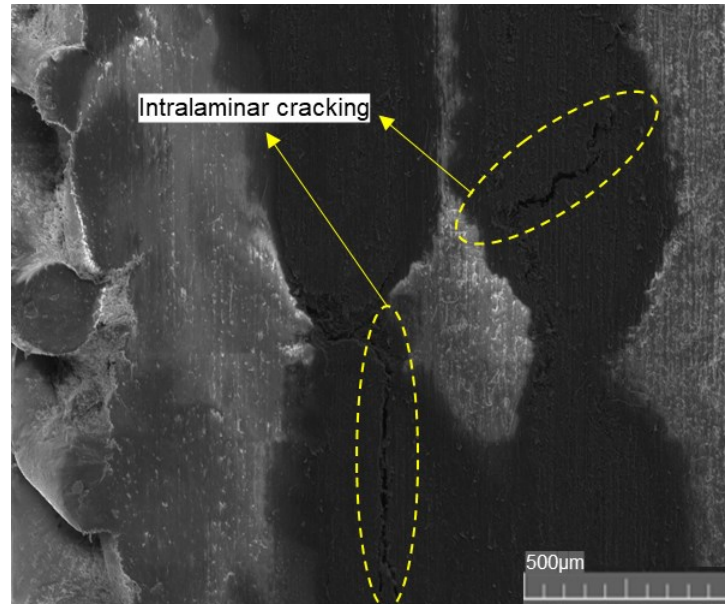


Figure 55

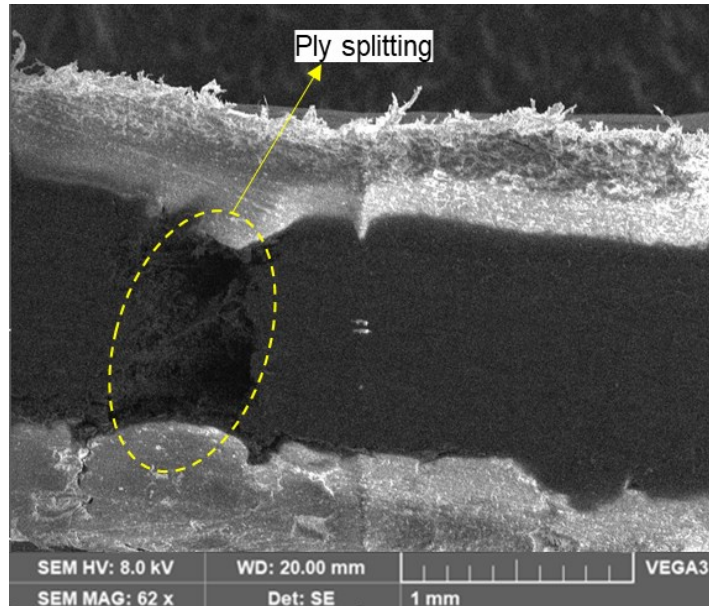
Matrix cracking in a flat printed 45° carbon FRAM (4 carbon layers)



Intralaminar failure is the most common failure in these specimens, and Figure 55 shows cracks in the reinforced region. The local stress field, probably due to differences in local stiffness, influences the path of the propagating crack, causing it to deviate.

Figure 56

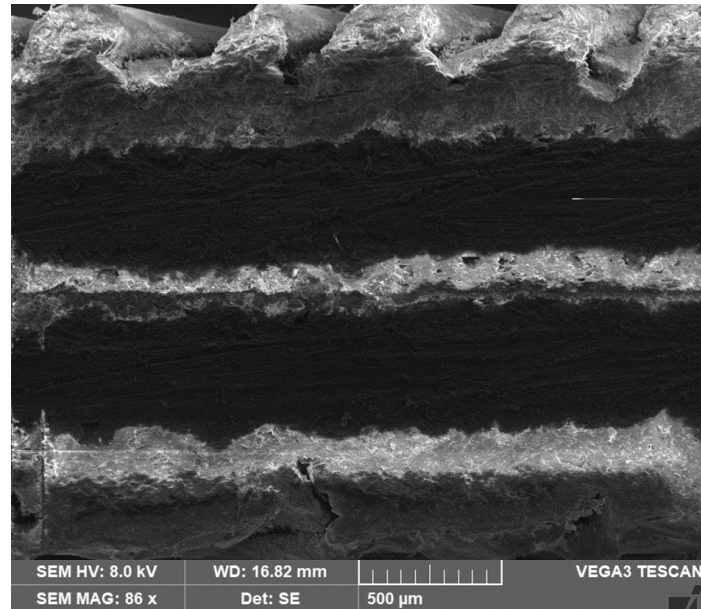
Ply splitting in a flat printed 45° carbon FRAM



The specimen in Figure 56 may have failed under intralaminar fracture followed by interlaminar as the detachment of the reinforced plies and the nylon indicates. Ply splitting is one of the most common failure modes in laminated composites. This fracture mode develops from tensile forces transverse to the fibers or shear forces parallel to the fibers.

Figure 57

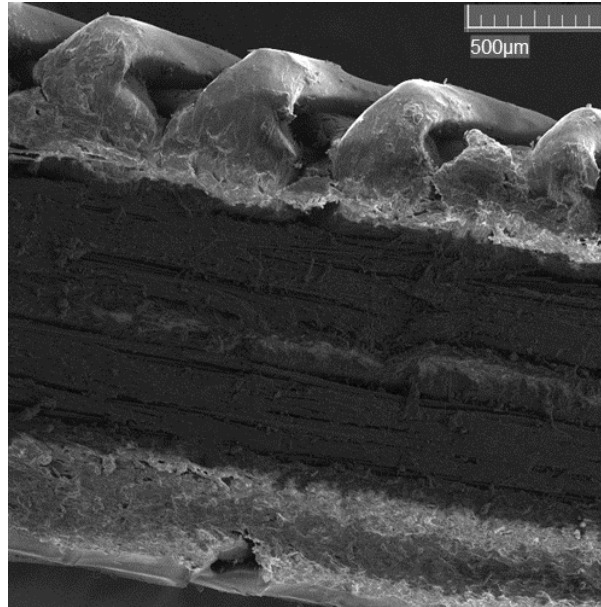
Macroscopic view of a flat printed FRAM with 2 layers reinforcement at 90°



In the 90° samples, evidence of more matrix cracking than in the 45° reinforced specimens is present, and this is because the fibers sustain the least amount of stress compared to other angles. Thus, demanding more for the matrix. Figure 57 shows a low volume reinforced 90° macroscopic appearance. Figure 58 depicts the extensive crack growth in a 90° medium reinforced sample consistent with an intralaminar failure, and also, crazes in the nylon bottom part are present.

Figure 58

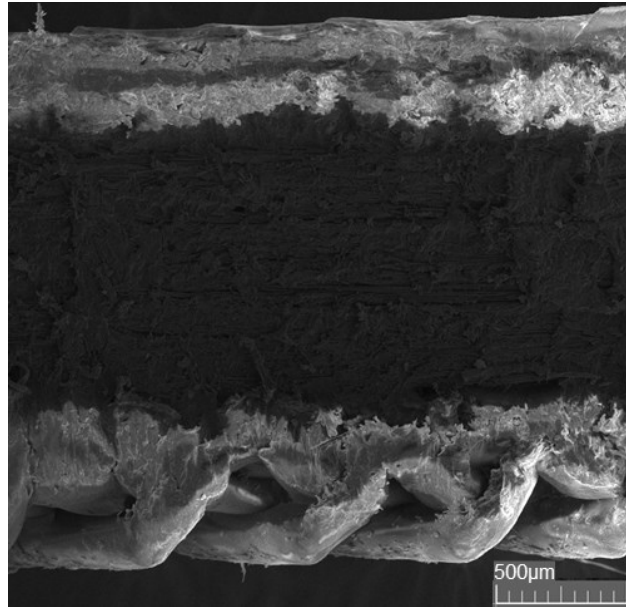
Extensive crack growth in a 90° reinforcement FRAM



Even at high reinforcement volume, Figure 59 shows some signs as extensive as Figure 58. This interlaminar failure is because matrix cracking is a prevalent failure topology in those parts.

Figure 59

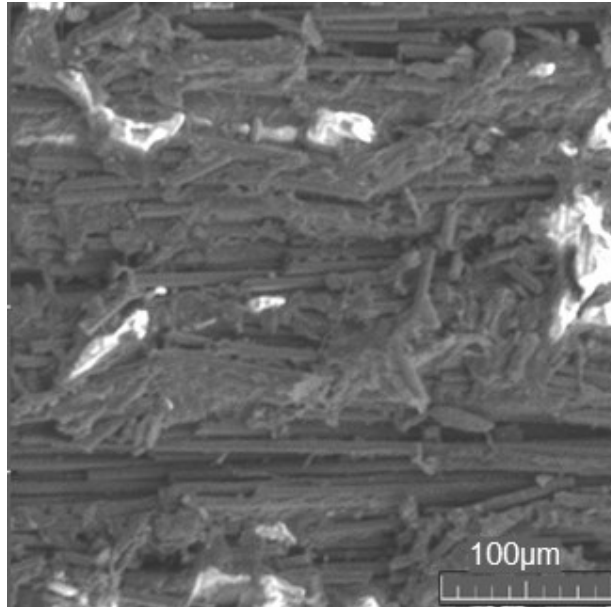
Fractography of a six-layered flat printed 90° reinforced FRAM



Due to its high toughness when compared with other polymeric matrix systems, nylon present a rough surface in which the fracture is principally absorbed through void coalescence (Greenhalgh, 2009; Tasch et al., 2019), such that large-scale ductile drawn and fibrillation occurs, see Figure 60.

Figure 60

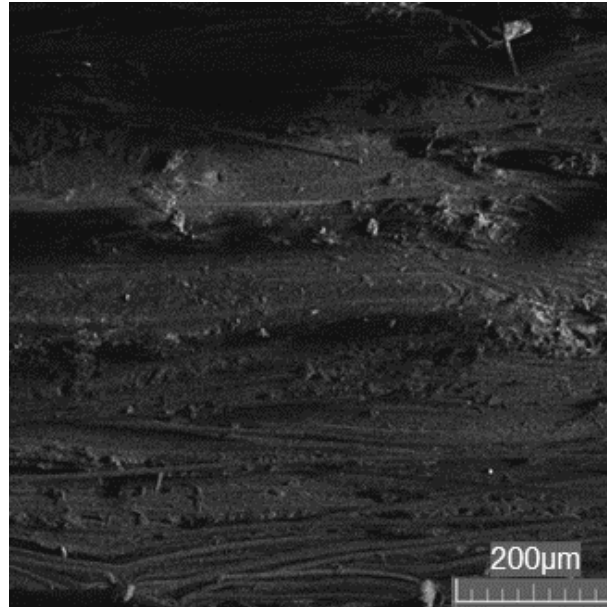
Fractography of a six-layered flat printed 90° reinforced FRAM at 565X



In addition, at slow speeds such as those presented in this test, the matrix has time for plastic deformation, and fibrillation of the matrix develops. Thermoplastic composite preparation is a delicate issue despite the care taken because abrasive particles could cause torn and rough surfaces, as shown in Figure 61. It also shows in-plane fiber misalignment and low severity waviness.

Figure 61

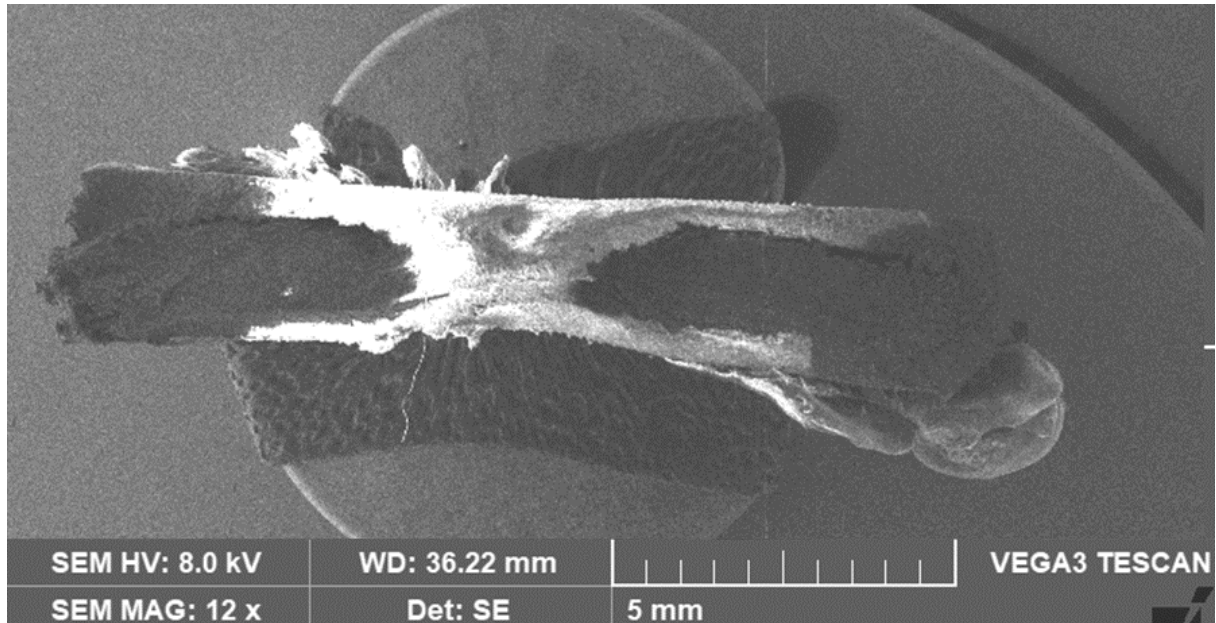
Fractography of an on-edge printed reinforced FRAM with 55 reinforced layers



The on-edge printing specimens show extensive damage in the nylon region, which can be concluded from the fibrillations in Figure 62. Other fractographic features such as scarps and crazes are visible in the nylon region in Figure 63 and Figure 64. Features like cusps and scarps to be visible.

Figure 62

Wide view of a 70 layer on-edge printed reinforced FRAM

**Figure 63**

Fractography of a 70 layer on-edge printed reinforced FRAM, zoom on reinforcement region

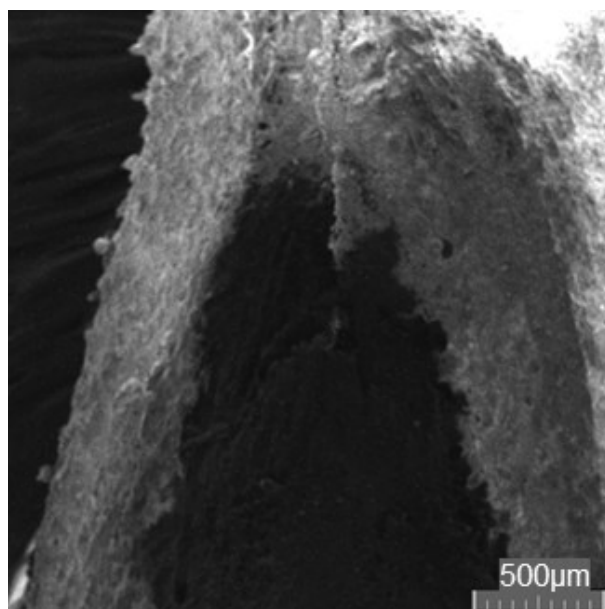
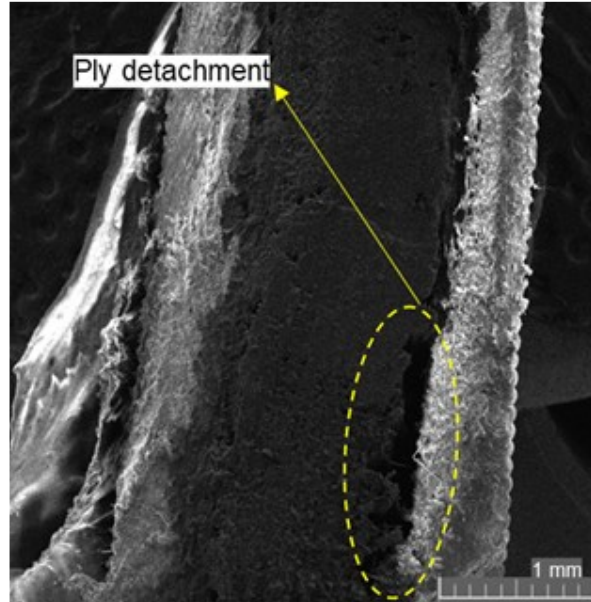


Figure 64

Ply detachment on a 70 layer on-edge printed reinforced FRAM



5.5 Conclusions of the effects of process parameters

Considerable strength variations are observed in this work, and there are many reasons for this significant difference. First, a lack of consistent definition of strength is the maximum or linear elastic stress, also known as yield. Second, intrinsic variability and the effect of the manufacturing process. Third, the materials could have microporous differences in the reinforcing fibers. In addition, poor test methods and variations in carrying them out, although this effect was minimized with a careful manipulation of the specimens, the author can not ensure the same conditions in other experimental work. Such conditions are the use and type of grip tabs.

The results are independent of the stack-up order (for longitudinal testing such as tension and compression). However, a flexural model will give un-accurate results. One could then express the individual compliance matrices of the laminate.

The generalization capabilities of machine learning algorithms are pretty good, giving reasonable estimates of the longitudinal and transverse modulus and strength of AM composites. However, the lack of an estimate of the other direction's properties makes its generalization relatively poor. A possible way to overcome this issue would be to perform a data augmentation based on micromechanical formulations, preferably more accurate ones. Thus, the two models will cooperate instead of competing.

In fact, what is present is a composite sandwich in which forces are applied to a laminate. This work compares a basic model in which the mesoscale is not entirely depicted and instead gives quick estimates of the mechanical properties.

The model assumes a perfect bonding between layers, which is difficult to obtain in AM components. In addition, defects such as bed level issues, thermal management of the extruder, warping of the piece, and hygroscopic characteristics of the nylon can affect the interlayer bonding.

The effect of the volumetric fiber fraction and printing direction on the mechanical response and failure mechanisms was assessed in this article. Different models were tested to evaluate their prediction capabilities, and micromechanical models outperform machine learning with an RMSE of 7.66 GPa in stiffness and 70.05 MPa in strength. In addition, it has the advantage of being physics-based. However, the performance of the ML algorithms was not very good in part due to a lack of consistent data, with a widespread range of materials, methods, and machines for the promotion of continuous FRAM. Poor data amount derives from the difficulty in obtaining

data without a standard for reporting the printing process and parameters. For instance, most of the assumed flat printing direction was not reported in the article. Also, volumetric fiber fraction is not always reported. Among the ANNs, the trilayered NN performs the best. However, more data is needed in testing to give an absolute answer.

Fractography of AM composites shows the macroscopic features such as interlaminar, intralaminar and translaminar failures, having the same nature of failure mechanisms as traditional manufactured composites. Also, microscopic features of both matrix and fiber were observed, depending on the load type, fiber failure could present torn surface, indicative of a compressive fiber micro buckling or a flat surface most likely due to sudden tensile rupture. Matrix microscopic features such as scarps, riverlines, and microflow. Microstructural differences among the specimens with different reinforcement content and printing orientation were observed, the macroscopic appearance of the flat and on-edge 3D printed evidence lower amount of intralaminar cracking, while the detachment of the plies was a common failure mechanism.

6. Progressive Damage Model, Validation, and Verification

FRAM composite displays better mechanical properties than AM polymers and better manufacturability than traditional composite manufacturing. However, their mechanical properties, damage behavior, and failure mechanisms are still active research topics because of their recent invention (Díaz-Rodríguez et al., 2021).

The present chapter aims to determine a progressive failure analysis of composite FRAM via a continuum damage mechanics method to assess their prediction capabilities. It relies on a

reduced methodology which allows few tests to determine the damage parameters. This work extends engineers' tools by assessing damage methods, showing progressive damage and their link with damage variables.

This chapter states the validation methodology of the damage model based on the material characterization presented before. The first part introduces the damage models, stating the primary variables, assumptions, and capabilities. Notably, a CDM model based on Matzenmiller work is carried on, first stating the eight model parameters: four energy released per area and four viscous damping coefficients. Second, a general overview of validation and verification methods in FEA is presented, emphasizing experimental validation. Third, the validation of the model is done with an experimental stress analysis using a 2D-DIC, and the details and DIC parameters are presented. Finally, the chapter concludes with the comparison of the FEA model and the experimental results of the validation.

6.1 Damage Models

Polymer matrix composites (PMC) and generally all composites show an anisotropic behavior, complex failure mechanisms, and recyclability problems. Their mechanical behavior is reasonably well understood in the linear elastic region. PMC elastic behavior can be described using an anisotropic elasticity theory or micromechanical theory, which helps characterize the composite properties from its constituents. However, failure mechanisms and prediction are more complex tasks (J. León-Becerra et al., 2021). First, there is not an obvious definition of the strength or failure of a composite. There are two disputable points: the first when the structure fails and the second when the composite suffers irreversible damage. Next, multiple failure mechanisms such as matrix cracking, fiber fracture, matrix crushing, delamination, buckling, and fiber micro buckling can interact in different forms. Finally, there is not a consensus on failure-prediction

theories. There is a wide range of failure criteria: Max stress, max strain, or interactive criteria such as Tsai-Hill, Tsai-Wu, LaRC-03, LaRC-04, Puck and Schurmann, ExPan extended Puck and Schurmann (T. A. Dutra et al., 2020), Hashin, Hoffman, and more. Those failure criteria usually apply to the failure of a single ply, while most manufacturing methods use multiple plies layed up in composite laminates. For those cases, continuum damage mechanics CDM theory helps determine the non-linear behavior after the first ply failure (FPF) occurs. The PMC recyclability is being addressed by developing thermoplastic matrices such as PLA, PEEK, PHA, PHB, or Polyamide, which are easier to recycle. In addition, natural fibers such as Sisal, Flax, and Coir are employed as reinforcement (Azzouz et al., 2019; Montalvo Navarrete et al., 2018).

Current research in traditional manufacturing is well-grounded in the mechanical description and partially on the progressive damage. The composite laminate mechanical behavior starts with a linear elastic region governed by the orthotropic linear elasticity theory. The stresses in the individual plies can be found through classical laminate plate theories CLPT, See equation (43), First-order shear deformation theory (FOSDT), or a second-order one. Once the stress state in an individual ply increases above the ply strength given by the failure criterion, the ply is damaged, the extent and severity of the damage can be accounted for in the microstructure, and the reduced mechanical properties (Guo et al., 2021). After the FPF, the stress-strain response of the whole composite laminate is non-linear, usually with a loss of stiffness due to strain softening. Different approaches can be considered in determining this non-linearity: First, the material property degradation method (MPDM) reduces the stiffness of each engineering constant in a specific factor. While this method is easy to implement, it is not entirely accurate. Second, multi-continuum theories have excellent prediction capabilities, but with high computational costs (Bhattacharyya & Basu, 2020; Zhao et al., 2018). Continuum damage mechanics CDM present a

good fit while maintaining relatively low computational time. Damage progression based on CDM is in numerous works in composite materials. They are used in tanks (Xu et al., 2009), marine, from components made from multiple manufacturing processes, Hand-Layup, Resin Transfer Moulding, and filament winding (Gemi et al., 2009). Damage models are being applied to injection molded composites (Belingardi et al., 2016), waved fibers as in automated fiber placement (Cairns et al., 2016), Concrete; however, few studies use CDM to perform a PDA to AM composites.

MPDM reduces the stiffness of the composite by a set of factors affecting each of the terms. In contrast, CDM formulations degrade the laminate response proportionally according to a damage evolution law. CDM models for composites must satisfy the following steps: first, a definition of the appropriate damage variable, then the failure criterion establishes where the damage would start. Finally, damage evolution law determines how the damage extends and propagates through the structure. CDM damage models for composites are numerous: (Matzenmiller et al., 1995) propose a damage model using three damage variables d_f for fiber, d_m for matrix, and d_s for shear, a Hashin initiation criterion, and an appropriate damage evolution law. Matzenmiller's model is extended due to its implementation in commercial FEA software such as ABAQUS and ANSYS. Barbero et al. (Barbero & Shahbazi, 2017) present a methodology for finding the appropriate material parameters using the least number of tests by minimizing the error in the predictions. More sophisticated CDM models exist, Maimi et al. (Maimi et al., 2007a, 2007b) present an intralaminar progressive damage model supported by a 3D failure criterion in contrast with Matzenmiller (Matzenmiller et al., 1995). In (Vyas & Pinho, 2012), the authors present a novel damage model. CDM models can also account for fatigue behavior and some works compared with machine learning (Zhan & Li, 2021). Interlaminar CDM models are helpful for delamination failures with advances in techniques such as VCCT or CZM.

It is customary that damage models are tested with actual application data such as force, deflection, or deformation. However, another method is to test with an open-hole specimen (Han et al., 2020), a double notched specimen, or a double open-hole for the numerical model validation (Habibi & Laperrière, 2020). Validation data can be captured through acoustic emission, digital image correlation (DIC), or X-Ray. In addition, DIC can be a low-cost to implement method (Miikki et al., 2021; Olufsen et al., 2020).

The mechanical behavior, failure mechanisms, and recyclability of composites depend on the manufacturing method used to fabricate them. AM is an uprising and emergent technology that creates a part formed by layers (Kim et al., 2020). AM of polymer composites is a recent fabrication technology, including discontinuous chopped fibers and continuous reinforcements (Kabir et al., 2020). Discontinuous are cheaper to produce and can be printed in a traditional FFF machine, and they have the advantage of more strength and stiffness than raw polymers but are not as great as continuous fibers. Different authors have studied the failure mechanisms and damage propagation in AM composites (Hou, Tian, Zhang, et al., 2020; Hou, Tian, Zheng, et al., 2020). In (Hou et al., 2018), the authors perform a study of tensile behavior and damage of AM composites. Al-Abadi (al Abadi et al., 2018) perform a CDM analysis of a composite sandwich specimen. Cohesive models can be used in AM to predict the force separation between layers (Liravi et al., 2015). In (Malakhov et al., 2020), the authors perform an MPDM to Variable curve and stiffness continuous FRAM. Van der Werken (van de Werken et al., 2019) characterized the stiffness behavior of AM composites with curved fibers using experimental methods and FE analysis. Zhao uses CDM (Y. Zhang et al., 2021) to account for the degradation of mechanical properties in PLA.

6.1.1 Damage Model Definition

The damage models involve the creation or definition of three stages: first, the definition of the damage variable. Second is the establishment of the damage initiation criteria. Finally, the model is complete by stating the damage evolution law (Sumio, 2012).

In the definition of the damage variable, it is possible to consider three main approaches: first, modeling by the effective area reduction, modeling by the stiffness reduction, and finally, modeling by the void volume fraction.

After the modeling approach has been stated, the grade or dimensionality of the variable should be selected. For example, a scalar damage variable could measure isotropic damage, and it is fast and straightforward to compute but lacks a proper directional damage description. On the other hand, second-order tensors commonly describe orthotropic damage. In PMC materials, the damage is directional, thus, suitable for measuring stiffness reduction.

Damage is caused by stresses, displacements, or loads of different nature. There are models for ductile damage, brittle, low and high cycle fatigue, and spall damage present in impacts. On the other side, environmental, chemical, or thermal degradation weakens the composite, worsening the performance. It can be caused by humidity, temperature, UV Rays, solvents, radiation, and other phenomena. The scope of this work is limited to monotonic mechanical loads, thus neglecting all degradation and fatigue or impact damage.

Knowing the damage activation function and initiation criteria is the next stage in defining a progressive damage model. A suitable damage activation function limits the elastic zone from the damage zone. The elastic zone is where new damage does not occur, and damage growth is absent. Damage threshold can be obtained from the failure criteria by replacing the real stress with the effective stress.

Finally, the damage evolution rule is the last step in defining a damage model. Damage can only grow in a thermodynamically compatible way. The derivation of the framework is not presented here but can be consulted (Kachanov, 1986; Sumio, 2012). The constitutive tangent equation can be obtained by differentiation by the time of $[\sigma] = [C]:[\varepsilon]$, which yields the equation (74) and equation (75)

$$[\dot{\sigma}] = [C]:[\dot{\varepsilon}] + [\dot{C}]:[\varepsilon] \quad (74)$$

$$[\dot{C}]:[\varepsilon] = \frac{\partial[C]}{\partial[D]}: [\dot{D}]:[\varepsilon] \quad (75)$$

In which $[D]$ is the damage matrix. Therefore, with some arrangements and noting that ε is an independent state variable ($\delta[\varepsilon]/\delta[D] = 0$), then expression can be arranged as in equation (76)

$$[\dot{\sigma}] = [C^{ed}]:[\dot{\varepsilon}] \quad (76)$$

Thus, the damage can be obtained, and the constitutive tensor is expressed as equation (77)

$$[C^{ed}] = \begin{cases} [C] & \text{if } [\dot{D}] \leq 0 \\ [C] + \frac{\partial[\sigma]}{\partial[D]}: [L^d]: \frac{\partial f}{\partial Y} & \text{if } [\dot{D}] \geq 0 \end{cases} \quad (77)$$

6.1.2 Simple Instant Material Stiffness Reduction

The simple instant material stiffness reduction also called the material property degradation method, is probably the simplest way to model progressive damage in fiber-reinforced composites.

It states that an instant reduction in stiffness is presented after the damage has occurred.

Furthermore, this reduction is in the specific damage mode, as can be inferred from equation (78):

$$[\mathbf{D}]_d = \begin{bmatrix} \frac{C_{11}}{(1-d_f)} & C_{12} & C_{13} & 0 & 0 & 0 \\ C_{21} & \frac{C_{22}}{(1-d_m)} & C_{23} & 0 & 0 & 0 \\ C_{31} & C_{32} & \frac{C_{33}}{(1-d_m)} & 0 & 0 & 0 \\ 0 & 0 & 0 & \frac{C_{44}}{(1-d_s)} & 0 & 0 \\ 0 & 0 & 0 & 0 & \frac{C_{55}}{(1-d_s)} & 0 \\ 0 & 0 & 0 & 0 & 0 & \frac{C_{66}}{(1-d_s)} \end{bmatrix}^{-1} \quad (78)$$

Where $d_f, d_m,$ and d_s are the damage variables for the fiber, matrix, and shear, respectively, and $[\mathbf{D}]_d$ is the damaged elasticity matrix. The damage variables are constant and equal to the stiffness reduction factor, and their value must be specified. Valid values are between 0 to 1, where 0 indicates no damage and one a complete loss of stiffness. The ply discount method could be considered a sub-type of instant stiffness reduction method in which the reduction factor or damage variables are all set to 1. All the failure criteria can be applied to this damage model to define the damage activation function.

6.1.3 Matzenmiller Damage Model

Matzemiller et al. (Matzenmiller et al., 1995) developed an elastic-brittle damage model for fiber-reinforced composites. Their proposed model relies on the following assumptions:

- UD laminae are considered based on a homogenized continuum. Also, plane stress conditions are assumed adequate.

- The elasticity moduli of the undamaged UD-lamina can be calculated from simple micromechanical equations.
- The stress-strain response is known to be very nonlinear, especially for shearing. However, linear elasticity is assumed to hold if the damage state does not change, implying linear elastic unloading and reloading in stress-strain space. Therefore, no plasticity is supposed to occur.
- The orthotropic nature of the lamina as a homogenized continuum is maintained throughout the damaging process. Therefore, the symmetry class of the UD-lamina remains the same for all states of damage.
- The constitutive model is considered rate independent.

The failure criterion for the damage model is Hashin, which accounts for four types of failure mechanisms: matrix crushing due to transverse compression, fiber buckling or kinking due to longitudinal compression, matrix cracking due to transverse tension, and fiber fracture from tensile longitudinal stresses. Hashin failure criterion is given in equation (79) to equation (82):

$$\left(\frac{\sigma_{11}}{F_{1T}}\right)^2 + \left(\frac{\sigma_{12}}{F_6}\right)^2 = 1, \quad \sigma_{11} > 0 \quad (79)$$

$$\sigma_1 = -F_{1C}, \quad \sigma_1 < 0 \quad (80)$$

$$\left(\frac{\sigma_{22}}{F_{2T}}\right)^2 + \left(\frac{\sigma_{12}}{F_6}\right)^2 = 1, \quad \sigma_{22} > 0 \quad (81)$$

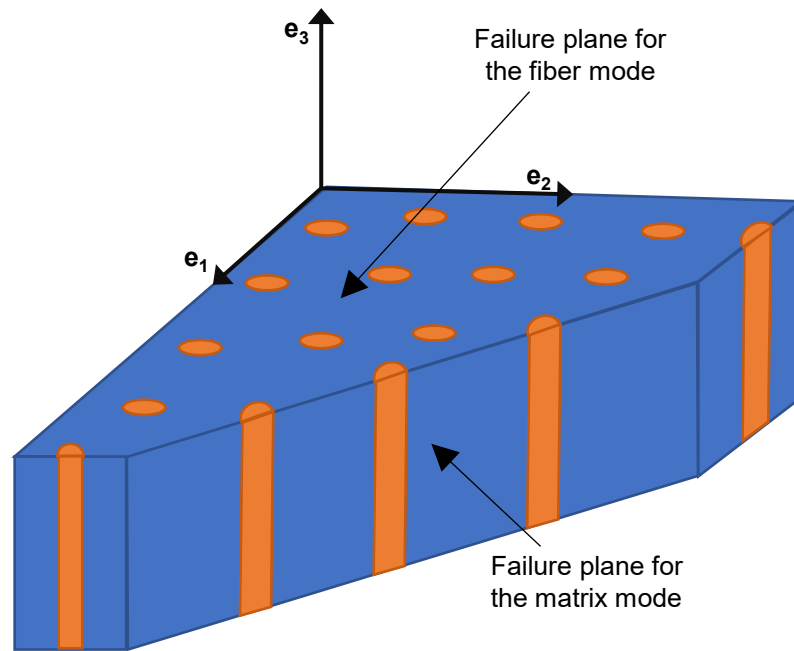
$$\left(\frac{\sigma_{22}}{2F_4}\right)^2 + \left[\left(\frac{F_{2C}}{2F_4}\right)^2 - 1\right] \frac{\sigma_{22}}{F_{2C}} + \left(\frac{\sigma_{12}}{F_6}\right)^2 = 1, \quad \sigma_{22} < 0 \quad (82)$$

The threshold variable will take the role of the equivalent von Mises stress in elasticity in damage mechanics. The assumption of orthotropy even in the damaged state implies that the

damage modeling is by two arrays of parallel cracks, coinciding with the failure planes in Figure 65.

Figure 65

Failure planes of the composite lamina



The rate of evolution of the damage variables is assumed to be locally governed by the local state variables σ, d_i . If no “healing” is present, then the damage variable must be monotonically increasing ($\dot{d}_i \geq 0$) when damage takes place. Also, the rate equations of the damage, see equation (83), must allow for coupling among them or independent growth if that is the case.

$$\dot{d}_{11} = \frac{\phi_1 2E_1}{F_{1c}^2}, \quad \dot{d}_{22} = \frac{\phi_2 2E_2}{F_{2c}^2}, \quad \dot{d}_{12} = \frac{\phi_2 2G}{F_{6c}^2} \quad (83)$$

In which ϕ_i are the associated damage variables. Given the dissipation inequality of equation (84):

$$D = (Y, d) \geq 0 \quad (84)$$

Where Y is analogous to the energy release rate. Nevertheless, in CDM, the variables Y have the energy released per volume due to the advancement of damage. They are the thermodynamic forces conjugate to the damage variables, d_i as the equation (85) shows.

$$Y = -\frac{\partial W}{\partial d} \quad (85)$$

Where W is the the Free energy of anisotropic damaged material. The computational implementation of the model establishes that the damage evolution analysis requires eight parameters: four values of energy dissipated per unit are (G_C) and four viscous damping coefficients. The G_C parameter is defined as in equation (73).

For the computational implementation, the four damage evolution parameters are the energies dissipated per unit area from: tensile fiber damage, compressive fiber damage, tensile matrix damage and compressive matrix damage.

Then, the damage variables for calculating the damage elasticity are determined as in equation (86) and equation (87)

$$d_f = \begin{cases} d_f^+ & \text{if } \tilde{\sigma}_{11} > 0 \\ d_f^- & \text{if } \tilde{\sigma}_{11} < 0 \end{cases}; \quad d_m = \begin{cases} d_m^+ & \text{if } \tilde{\sigma}_{22} > 0 \\ d_m^- & \text{if } \tilde{\sigma}_{22} < 0 \end{cases} \quad (86)$$

$$d_s = 1 - (1 - d_f^+)(1 - d_f^-)(1 - d_m^+)(1 - d_m^-) \quad (87)$$

Where $\tilde{\sigma}_{11}, \tilde{\sigma}_{22}$ stands for fiber and, matrix failure calculated from effective stress $\tilde{\sigma}$.

In Matzenmiller CDM damage model, damage increase gradually based on the energy dissipated for the various damage modes. To achieve convergence, the regularization is needed as shown in equation (88) and equation (89)

$$g_v = \frac{G_c}{L_e} \quad (88)$$

In which L_e is calculated in term of the area A as:

$$L_e = \begin{cases} 1.12\sqrt{A} & \text{for square element} \\ 1.52\sqrt{A} & \text{for triangular element} \end{cases} \quad (89)$$

6.1.4 Maimí Damage Model

More recently, Maimí et al. (Maimí et al., 2007a, 2007b) developed a continuum damage model appropriate for the quasi-brittle failure of fiber-reinforced laminates. Their model requires materials properties obtained from standards test methods and uses a ply-based perspective rather than laminate testing.

Maimí's model considers the effect of the ply thickness on shear strength and the closure of transverse cracks under load reversal, also known as the unilateral effect. The damage activation function in their model is a simplified version of the LaRC04. Finally, it tracks the damage caused by tension loads separately from damage caused by compression loads.

Some drawbacks of the model are that the delamination is not considered, and it requires the programming of a rather complex material routine in the FEA software (Maimí et al., 2007b).

6.2 Verification and Validation

The progressive failure analysis framework subdivides the stress-strain response of material into the elastic, pre-peak, failure criteria, and post-peak regimes. The response of a material model

in a PDFFA method can be verified and validated in each regime independently to establish the strengths and weaknesses.

The process of verification and validation helps establish confidence in the results of complex numerical simulations. Although this process is such a critical stage that ASME has a guide to verification and validation in computational mechanics (ASME, 2019). The guide is a compendium of recommended practices rather than a step-to-step guide on performing verification and validation. The guide defines those processes as:

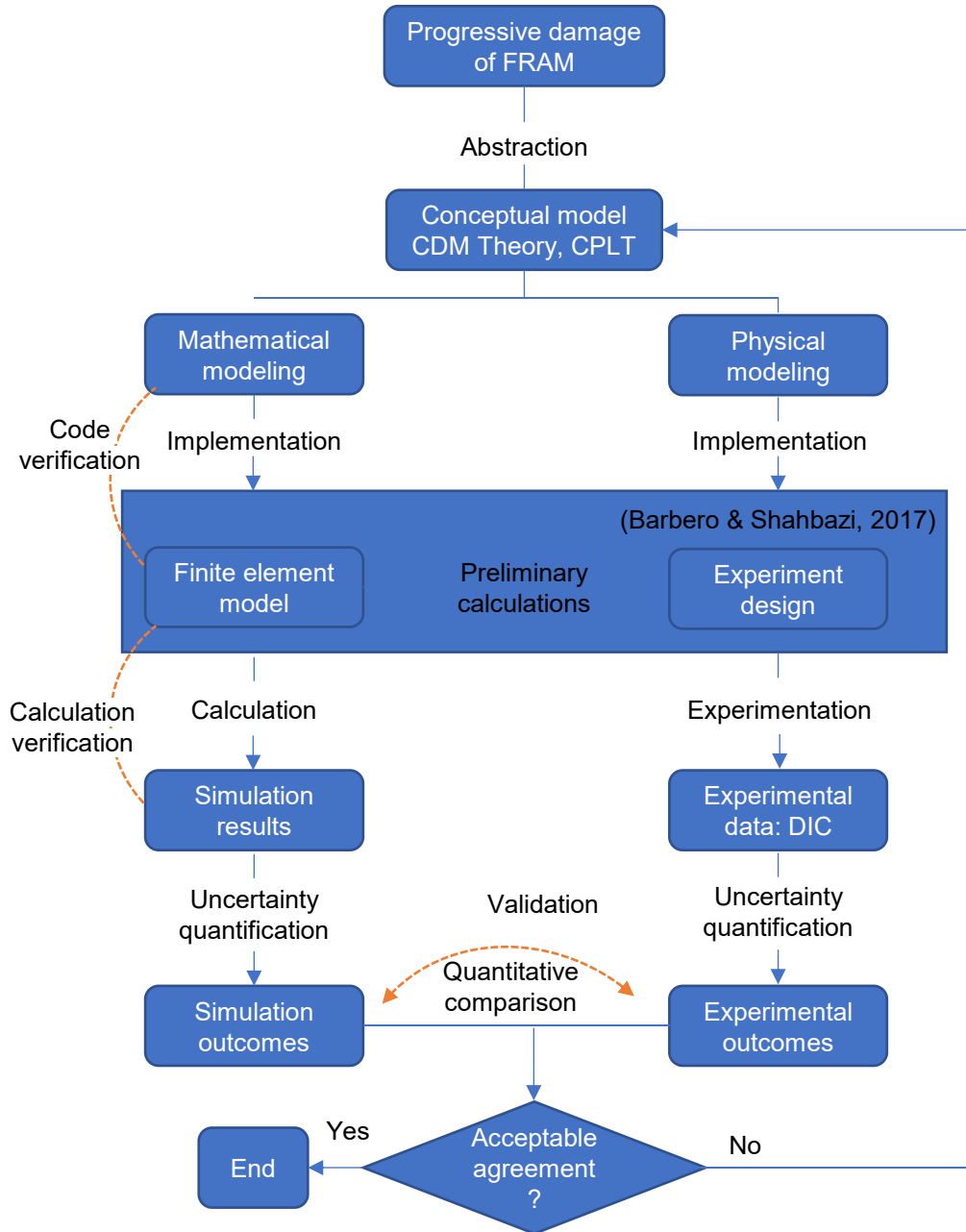
Verification: determining that a computational model accurately represents the underlying mathematical model and its solutions.

Validation: The process of determining the degree to which a model accurately represents the real world from the perspective of the intended uses of the model.

The schematic process for the verification and validation used in this work is summarized in Figure 66.

Figure 66

Schematic of the verification and validation process



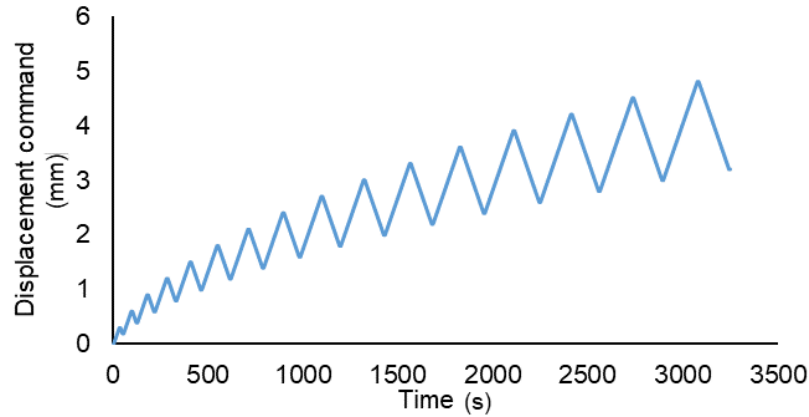
6.3 Experimental Validation and Experimental Stress Analysis

The experimental validation consists first of a material parameter characterization, finding the eight parameters of the damage model described in (Barbero & Shahbazi, 2017). This methodology can find the values by numerically adjusting two stiffness degradation curves of different laminates. After, numerical simulations of the open hole, run with the above-determined parameters, are compared with 2D-DIC experimental data.

First, two different laminates were 3D printed to determine the damage parameters via a pseudo cyclic tensile test, as performed by (Barbero & Shahbazi, 2017). The applied displacement versus time curve is shown in Figure 67. In each cycle, the tangent stiffness was calculated to find the stiffness degradation as a function of the applied strain, and this data could be used to determine the damage properties of the material in the Matzenmiller damage model. The used parameters are depicted in the numerical results section of this chapter. Next, damage parameters characterization was conducted on a tensile test in a Bionix 370.02 MTS equipped with a mechanical extensometer for the first stiffness calculation, a built-in displacement sensor, and a 25 (kN) load cell completed the setup. Appropriate tabs were placed following the ASTM D3039 standard. The rate was 2 mm/min in a pseudo cyclic manner. First increasing, then discharge, and further increasing to a new maximum displacement.

Figure 67

Pseudo-cyclic test used for damage characterization in the Bionix 370.02 MTS



Onyx, a trademarked material, property of Markforged, was 3D printed on an Onyx Pro desktop printer. Onyx is a mixture of chopped carbon fibers in a thermoplastic matrix. Continuous reinforcements of fiberglass and Kevlar were employed for the fiber extruder, and two different laminates were 3D printed following the below-mentioned in Table 16 printing parameters:

Table 16

Printing parameters of the tested specimens for damage characterization

Property or parameter	Value
Composite laminate sequence	$[0_1/\pm 40_4/0_{1/2}]_s, [0_2/90_4]_s$
Continuous fiber type	Kevlar and fiberglass
Polymeric material	Onyx – chopped carbon fibers in nylon.
Dimensions	160 × 15 × 3 mm
Print direction	Flat
Extruder temperature	260 °C
Layer height	0.1 mm
Number of plastic layers	Four top, Four Bottom, and a ten-layer core after the sixth layer.

Stress is a derived physical quantity because it is not directly measurable. It is possible, for instance, to find the force and, given the area, find the stress. Alternatively, obtain the strain from the displacements and find the stress using the material constitutive equations. Experimental stress analysis involves the determination of the stresses in a machine component or a material test coupon. A possible classification will be into local and global measurements techniques. Point or local stress techniques can include strain gauges and load cells.

Conversely, full-field measurements overview the entire stress field or a particular region interest (ROI). Some full-field measurements techniques include digital image correlation, Moiré patterns, photoelasticity, and laser interferometer techniques.

DIC is a full-field displacement measurement technique. It consists of a sequence of images of a moving object and a tracking process. The tracking process is performed on features in each image, and the image location can be converted into the position. A random pattern is more appropriate than a dot matrix, but the latter is simpler to implement. It is possible to get a thousand magnitude improvement in displacements, and thus, it can measure stretches of a few microns. Applications are model validation, material characterization, and real-time monitoring. DIC is material independent, load-independent, and also, as an advantage over strain gages, it can be used repeatedly.

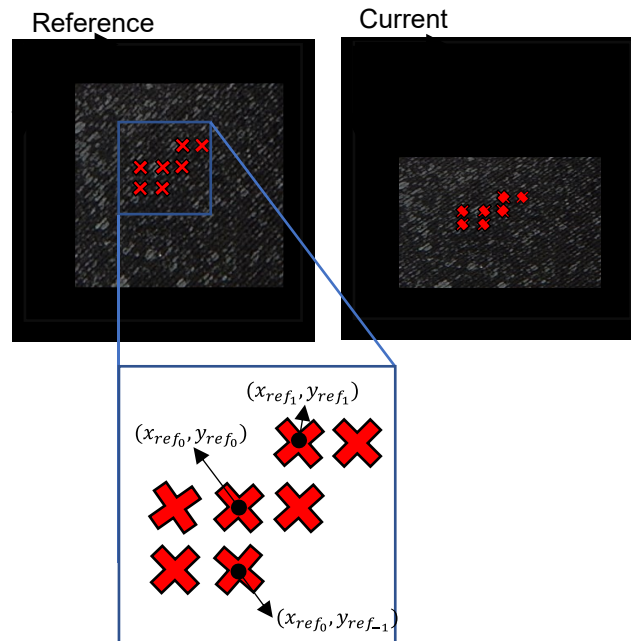
DIC tries to find a one-to-one correspondence between material points in the reference (initial undeformed picture) and current (subsequent deformed pictures) configurations. This one-to-one correspondence is done by taking small subsections of the reference image, called subsets, and determining their respective locations in the current configuration. Then, for each subset displacement and strain information is obtained through the transformation used to match the

location of the subset in the current configuration. The displacement/strain fields can then be reduced or interpolated to form a "continuous" displacement/strain field.

Subsets are essentially a group of coordinate points; the idea of subsets in the reference and current image is shown in Figure 68.

Figure 68

Reference and current configuration for DIC treatment. Coordinates of the subsets are shown as red crosses, notation at the bottom is used throughout the rest of the chapter



It is intended to find the optimal displacement vector P_{rc} , when $P_{rr} = 0$. r, c relates to the reference and current subset. This optimal vector is such that the coordinates x_{ref} , and y_{ref} best match the coordinates x_{cur} and y_{cur} . With $(i, j) \in S$.

$$\tilde{x}_{cur_i} = x_{ref_i} + u_{rc} + \frac{\partial u}{\partial x_{rc}}(x_{ref_i} - x_{ref_c}) + \frac{\partial u}{\partial y_{rc}}(y_{ref_j} - y_{ref_c}) \quad (90)$$

$$\tilde{y}_{cur_j} = y_{ref_j} + v_{rc} + \frac{\partial v}{\partial x_{rc}}(x_{ref_i} - x_{ref_c}) + \frac{\partial v}{\partial y_{rc}}(y_{ref_j} - y_{ref_c}) \quad (91)$$

$$P = \left\{ u, v, \frac{\partial u}{\partial x}, \frac{\partial u}{\partial y}, \frac{\partial v}{\partial x}, \frac{\partial v}{\partial y} \right\}^T \quad (92)$$

The second step is to establish a metric for the similarity between the final reference and the current subset. Equation (93) is called the cross-correlation coefficient, and it is more correlated when close to 1, while equation (94) is the least-square coefficient correlation, and the closer the match, the close to zero is the value. A common correlation metric is C_{LS} given by equation (94)

$$C_{CC} = \frac{\sum_{(i,j) \in S} (f(\tilde{x}_{ref_i}, \tilde{y}_{ref_j}) - f_m)(g(\tilde{x}_{cur_i}, \tilde{y}_{cur_j}) - g_m)}{\sqrt{\sum_{(i,j) \in S} [f(\tilde{x}_{ref_i}, \tilde{y}_{ref_j}) - f_m]^2 \sum_{(i,j) \in S} [g(\tilde{x}_{cur_i}, \tilde{y}_{cur_j}) - g_m]^2}} \quad (93)$$

$$C_{LS} = \sum_{(i,j) \in S} \left[\frac{f(\tilde{x}_{ref_i}, \tilde{y}_{ref_j}) - f_m}{\sqrt{\sum_{(i,j) \in S} [f(\tilde{x}_{ref_i}, \tilde{y}_{ref_j}) - f_m]^2}} - \frac{g(\tilde{x}_{cur_i}, \tilde{y}_{cur_j}) - g_m}{\sqrt{\sum_{(i,j) \in S} [g(\tilde{x}_{cur_i}, \tilde{y}_{cur_j}) - g_m]^2}} \right]^2 \quad (94)$$

Where f and g are the references and current image functions, respectively, they return a grayscale value corresponding to the specified (x, y) point. f_m and g_m are the mean grayscale values of the final reference and current subset, respectively.

Therefore, DIC relies on nonlinear optimization to find the best transformation P_{rc}^* such that it minimizes equation (94). There are multiple methods to perform this optimization, and the most common are: the forward additive Gauss-Newton method (FA-GN) and inverse composition Gauss-Newton method (IC-GN). Those are iterative process methods that lead to the displacement of the center point. The full-field displacement data can be obtained first by selecting a region of

interest (ROI) and determining the displacement data in a grid. Then, the displacements are interpolated to form a continuous displacement field.

Finally, strains ($[E]$) are obtained via the differentiation of the displacement field, which could be challenging because it involves differentiation sensitive to noise. Equation (95) to equation (97) state the 2D Green-strain tensor components.

$$E_{xx} = \frac{1}{2} \left(2 \frac{\partial u}{\partial x} + \left(\frac{\partial u}{\partial x} \right)^2 + \left(\frac{\partial v}{\partial x} \right)^2 \right) \quad (95)$$

$$E_{xy} = \frac{1}{2} \left(\frac{\partial u}{\partial y} + \frac{\partial v}{\partial x} + \frac{\partial u}{\partial x} \frac{\partial u}{\partial y} + \frac{\partial v}{\partial x} \frac{\partial v}{\partial y} \right) \quad (96)$$

$$E_{yy} = \frac{1}{2} \left(2 \frac{\partial v}{\partial y} + \left(\frac{\partial u}{\partial y} \right)^2 + \left(\frac{\partial v}{\partial y} \right)^2 \right) \quad (97)$$

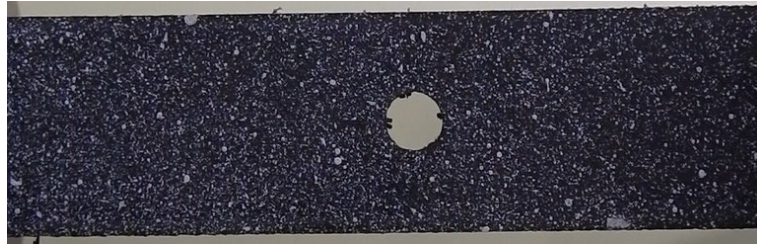
An open hole test of a $[45/90/-45/0]_{2S}$ 3D printed laminate was performed to analyze and validate the results, and the displacement field was obtained through a digital image correlation technique using a Nikon camera Coolpix L830 with Zoom-Nikkor ED VR lens with a focal length of 50 mm, 16.1 Megapixel CMOS Sensor. The images were processed in Ncorr correlation software (Blaber et al., 2015), for the calibration metric the width of the sample across the hole was measured with a micrometer and used as reference length. The speckle pattern was generated using the paint and brushing procedure but first, the surface was prepared with appropriate polishing with carbide paper starting incrementally from 120 grits to 1200 grits for 2 minutes each. Figure 69 depicts the open hole specimen with the speckle pattern in its surface. In AM parts, the surfaces are rough, and oriented in a pattern, dominated by the raster angle. The pattern makes the painting of the speckle to have an oriented direction. Thus, a not anisotropic pattern, with which

the analysis is not recommended. Therefore, the specimens were grinded, provided that the stiffest layers were the reinforced ones, and will not affect the test.

Low-cost DIC solutions have been already assessed, and their performance is good, making them suitable for the present application (Das et al., 2021; Harilal & Ramji, 2014).

Figure 69

Open hole specimen speckle pattern viewed from the DIC camera



6.4 Results

This section presents the results of the experimental verification and validation campaign, both for damage determination and the open hole tests. Then, in a second moment, the numerical results are displayed. In this case, only the open-hole test is presented. The final part presents the validation of the Matzenmiller models in different magnitudes, such as strain and stress components, showing the relative error metric. Finally, the influence of the temperature and the dynamical behavior is stated.

6.4.1 Numerical Results

The material properties used in this work are presented in Table 17, where tensile tests were performed for the Onyx. Besides, the works of different authors were consulted

(Ghebretinsae et al., 2019; Pascual-González et al., 2020). The properties for the fiberglass came from the work of (Justo, Távora, García-Guzmán, et al., 2018) and our own experiments. Kevlar material properties are found in (Kabir et al., 2020; Oztan et al., 2019). Finally, Carbon fiber properties are available in (Iragi et al., 2019) and from this work in chapter 4. Also, where convenient, micromechanical equations were applied to find the remaining data, and this process was generally used for difficult to find properties such as G_{23} , and ν_{23} .

Table 17

Summary of the material properties used in the numerical model

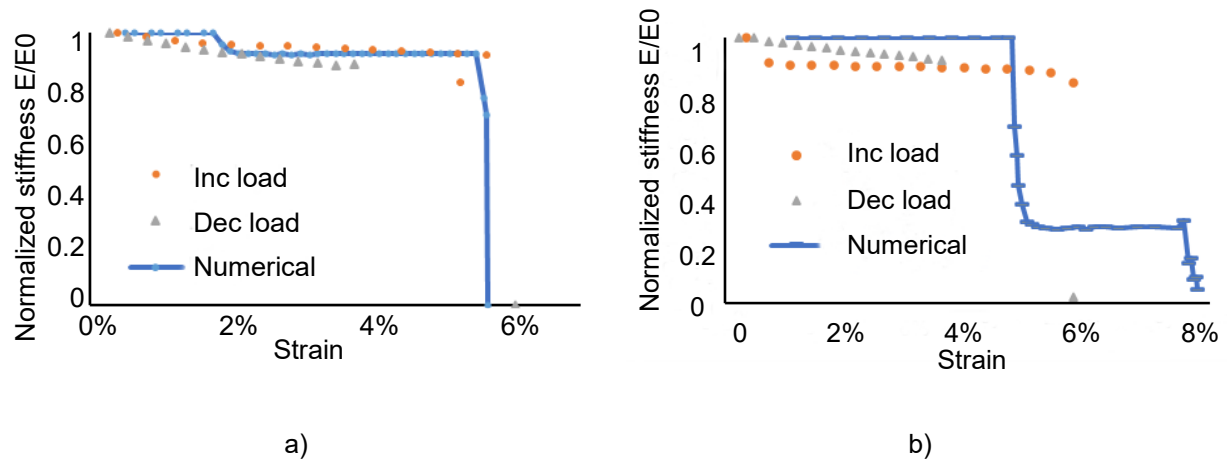
Property or parameter	Materials		
	Onyx	Fiberglass	Kevlar
E_1	1.2 – 1.4 GPa	21 GPa	27 GPa
ν_{12}	0.43	$0.36 = \nu_{13}$	$0.38 = \nu_{13}$
S_Y	36-39 MPa	NA	NA
S_{ut}	54 – 69 MPa	NA	NA
ϵ_{ut}	260% - 311%	NA	NA
E_2	NA	$1.13 \text{ GPa} = E_3$	2.60 GPa
G_{12}	0.41 - 0.49 GPa	$0.88 \text{ GPa} = G_{13}$	$1.48 \text{ GPa} = G_{13}$
Material model	Bilinear elasto plastic	Orthotropic elasticity with damage	Orthotropic elasticity with damage
Tangent modulus	100 MPa	NA	NA
G_{23}	NA	0.71 GPa	1.37 GPa
ν_{23}	NA	0.3	0.36
F_{1T}	NA	574 - 590 MPa	610 MPa
F_{1C}	NA	-82 -130 MPa	-130 MPa
F_{2T}	NA	9.84 MPa	55.00 MPa
F_{2C}	NA	-12.73 MPa	-55.00 MPa
F_6	NA	67.77 MPa	48.00 MPa

The numerical models were created in ANSYS v2021, using the ACP module which allows a ply-wise definition of the composite laminate. Figure 70 shows the tensile test in a pseudo cyclic

manner, the stiffness response vs. the applied strain is graphed, and the comparison with the Matzenmiller damage models is presented.

Figure 70

Stiffness degradation in a tensile test for 3D printed laminates: a) L1 $[0_2/90_4]_s$, b) L8 $[0_1/+40_4/0_1/2]_s$



The errors in the curves are consistent with the great material properties values dispersion, the curve was fitted to the first laminate L1. The adjusted numerical model of the laminates was performed with the material parameters shown in Table 18:

Table 18

Damage material properties, fiber tensile, compressive, matrix tensile, and compressive for fiberglass and Kevlar.

Material	G_{CFT} (N.mm ⁻¹)	G_{CFC} (N.mm ⁻¹)	G_{CMT} (N.mm ⁻¹)	G_{CMC} (N.mm ⁻¹)	η_{damp}
Fiberglass	1760	1700	44.45	1134	0.001
Kevlar	1711	1647	37.61	998	0.001

6.4.2 Experimental Results

Open hole stress-strain is shown in Figure 71. It is clear that this general or lumped approach lacks enough information for complete model validation. Therefore, DIC analysis complements the validation framework.

Open hole test specimens are a [45/90/-45/0]_{2S} laminate, such that 16 layers are arranged in the following way: [45/90/-45/0/45/90/-45/0/Core/0/-45/90/45/0/-45/90/45] where the core consist of six Onyx layers.

Figure 71

Average stress-strain response of the open hole laminates: a) Onyx reinforced with Kevlar, b) Onyx reinforced with fiberglass

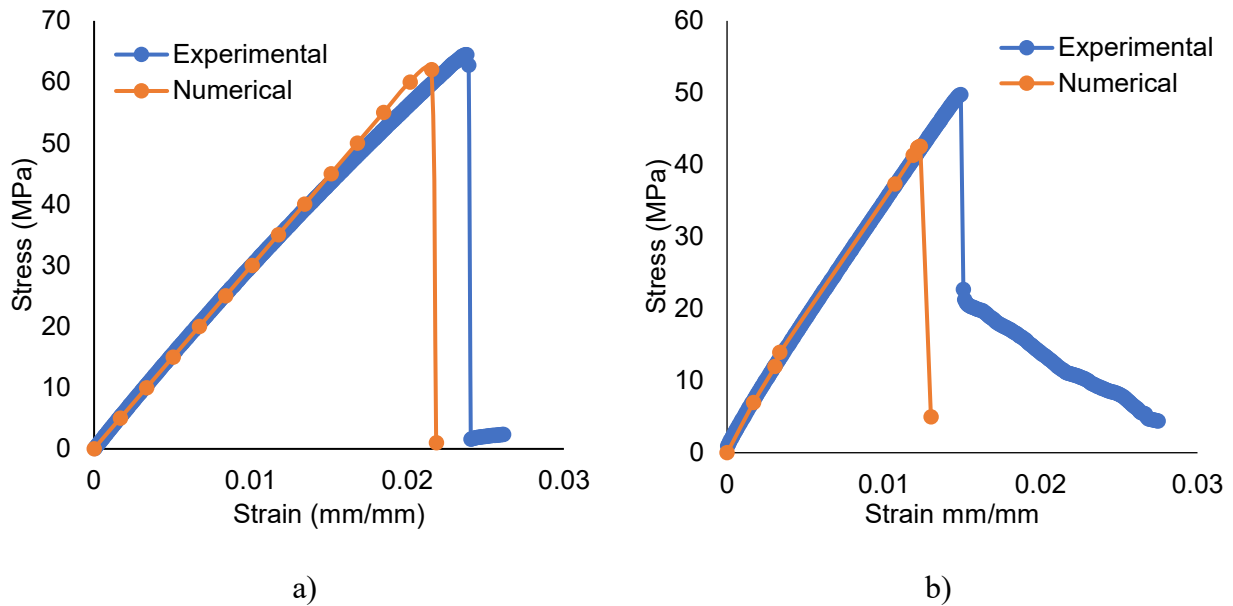
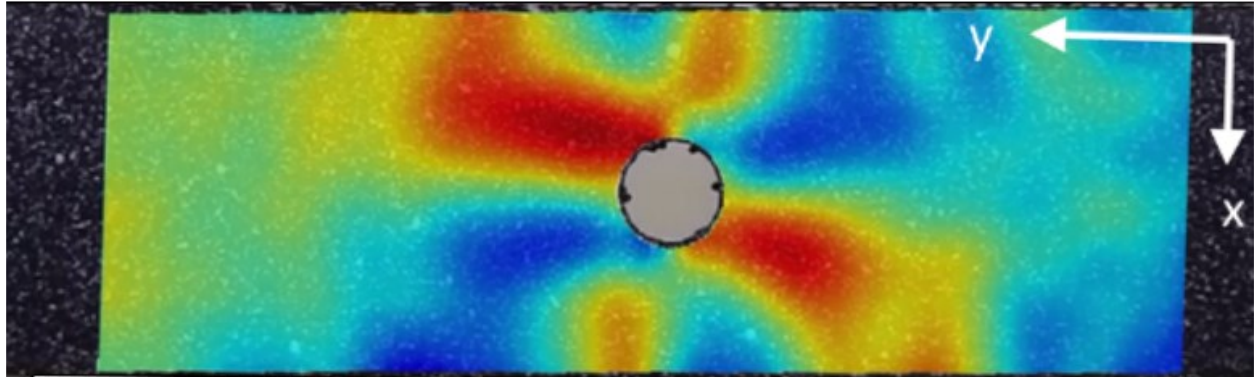


Figure 71 depicts a good agreement between the numerical model and the experimental model, this in terms of the stiffness. However, the numerical model tends to underestimate the maximum stress of the laminate in both cases. Although the agreement is fair good this does not imply a full validation of the numerical model because it can exist multiple values with similar stress-strain response. Thus, it is frequent to employ full-field displacements techniques to validate the model in a correct manner.

Figure 72 shows an output image for the shear strain of the processed Ncorr video. The video files for the different test results can be viewed in Appendix A. The X axis is oriented towards the width of the part and the Y axis to the longitudinal axis of the part, a Lagrangian visualization of strains is performed, meaning in the non-deformed configuration.

Figure 72

In-plane shear field of processed DIC strain results in Ncorr

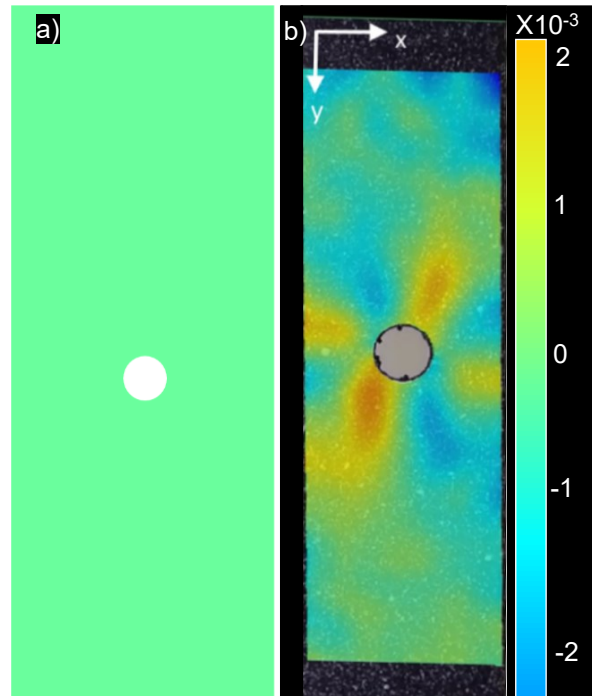


6.4.3 Model Validation

The numerical model was validated through comparisons with the experimental DIC data. The mesh employed for the numerical model was a quadratic quadrilateral dominated mesh with a maximum element size of 5 mm. For validating, the strain fields were compared, particularly the shear strains in Figure 73, the X normal strains in Figure 74, and the Y normal strain in Figure 75 with the top ply, which is analyzed in the DIC technique. The scale in the figures are for both experimental and numerical data.

Figure 73

Shear strain comparison at $F=2500N$, both results are close to zero: a) numerical model, b) experimental with DIC technique



Although some shear bands are visible in the experimental data, their strain value is low ($1E-3$ %) and thus can be considered a zero-value field as in the numerical case.

Figure 74

Normal strain in the x direction at $F=2500N$: a) numerical technique, b) experimental DIC

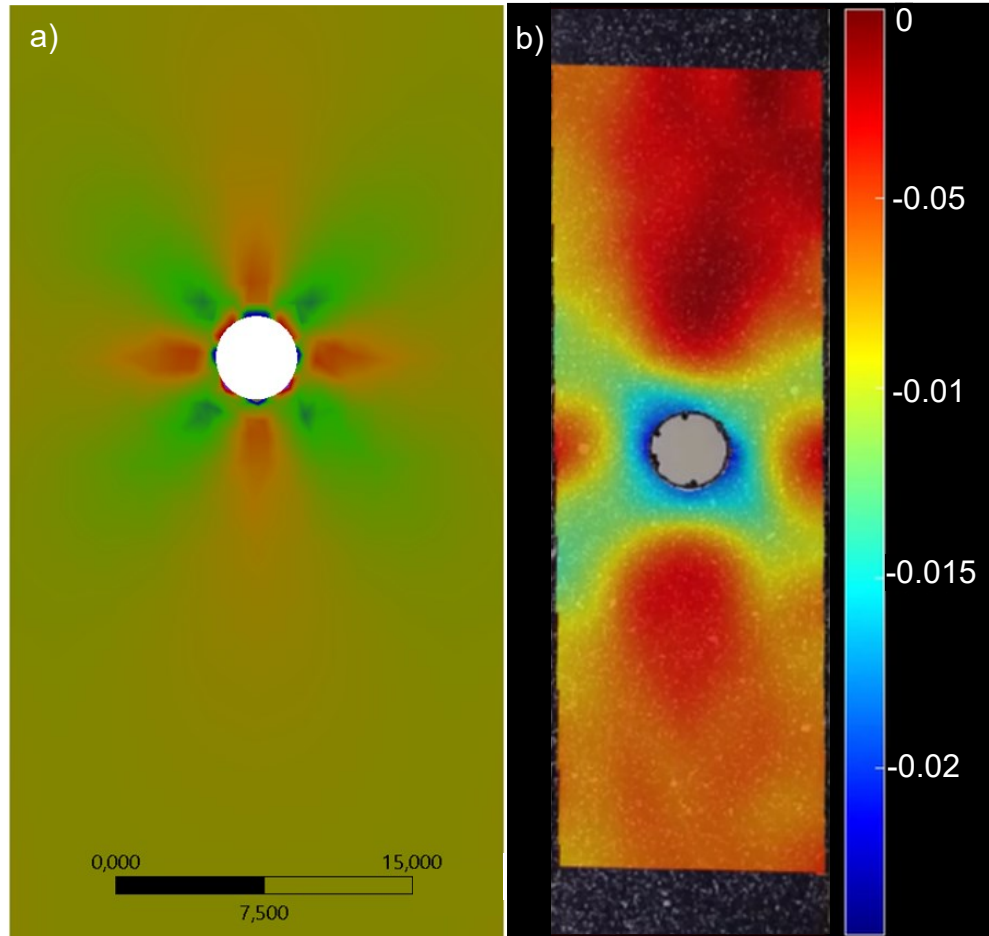
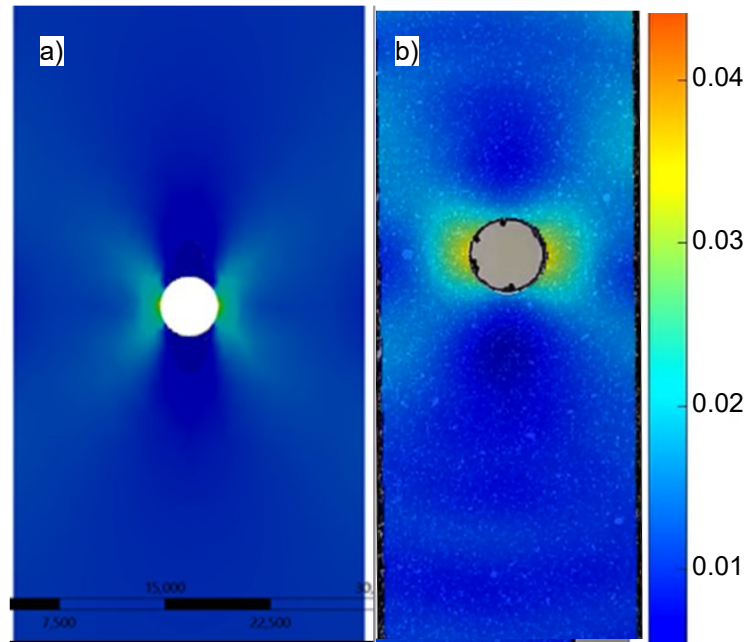


Figure 74 represents the X normal strains with values ranging from 0 to 0.005 mm/mm . The same pattern for the X normal strain field is observed for the experimental and the numerical tests. The experimental test shows a wider area where strains around the hole are softened.

Figure 75

Validation using normal strain in the y direction at $F= 2500N$: a) numerical model, b) experimental

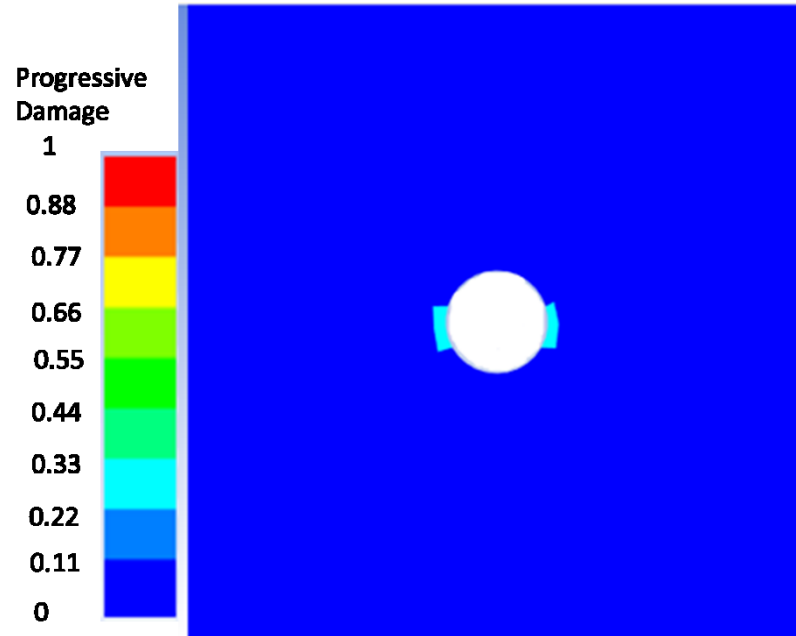


As the Figure 75 shows, the normal strains in the Y-axis for both tests look very similar. Furthermore, there is a high strain zone in the lateral points of the hole, in which the maximum occurs. Thus, as the validations show, there is good agreement between the numerical model and the experimental data. Thus, the model could be a suitable representation of mechanical behavior in FRAM.

The numerical model also complements the experimental data. For example, in the DIC technique, the strain information of the outermost layer is visible. Moreover, with a numerical model, it is possible to observe the damage values of the inner layers. Figure 76 shows the matrix tensile damage in the open hole specimen for fiberglass reinforced FRAM near the failure point.

Figure 76

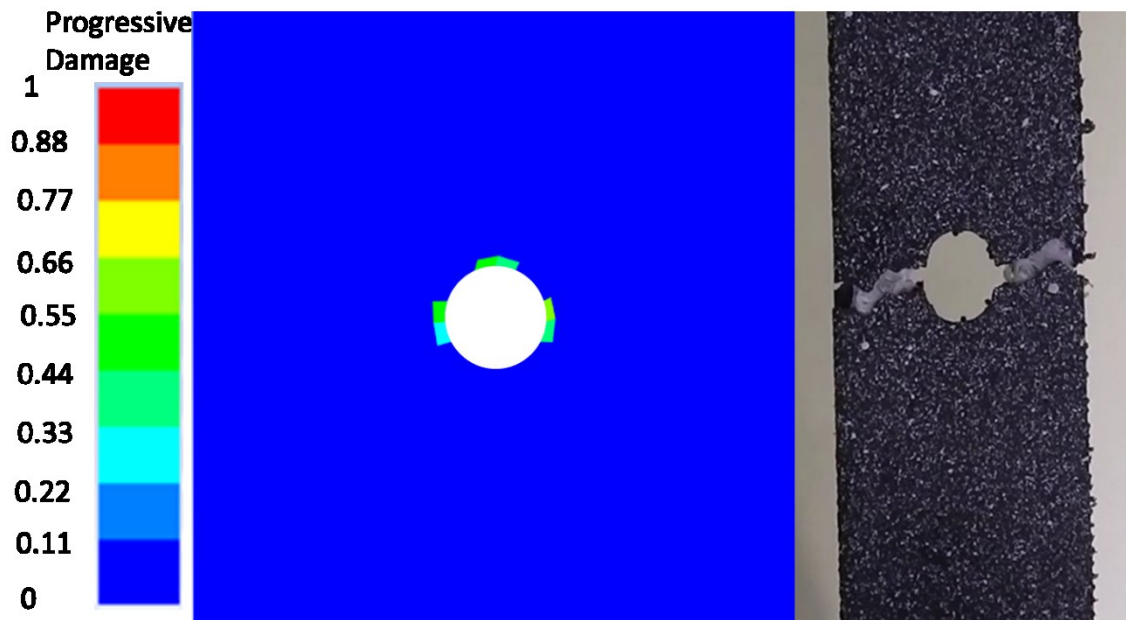
Tensile matrix damage for a 0° layer in a fiberglass open hole specimen



Also, as observed in Figure 77, the shear damage has a greater value, thus, the main failure component is shear stress. This does not imply that the shear component is the highest, but it is the principal damage mechanism in the part. The model predicts failure in the lateral regions of the hole, with a nearly horizontal damage length, and this was observed in the failed sample.

Figure 77

Shear damage for a 0° layer in a fiberglass open-hole specimen



6.5 Source of Errors

In the previous chapters, the static behavior of FRAM was covered, comparing different models analytical, numerical, and data-driven in trying to predict the response of such materials. However, little has been said about the source of errors that are usually neglected. This section aim is to explain two possible factors that could affect the measure but has been disregarded so far, and they are the dynamical behavior and the temperature. In performing the tensile test and suddenly stopping the displacement, an apparent descent in stress was observable, similar to those presented in a relaxation test, implying a contribution of the viscosity term in the component behavior.

Stress relaxation is a way of a viscoelastic behavior showing up and affects how the structure performs in time-dependent loads and temperature variations. For studying this

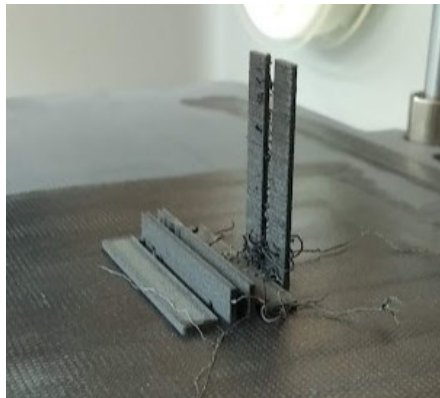
phenomenon, the most extensively used technique is the dynamic mechanical characterization (DMA).

Recent works have included four-dimensional printing of AM composites for aerospace applications (Hoa et al., 2021). In (Mohammadizadeh et al., 2018) the authors perform DMA to continuous fiber-reinforced nylon composites, in a range of 30 to 150 °C and a test frequency of 1 Hz. The work of (Calignano et al., 2020) performed a mechanical test on short fiber chopped carbon reinforcement material. In their study, a nylon-carbon filament (chopped fibers with a random orientation), which had a standard diameter of 1.75 mm, was used for 3D printing. In (Galeja et al., 2020) researchers studied ABS reinforced with chopped carbon fiber, and the DMA was performed using the DMA Q800 TA Instruments apparatus (TA Instruments; New Castle, DE, USA). Samples cut to the dimensions of 40×10×2 mm were loaded with a variable sinusoidal deformation force in the single cantilever bending mode at the frequency of 1 Hz under the temperature rising rate of 4 °C/min within the temperature range between 20 °C and 180 °C. Mohammadizeh et al. also performed creep analysis to 3D printed composites. A creep test was done according to the ASTM standard D2990-17 for the creep test of polymer composite specimens. All specimens were allowed to equilibrate for at least three minutes in test temperature.

In this work, test specimens were fabricated following the specifications in Table 19 in an Onyx Pro 3D printer from Markforged with different printing orientations, as shown in Figure 78.

Table 19*Printing specifications for surface and dynamic mechanical analysis*

Parameter	Value
Material	Onyx, chopped carbon fiber in a polyamide matrix
Layer thickness	0.1 mm
Print directions	Upright, on-edge, and flat
Dimensions	45×7×1.5 mm

Figure 78*3D printed Onyx with different printing directions*

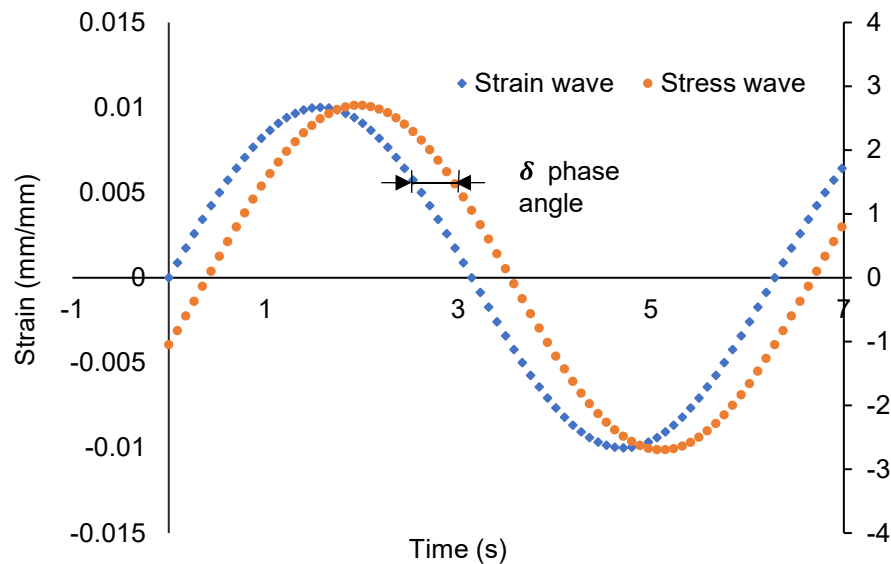
6.6 Dynamic Mechanical Analysis

DMA is a powerful characterization tool for materials, primarily used in polymers, emulsions, liquids, and other materials for rheological studies. DMA works by subjecting an eprouvette to an oscillatory displacement, capturing stress response. Figure 13 depicts the DMA equipment used in this research. If the material is entirely elastic, then the stress wave will be in

phase with the strain wave; however, all materials have a dissipative component, thus, shifting the curve to a delta angle, as Figure 79 shows.

Figure 79

Strain wave and stress wave for a dynamical test as a function of time



The elastic part describes how much the material deforms to given stress or vice versa how much stress is experienced when a set displacement is imposed. It is expressed in terms of Hooke's law $\sigma = E\varepsilon$. One way to characterize the lag in the temporal response is by introducing the viscosity factor η , thus imaging a dashpot as a model, it is expressed in equation (98):

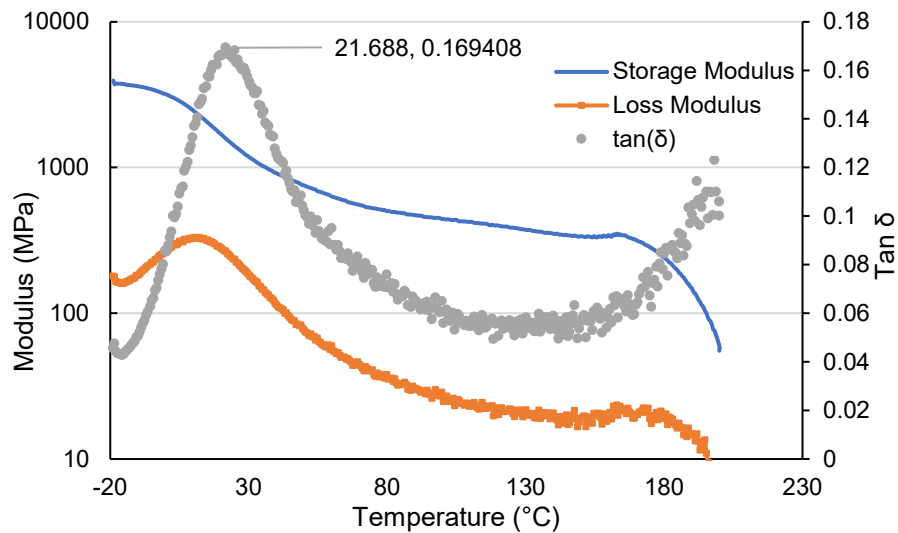
$$\sigma = \eta \dot{\gamma} = \eta \frac{d\gamma}{dt} \quad (98)$$

The viscosity behavior could be used to classify the material. In the linear viscoelastic region, the storage modulus is not affected by the frequency of the test. The storage modulus E' , the viscosity is related to the imaginary part E'' , while E^* is the complex modulus and considers both parts. The $\tan \delta$ is the ratio of real part to the imaginary part.

In a thermomechanical analysis, the temperature is swept across a predefined range using a constant temperature ramp in most cases. Then, the storage and loss modulus are plotted as a function of temperature, and the representative graph is shown in Figure 80.

Figure 80

DMA results for a flat Onyx specimen, T_g is indicated in the graph



The peak $\tan \delta$ graph is the glass temperature transition (T_g). Whereas the final point is called T_m , the melting temperature. Depending on the polymer or material being considered, other temperatures, such as t_{ll} and beta temperature transitions will show that they could be of interest. T_g is important because, in most polymers, it detects a change in the free volume of the polymeric chains, implying that they are freer to move. It is identified by a sharp peak in the $\tan \delta$ curve.

DMA can also be performed by varying the frequency instead of the temperature. The Boltzmann superposition principle and the WLF transformation scheme could be used to relate both frequency and temperature in a master curve. The DMA for Table 19 specimens was performed. The set

temperature was $-20\text{ }^{\circ}\text{C}$ to $200\text{ }^{\circ}\text{C}$ in a $3\text{ }^{\circ}\text{C}/\text{min}$ temperature ramp and a 0.1% strain three-point bending fixture, depicted in Figure 14.

Figure 81

Effect of printing direction in the storage modulus of Onyx

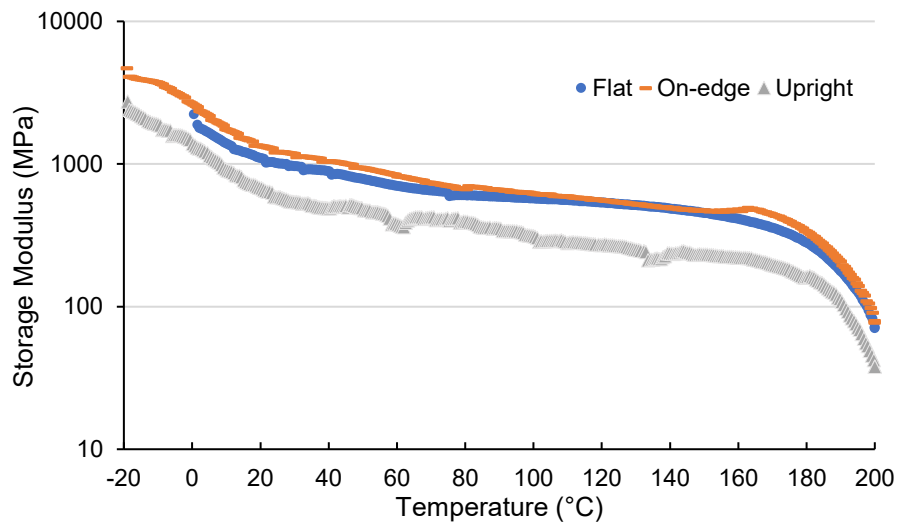


Figure 81 depicts the storage modulus in terms of temperature. First, Figure 81 shows a similar tendency of the storage modulus vs. temperature curve in all three samples. An indication that the printing orientation does not affect the overall storage curve behavior. However, the values of the storage modulus are distinct, it is to note that scale is logarithmic therefore modulus are much more dissimilar than they look in the graph. The upright direction is the least stiff, while the on-edge printed direction presents the highest stiffness value for any given temperature, slightly over the flat printed sample.

The same tendency across all the samples is identified in the loss modulus, see Figure 82. The flat printed sample presents portions of the curve in which the loss modulus is higher than the on-edge

printed. A straightforward descent of the modulus is presented at 160 °C, meaning degradation of the matrix, which initiates the melting process.

Figure 82

Effect of printing direction in the loss modulus of Onyx

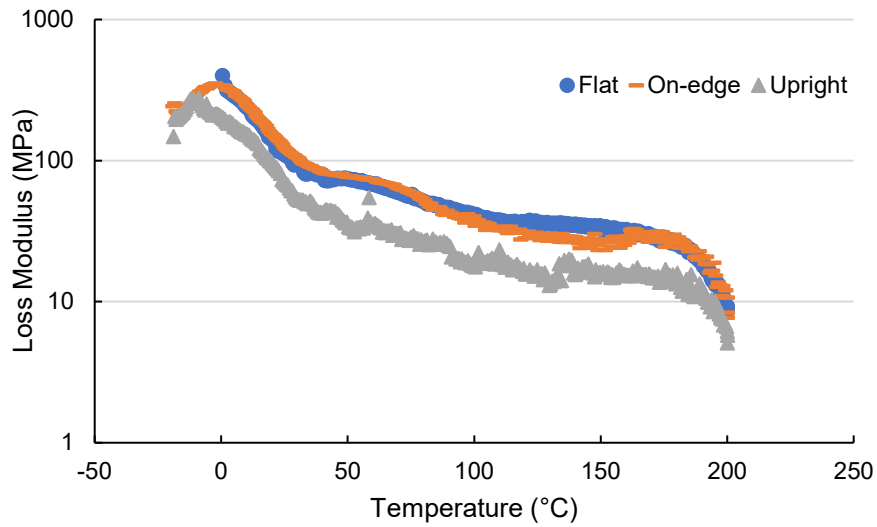
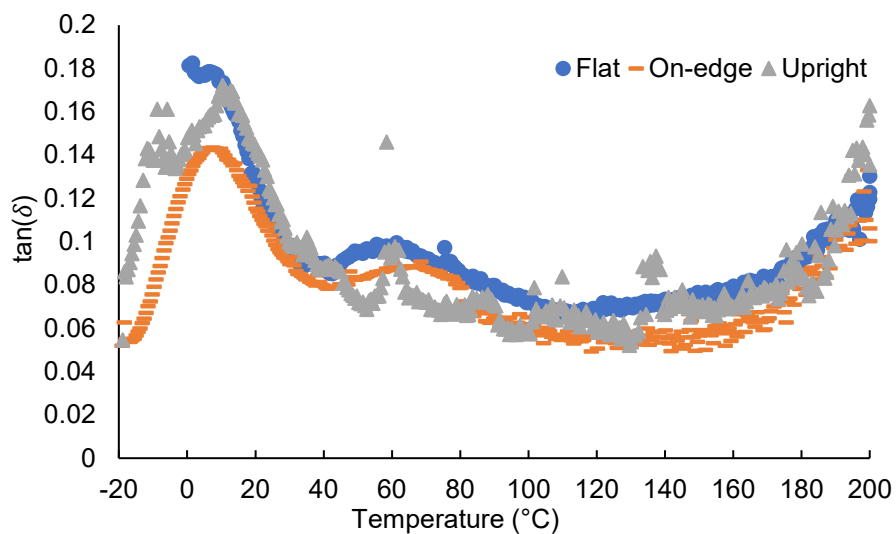


Figure 83

Effect of printing direction in the tan(δ) of Onyx



The $\tan \delta$ could be used to determine the glass transition temperatures of the polymers in a much more accurate way. Figure 83 depicts the curve for the three samples. As a difference from storage or loss modulus, similar values for the three samples were registered. However, some curves have an apparent shift. Thus, T_g is slightly different for all the tested specimens, higher in the upright direction and lowest in the on-edge direction. One surprising fact is that the T_g could be close to the test temperature, being that zone in which significant modulus changes could occur and thus, making it a considerable source of error in the testing of FRAM.

This error would be increase as the proportion of the thermoplastic polymer increases, this provided that the composite region present lower dissipative characteristics as it is most likely to occur (Mohammadizadeh et al., 2018).

6.7 Conclusions of the progressive damage

This chapter states the damage model, the verification and validation process. Results show that the continuum damage mechanics model could be suitable for the integrity determination of AM composites. Despite the validation being in only the outermost ply of the laminate the model can accurately predict the stiffness and the stress state in the AM parts.

Digital image correlation is a powerful technique for analyzing strain fields. However, given the surface finish of the parts, correct surface preparation must be done before the measurements. This grinding could reduce the outermost layers and, thus, the thickness of the piece. Other optical features such different pattern arrangement, ink material and methods (light projection) could be used to improve the DIC setup.

The proposed numerical model with the material properties is a suitable tool for considering damage progression in FRAM components. It can determine the failure zone and the

failure stress with reasonable accuracy. However, the numerical method underestimates the failure point by close to 4% in stress and 9.5 % in strain for the fiberglass case. Also, when having low content of fiber reinforced region, viscoelastic behavior could be a considerable factor of error if a different stress rate is applied. Consequently, caution should be taken when applying to other laminates and thermoplastic materials. Also, the specimens were printed without lattice infills.

The chapter also shows the effect on dynamic behavior of the printing direction in short-fiber reinforced AM parts. The dynamic mechanical properties could feed more elaborated models considering the applied load rate and environmental factors such as temperature.

A disregard for dynamical properties could lead to inaccurate results or a poor experimental design, given that temperature is an essential factor in the study of AM polymers.

7. Conclusions and Future Work

Next, the author present the general conclusions of the thesis, its impact and novelty and frame possible future works.

7.1 General Conclusions

This thesis proposes, implements, and validates a progressive damage model in AM composite materials. The material modeling strategy here used is a modification of the volumetric average stiffness method that considers the created lattice structure configuration and the progressive damage of the composite sections.

The volumetric average stiffness model accurately retrieves the stiffness matrix and the engineering constants in terms of the volumetric fraction and the mechanical behavior of each material region. It predicts the behavior in a tensile test stress state. However, the volumetric

average stiffness, due to the assumption of constant strain in the section, does not take into consideration the order in which the plies are layed-up meaning that for other load states such as bending in which distance from the neutral axis is an essential factor, such a model could not be applied. Authors thus recommend using classical approaches for composite materials, such as the classical laminate theory or first shear order deformation.

Even with the restrictions and the microstructure generated from fiber-reinforced AM components, it was shown that a RVE was suitable to obtain and that it does not invalidate the assumption of continuum made by the progressive damage model.

The effects of diverse manufacturing parameters were assessed by a design of experiment approach. First, it was shown the effect of each manufacturing parameter on the stiffness and strength of fiber-reinforced AM components. Then, different methods were evaluated to predict their mechanical properties, such as micromechanics and data-driven models using machine learning methods. Data-driven could use physics information, as recent work tries to recognize and implement rules in artificial neural networks.

A qualitative study of the fiber-reinforced AM components failure shows diverse failure mechanisms, topologies, and defects. Primary defects concern the layered aspect, which modifies the roughness and the void distribution in the composite region. The failure mechanisms predominantly show matrix damage and defects such as crazes, plastic microflow, river lines, and void coalescence. A more detailed fractographical study is needed to correlate damage variables to microstructural characteristics.

The numerical damage model is validated through open hole specimens, using a strain field measurement technique such as digital image correlation. While being a powerful tool, digital

image correlation lacks the needed ply-wise capabilities for a full 3D validation. Other techniques such as volumetric digital image correlation, acoustic emissions, and Micro Computerized Tomography could be suitable for those validations.

7.2 Impact of the Research and Contributions

The contribution of this thesis is to extend the prediction capabilities of state-of-the-art mechanical characterization methods to take into account different process-related variables such as the specific infill pattern type and densities values, the angle and type of reinforcement fibers, and the printing lay-up direction. Furthermore, it shows that Gibson-Ashby coefficients can be securely applied to AM lattice structures. It presents a comparison of micromechanical and data-driven models to predict the stiffness and strength of continuous fiber AM composites while evaluating their prediction capabilities, speed, and feasibility.

The thesis develops the hypothesis that a continuum damage model can predict progressive damage analysis in AM composites, even in high complexity microstructure and process parameters. The failure mechanisms and the effects of some processing conditions on the microstructure are discussed.

7.3 Future Work

Future work can assess the following areas: Parametric analysis of lattice structures for characterizing strength via a non-linear buckling numerical model.

Interlayer damage is also an essential issue on fiber-reinforced AM components. Layer to layer adhesion affects the mechanical response dramatically, and delamination models could characterize the interlayer strength, such as cohesive zone models, virtual crack closure technique, or multi continuum theory.

When tensile tests were carried on, a tendency of stress reduction when the displacement was fixed at a time was observed, indicating stress relaxation, typically present within viscoelastic materials. There is a recent interest in the dynamic properties of AM, while there is a lack of understanding of composite dynamic behavior. Future work will expand the capabilities of the model to take into account viscosity-related issues. This may be more present with low fiber-reinforced regions parts, in which polymeric content is high.

The search for new applications continues as the range of materials grows. For example, fiber-reinforced AM is currently used with nylon matrix, but new generation plastics like Ultem could also be used. Other high-performance thermoplastics such as PEEK can be tested, but this requires increasing the temperature of the extruder.

Health concerns in AM is also a recent trend, a fusion of thermoplastics could generate volatile organic compounds (VOCs) that are nocive to human. In addition, there are no works of health safety in printing with carbon fibers or other reinforcements.

7.4 List of Publications and Conference Participations

Besides, during the doctoral thesis development, different dissemination and formative activities have been performed.

7.4.1 Published Journal Papers

1. **León B., J.,** Díaz-Rodríguez, J. G., & González-Estrada, O. A. (2020). Daño en partes de manufactura aditiva reforzadas por fibras continuas. *Revista UIS Ingenierías*, 19(2), 161–175. <https://doi.org/10.18273/revuin.v19n2-2020018>

2. **León-Becerra, J. S.**, González-Estrada, O. A., & Pinto-Hernández, W. (2020). Caracterización mecánica de materiales compuestos de fabricación aditiva. *Respuestas*, 25(2). <https://doi.org/10.22463/0122820X.2189>
3. **León-Becerra., J.**, González-Estrada, O. A., Quiroga, Jabid (2021). Effect of relative density in In-plane mechanical properties of common 3D-printed PLA lattice structures. *ACS OMEGA* 2021 6 (44), 29830-29838. DOI: 10.1021/acsomega.1c04295.
4. Díaz, J.G., **León-Becerra, J.**, Pertuz, A.D., González, O.A., Jaramillo, M.I. “Evaluation through sem image processing of the volumetric fiber content in continuous fiber-reinforced additive manufacturing composites”. *Materials Research* 2021 24 (suppl 2) <https://doi.org/10.1590/1980-5373-MR-2022-0049>
5. **Leon-Becerra* Juan**, González Estrada O.A., Heller Sanchez-Acevedo. (2022) “Comparison of models to predict mechanical properties of FR-AM composites and a fractographical study”. *Submitted*.
6. **Leon-Becerra Juan**, Hidalgo-Salazar Miguel, González-Estrada O.A. (2022) “Progressive damage analysis of continuous fiber additive manufacturing composites”, *in progress*.

7.4.2 Conferences

1. Leon-Becerra, Juan., González-Estrada, O.A., & Pinto-Hernández, W. (2019). “Caracterización mecánica de materiales compuestos de fabricación aditiva” Congreso Iberoamericano de Ingeniería mecánica CIBIM 2019. Cartagena de Indias, Colombia. Speaker and author.

2. Leon-Becerra, Juan., &. (2020). “Predicting mechanical properties in fiber reinforced composites produced by additive manufacturing” International mechanical engineering conference and expo IMECE 2020. Portland, United States of America. Speaker and author.

3. Díaz, J.G., Pertuz, A D., González-Estrada, O.A., León-Becerra, J. “Fused deposition modeling fiber content evaluation with digital image treatment techniques” 5th Brazilian Conference on Composite Materials – BCCM 5. Fused deposition modeling fiber content evaluation with digital image treatment techniques. Speaker and coauthor.

References

- Ahmed, S. W., Hussain, G., Altaf, K., Ali, S., Alkahtani, M., Abidi, M. H., & Alzabidi, A. (2020). On the effects of process parameters and optimization of interlaminar bond strength in 3D printed ABS/CF-PLA composite. *Polymers*, 12(9). <https://doi.org/10.3390/POLYM12092155>
- Akasheh, F., & Aglan, H. (2019). Fracture toughness enhancement of carbon fiber-reinforced polymer composites utilizing additive manufacturing fabrication. *Journal of Elastomers and Plastics*, 51(7–8), 698–711. <https://doi.org/10.1177/0095244318817867>
- Al Abadi, H., Thai, H. T., Paton-Cole, V., & Patel, V. I. (2018). Elastic properties of 3D printed fibre-reinforced structures. *Composite Structures*, 193(February), 8–18. <https://doi.org/10.1016/j.compstruct.2018.03.051>
- Araya-calvo, M., López-gómez, I., Chamberlain-simon, N., León-salazar, J. L., Guillén-girón, T., Corrales-cordero, J. S., & Sánchez-brenes, O. (2018). Evaluation of compressive and flexural properties of continuous fiber fabrication additive manufacturing technology. *Additive Manufacturing*, 22(May), 157–164. <https://doi.org/10.1016/j.addma.2018.05.007>
- Argawal, K., Houser, M., Vangapally, S., & Kumar Vulli, A. (2017). Process – Property relationships in additive manufacturing of nylon-fiberglass composites using Taguchi design of experiments. *Solid Freeform Fabrication Symposium*, 399–412.
- Arguëllo-Bastos, J. D., González-Estrada, O. A., Ruiz-Florián, C. A., Pertuz-Comas, A. D., & V-Ninõ, E. D. (2018). Study of mechanical properties under compression failure in reinforced composite materials produced by additive manufacturing. *Journal of Physics: Conference Series*, 1126(1). <https://doi.org/10.1088/1742-6596/1126/1/012005>

- Argüello-Bastos, J. D., Ruiz-Florián, C. A., González-Estrada, O. A., Pertuz-Comas, A. D., & Martínez-Amariz, A. (2018). Compression tests performed in reinforced rigid matrix composite varying the reinforcement material. *Journal of Physics: Conference Series*, 1126(1), 012007. <https://doi.org/10.1088/1742-6596/1126/1/012007>
- ASME. (2019). *Standard for Verification and Validation in Computational Solid Mechanics V V* 10 - 2019 (Vol. 10). ASME Press.
- ASTM. (2014). *Standard test method for tensile properties of polymer matrix composite materials* (Standard No. D3039/D3039M). In Annual Book of ASTM Standards. <https://doi.org/10.1520/D3039>
- ASTM. (2016). *Compressive properties of polymer matrix composites materials with unsupported gage section by shear loading* (Standard No. D3410). In Standard test method.
- Avdeev, A., Shvets, A., Gushchin, I., Torubarov, I., Drobotov, A., Makarov, A., Plotnikov, A., & Serdobintsev, Y. (2019). Strength Increasing Additive Manufacturing Fused Filament Fabrication Technology, Based on Spiral Toolpath Material Deposition. *Machines*, 7(3), 57. <https://doi.org/10.3390/machines7030057>
- Azarov, A. V., Antonov, F. K., Golubev, M. V., Khaziev, A. R., & Ushanov, S. A. (2019). Composite 3D printing for the small size unmanned aerial vehicle structure. *Composites Part B: Engineering*, 169(March), 157–163. <https://doi.org/10.1016/j.compositesb.2019.03.073>
- Azzouz, L., Chen, Y., Zarrelli, M., Pearce, J. M., Mitchell, L., Ren, G., & Grasso, M. (2019). Mechanical properties of 3-D printed truss-like lattice biopolymer non-stochastic structures for sandwich panels with natural fibre composite skins. *Composite Structures*, 213(January), 220–230. <https://doi.org/10.1016/j.compstruct.2019.01.103>

- Bandyopadhyay, A., & Heer, B. (2018). Additive manufacturing of multi-material structures. *Materials Science and Engineering R: Reports*, 129(April), 1–16. <https://doi.org/10.1016/j.mser.2018.04.001>
- Barbero, E. J. (2011). *Introduction to composite materials design* (2nd ed.). CRC Press.
- Barbero, E. J. (2013). *Finite Element Analysis of Composite Materials Using ANSYS* (2nd ed.). CRC Press.
- Barbero, E. J., & Shahbazi, M. (2017). Determination of material properties for ANSYS progressive damage analysis of laminated composites. 176, 768–779. *Composite Structures*, 176, 768–779. <http://dx.doi.org/10.1016/j.compstruct.2017.05.074>
- Belingardi, G., Mehdipour, H., Mangino, E., & Martorana, B. (2016). Progressive damage analysis of a rate-dependent hybrid composite beam. *Composite Structures*, 154, 433–442. <https://doi.org/10.1016/j.compstruct.2016.07.055>
- Bettini, P., Alitta, G., Sala, G., & Di Landro, L. (2017). Fused Deposition Technique for Continuous Fiber Reinforced Thermoplastic. *Journal of Materials Engineering and Performance*, 26(2), 843–848. <https://doi.org/10.1007/s11665-016-2459-8>
- Bhattacharyya, R., & Basu, P. K. (2020). Multiscale progressive damage analysis of CFRP composites using a mechanics based constitutive relation. *Composite Structures*, 235(December 2019), 111759. <https://doi.org/10.1016/j.compstruct.2019.111759>
- Bitar, I. S., Aboulkhair, N. T., & Leach, R. (2017). The application of composite through-thickness assessment to additively manufactured structures. *Solid Freeform Fabrication Symposium*, 616–632.

- Blaber, J., Adair, B., & Antoniou, A. (2015). Ncorr: Open-Source 2D Digital Image Correlation Matlab Software. *Experimental Mechanics*, 55(6), 1105–1122. <https://doi.org/10.1007/s11340-015-0009-1>
- Blok, L. G., Longana, M. L., Yu, H., & Woods, B. K. S. (2018). An investigation into 3D printing of fibre reinforced thermoplastic composites. *Additive Manufacturing*, 22(April), 176–186. <https://doi.org/10.1016/j.addma.2018.04.039>
- Brenken, B., Barocio, E., Favaloro, A., Kunc, V., & Pipes, R. B. (2018). Fused filament fabrication of fiber-reinforced polymers: A review. *Additive Manufacturing*, 21(October 2017), 1–16. <https://doi.org/10.1016/j.addma.2018.01.002>
- Brink, A. W. M. Van Den, Klift, F. Van Der, Bruins, R., & Hermans, M. J. M. (2017). Design and optimization method for 3D printed carbon reinforced aircraft components. *International Conference on Composite Materials, August*.
- Bronz, M., & Karaman, S. (2018). Preliminary Experimental Investigation of Small Scale Propellers at High Incidence Angle. *AIAA Aerospace Sciences Meeting, January*, 1–10. <https://doi.org/10.2514/6.2018-1268>
- Cairns, D. S., Nelson, J. W., Woo, K., & Miller, D. (2016). Progressive damage analysis and testing of composite laminates with fiber waves. *Composites Part A: Applied Science and Manufacturing*, 90, 51–61. <https://doi.org/10.1016/j.compositesa.2016.03.005>
- Calderón-Villajos, R., López, A. J., Peponi, L., Manzano-Santamaría, J., & Ureña, A. (2019). 3D-printed self-healing composite polymer reinforced with carbon nanotubes. *Materials Letters*, 249, 91–94. <https://doi.org/10.1016/j.matlet.2019.04.069>

- Calignano, F., Lorusso, M., Roppolo, I., & Minetola, P. (2020). Investigation of the mechanical properties of a carbon fibre-reinforced nylon filament for 3d printing. *Machines*, 8(3), 1–13. <https://doi.org/10.3390/machines8030052>
- Caminero, M. A., Chacón, J. M., García-Moreno, I., & Reverte, J. M. (2018). Interlaminar bonding performance of 3D printed continuous fibre reinforced thermoplastic composites using fused deposition modelling. *Polymer Testing*, 68(March), 415–423. <https://doi.org/10.1016/j.polymertesting.2018.04.038>
- Caminero, M. A., Chacón, J. M., García-moreno, I., & Rodríguez, G. P. (2018). Impact damage resistance of 3D printed continuous fibre reinforced thermoplastic composites using fused deposition modelling. *Composites Part B*, 148(April), 93–103. <https://doi.org/10.1016/j.compositesb.2018.04.054>
- Caminero, M. A., García-moreno, I., Rodríguez, G. P., & Chacón, J. M. (2019). Internal damage evaluation of composite structures using phased array ultrasonic technique: Impact damage assessment in CFRP and 3D printed reinforced composites. *Composites Part B*, 165(September 2018), 131–142. <https://doi.org/10.1016/j.compositesb.2018.11.091>
- Chabaud, G., Castro, M., Denoual, C., & le Duigou, A. (2019). Hygromechanical properties of 3D printed continuous carbon and glass fibre reinforced polyamide composite for outdoor structural applications. *Additive Manufacturing*, 26(January), 94–105. <https://doi.org/10.1016/j.addma.2019.01.005>
- Chacón, J. M., Caminero, M. A., García-Plaza, E., & Núñez, P. J. (2017). Additive manufacturing of PLA structures using fused deposition modelling: Effect of process parameters on mechanical properties and their optimal selection. *Materials & Design*, 124, 143–157. <https://doi.org/10.1016/j.matdes.2017.03.065>

- Chacón, J. M., Caminero, M. A., Núñez, P. J., García-Plaza, E., García-Moreno, I., & Reverte, J. M. (2019). Additive manufacturing of continuous fibre reinforced thermoplastic composites using fused deposition modelling: Effect of process parameters on mechanical properties. *Composites Science and Technology*, *181*(June 2018), 107688. <https://doi.org/10.1016/j.compscitech.2019.107688>
- Chohan, J. S., Mittal, N., Kumar, R., Singh, S., Sharma, S., Singh, J., Rao, K. V., Mia, M., Pimenov, D. Y., & Dwivedi, S. P. (2020). Mechanical strength enhancement of 3d printed acrylonitrile butadiene styrene polymer components using neural network optimization algorithm. *Polymers*, *12*(10), 1–18. <https://doi.org/10.3390/polym12102250>
- Ciftci, C., & Sas, H. S. (2019). A rational utilization of reinforcement material for flexural design of 3D-printed composite beams. *Journal of Reinforced Plastics and Composites*, 073168441986829. <https://doi.org/10.1177/0731684419868297>
- Das, P. P., Elenchezian, M. R. P., Vadlamudi, V., Reifsnider, K., & Raihan, R. (2021). RealPi2dDIC: A Low-cost and open-source approach to in situ 2D Digital Image Correlation (DIC) applications. *SoftwareX*, *13*, 100645. <https://doi.org/10.1016/j.softx.2020.100645>
- der Klift, F. van, Koga, Y., Todoroki, A., Ueda, M., Hirano, Y., & Matsuzaki, R. (2016). 3D Printing of Continuous Carbon Fibre Reinforced Thermo-Plastic (CFRTP) Tensile Test Specimens. *Open Journal of Composite Materials*, *06*(01), 18–27. <https://doi.org/10.4236/ojcm.2016.61003>
- Díaz, J. G., León-Becerra, J., Pertuz, A. D., González-Estrada, O. A., & Jaramillo-Gutiérrez, M. I. (2021). Evaluation Through SEM Image Processing of the Volumetric Fiber Content in

- Continuous Fiber-Reinforced Additive Manufacturing Composites. *Materials Research*, 24(suppl 2). <https://doi.org/10.1590/1980-5373-mr-2022-0049>
- Díaz-Rodríguez, J. G., Pertúz-Comas, A. D., & González-Estrada, O. A. (2021). Mechanical properties for long fibre reinforced fused deposition manufactured composites. *Composites Part B: Engineering*, 211, 108657. <https://doi.org/10.1016/j.compositesb.2021.108657>
- Dickson, A. N., Barry, J. N., McDonnell, K. A., & Dowling, D. P. (2017). Fabrication of continuous carbon, glass and Kevlar fibre reinforced polymer composites using additive manufacturing. *Additive Manufacturing*, 16, 146–152. <https://doi.org/10.1016/j.addma.2017.06.004>
- Dickson, A. N., & Dowling, D. P. (2019). Enhancing the bearing strength of woven carbon fibre thermoplastic composites through additive manufacturing. *Composite Structures*, 212(December 2018), 381–388. <https://doi.org/10.1016/j.compstruct.2019.01.050>
- Dickson, A. N., Ross, K. A., & Dowling, D. P. (2018). Additive manufacturing of woven carbon fibre polymer composites. *Composite Structures*, 206(March), 637–643. <https://doi.org/10.1016/j.compstruct.2018.08.091>
- Dutra, T. A., Ferreira, R. T. L., Resende, H. B., Blinzler, B. J., & Larsson, R. (2020). Expanding puck and schurmann inter fiber fracture criterion for fiber reinforced thermoplastic 3D-printed composite materials. *Materials*, 13(7), 1–28. <https://doi.org/10.3390/ma13071653>
- Dutra, T. A., Ferreira, R. T. L., Resende, H. B., & Guimarães, A. (2019). Mechanical characterization and asymptotic homogenization of 3D-printed continuous carbon fiber-reinforced thermoplastic. *Journal of the Brazilian Society of Mechanical Sciences and Engineering*, 41(3), 1–15. <https://doi.org/10.1007/s40430-019-1630-1>

- Dutra, T., Ferreira, R. T. L., & Resende, H. (2018). Interlaminar shear strength of continuous carbon fiber reinforced thermoplastic composites manufactured by 3D printing. January 2017. *24th ABCM International congress of mechanical engineering, December*. <https://doi.org/10.26678/abcm.cobem2017.cob17-0282>.
- Eichenhofer, M., Maldonado, J. I., Klunker, F., Ermanni, P., Materials, C., Extrusion, F. C., Structures, F. F., & Composites, T. (2015). Analysis of Processing Conditions for a Novel 3D-. *20th International Conference on Composite Materials, July*, 19–24.
- Ferreira, R. T. L., Ashcroft, I. A., Li, S., & Zhuo, P. (2018). Optimisation of Fibre-Paths in Composites Produced by Additive Manufacturing. *EngOpt 2018 Proceedings of the 6th International Conference on Engineering Optimization*, 2, 1083–1094. https://doi.org/10.1007/978-3-319-97773-7_94
- Fidan, I., Imeri, A., Gupta, A., Hasanov, S., Nasirov, A., Elliott, A., Alifui-Segbaya, F., & Nanami, N. (2019). The trends and challenges of fiber reinforced additive manufacturing. *International Journal of Advanced Manufacturing Technology*, 102(5–8), 1801–1818. <https://doi.org/10.1007/s00170-018-03269-7>
- Focke, O., Bostan, L., Gaitzsch, R., Koerdt, M., Jansen, F., Meijer, F., Miene, A., Hesselbach, J., Lühns, H., Dimassi, A., Herrmann, A. S., & Ciacchi, L. C. (2018). Multiscale non-destructive investigations of aeronautic structures : from a single fiber to complex shaped fiber-reinforced composites. *8th Conference on Industrial Computed Tomography, iCT*, 1–7. <https://doi.org/10.1093/acprof:oso/9780195379440.001.0001>
- Galeja, M., Hejna, A., Kosmela, P., & Kulawik, A. (2020). Static and dynamic mechanical properties of 3D printed ABS as a function of raster angle. *Materials*, 13(2). <https://doi.org/10.3390/ma13020297>

- Garces, I. T., & Ayrançi, C. (2018). A view into additive manufactured electro-active reinforced smart composite structures. *Manufacturing Letters*, *16*, 1–5. <https://doi.org/10.1016/j.mfglet.2018.02.008>
- García Móstoles, F., Martínez Miranda, M. R., López, B., Fernández, E. G., Salas, A. T., & Jara, A. (2018). Análisis de ensayos de ILSS de probetas de material compuesto reforzadas con fibra continua producidas mediante impresión 3D. *Materiales Compuestos*, *2*, 97–101.
- Garland, A., & Fadel, G. (2018). Optimizing Topology and Gradient Orthotropic Material Properties Under Multiple Loads. *Journal of Computing and Information Science in Engineering*, *19*(2), 021007. <https://doi.org/10.1115/1.4041744>
- Gemi, L., Tarakçioğlu, N., Akdemir, A., & Şahin, Ö. S. (2009). Progressive fatigue failure behavior of glass/epoxy (± 75)₂ filament-wound pipes under pure internal pressure. *Materials and Design*, *30*(10), 4293–4298. <https://doi.org/10.1016/j.matdes.2009.04.025>
- Ghebretinsae, F., Mikkelsen, O., & Akessa, A. D. (2019). Strength analysis of 3D printed carbon fibre reinforced thermoplastic using experimental and numerical methods. *IOP Conference Series: Materials Science and Engineering*, *700*(1), 012024. <https://doi.org/10.1088/1757-899X/700/1/012024>
- Gibson, L. J., & Ashby, M. F. (1999). *Cellular Solids Structure and Properties* (2nd edition). Cambridge University Press.
- Goh, G. D., Dikshit, V., Nagalingam, A. P., Goh, G. L., Agarwala, S., Sing, S. L., Wei, J., & Yeong, W. Y. (2018). Characterization of mechanical properties and fracture mode of additively manufactured carbon fiber and glass fiber reinforced thermoplastics. *Materials and Design*, *137*, 79–89. <https://doi.org/10.1016/j.matdes.2017.10.021>

- Goh, G. D., & Yeong, W. Y. (2018). Mode I interlaminar fracture toughness of additively manufactured carbon fibre thermoplastic. *Proceedings of the International Conference on Progress in Additive Manufacturing, 2018-May*, 505–510. <https://doi.org/10.25341/D40015>
- González-Estrada, O. A., Pertuz, A., & Quiroga Mendez, J. E. (2018). Evaluation of Tensile Properties and Damage of Continuous Fibre Reinforced 3D-Printed Parts. *Key Engineering Materials*, 774(September), 161–166. <https://doi.org/10.4028/www.scientific.net/kem.774.161>
- Greenhalgh, E. S. (2009). *Failure analysis and fractography of polymer composites* (1st ed.). CRC Press.
- Guo, Q., Yao, W., Li, W., & Gupta, N. (2021). Constitutive models for the structural analysis of composite materials for the finite element analysis: A review of recent practices. *Composite Structures*, 260(August 2020), 113267. <https://doi.org/10.1016/j.compstruct.2020.113267>
- Habibi, M., & Laperrière, L. (2020). Digital image correlation and acoustic emission for damage analysis during tensile loading of open-hole flax laminates. *Engineering Fracture Mechanics*, 228, 106921. <https://doi.org/10.1016/j.engfracmech.2020.106921>
- Han, W. Q., Hu, K. J., Shi, Q. H., & Zhu, F. X. (2020). Damage evolution analysis of open-hole tensile laminated composites using a progress damage model verified by AE and DIC. *Composite Structures*, 247(May), 112452. <https://doi.org/10.1016/j.compstruct.2020.112452>
- Harilal, R., & Ramji, M. (2014). Adaptation of Open Source 2D DIC Software Ncorr for Solid Mechanics Applications. 9th International Symposium on Advanced Science and Technology in Experimental Mechanics, November, 1–6.

- Hart, R. J., Patton, E. G., Sapunkov, O., Patton, E. G., & Sapunkov, O. (2018). Characterization of Continuous Fiber-Reinforced Composite Materials Manufactured Via Fused Filament Fabrication (Report OPSEC1544). *Tardec Technical Report*
- Ho, C. M. B., Ng, S. H., & Yoon, Y. J. (2015). A review on 3D printed bioimplants. *International Journal of Precision Engineering and Manufacturing*, 16(5), 1035–1046. <https://doi.org/10.1007/s12541-015-0134-x>
- Hoa, S., Reddy, B., & Rosca, D. (2021). Development of omega stiffeners using 4D printing of composites. *Composite Structures*, 272(June), 114264. <https://doi.org/10.1016/j.compstruct.2021.114264>
- Hou, Z., Tian, X., Zhang, J., & Li, D. (2018). 3D printed continuous fibre reinforced composite corrugated structure. *Composite Structures*, 184(September 2017), 1005–1010. <https://doi.org/10.1016/j.compstruct.2017.10.080>
- Hou, Z., Tian, X., Zhang, J., Zhe, L., Zheng, Z., Li, D., Malakhov, A. v., & Polilov, A. N. (2020). Design and 3D printing of continuous fiber reinforced heterogeneous composites. *Composite Structures*, 237(August 2019), 111945. <https://doi.org/10.1016/j.compstruct.2020.111945>
- Hou, Z., Tian, X., Zheng, Z., Zhang, J., Zhe, L., Li, D., Malakhov, A. v., & Polilov, A. N. (2020). A constitutive model for 3D printed continuous fiber reinforced composite structures with variable fiber content. *Composites Part B: Engineering*, 189(February), 107893. <https://doi.org/10.1016/j.compositesb.2020.107893>
- Hu, Q., Duan, Y., Zhang, H., Liu, D., Yan, B., & Peng, F. (2018). Manufacturing and 3D printing of continuous carbon fiber prepreg filament. *Journal of Materials Science*, 53(3), 1887–1898. <https://doi.org/10.1007/s10853-017-1624-2>

- Hu, Y., & Cong, W. (2018). A review on laser deposition-additive manufacturing of ceramics and ceramic reinforced metal matrix composites. *Ceramics International*, 44(17), 20599–20612. <https://doi.org/10.1016/j.ceramint.2018.08.083>
- Iragi, M., Pascual-González, C., Esnaola, A., Lopes, C. S., & Aretxabaleta, L. (2019). Ply and interlaminar behaviours of 3D printed continuous carbon fibre-reinforced thermoplastic laminates; effects of processing conditions and microstructure. *Additive Manufacturing*, 30(September), 100884. <https://doi.org/10.1016/j.addma.2019.100884>
- Isobe, T., Tanaka, T., Nomura, T., & Yuasa, R. (2018). Comparison of strength of 3D printing objects using short fiber and continuous long fiber. *IOP Conference Series: Materials Science and Engineering*, 406(1). <https://doi.org/10.1088/1757-899X/406/1/012042>
- Justo, J., Távora, L., García-Guzmán, L., & París, F. (2018). Characterization of 3D printed long fibre reinforced composites. *Composite Structures*, 185(October 2017), 537–548. <https://doi.org/10.1016/j.compstruct.2017.11.052>
- Kabir, S. M. F., Mathur, K., & Seyam, A. F. M. (2020). A critical review on 3D printed continuous fiber-reinforced composites: History, mechanism, materials and properties. *Composite Structures*, 232(August 2019), 111476. <https://doi.org/10.1016/j.compstruct.2019.111476>
- Kachanov, L. M. (1986). Introduction to continuum damage mechanics (1st edition). Martinus NijHoff Publishers.
- Kim, F. H., Moylan, S. P., Phan, T. Q., & Garboczi, E. J. (2020). Investigation of the Effect of Artificial Internal Defects on the Tensile Behavior of Laser Powder Bed Fusion 17–4 Stainless Steel Samples: Simultaneous Tensile Testing and X-Ray Computed Tomography. *Experimental Mechanics*, 60(7), 987–1004. <https://doi.org/10.1007/s11340-020-00604-6>

- Kousiatza, C., Tzetzis, D., & Karalekas, D. (2019). In-situ characterization of 3D printed continuous fiber reinforced composites: A methodological study using fiber Bragg grating sensors. *Composites Science and Technology*, 174(November 2018), 134–141. <https://doi.org/10.1016/j.compscitech.2019.02.008>
- Kutner, M., Nachtsheim, C., Neter, J., & Li, W. (2005). *Applied linear statistical models* (5th Edition). McGraw-Hill.
- Kvalsvig, A., Yuan, X., Potgieter, J., & Cao, P. (2017). Analysing the tensile properties of 3D printed fibre reinforced thermoplastic composite specimens. *2017 24th International Conference on Mechatronics and Machine Vision in Practice, M2VIP 2017, 2017-Decem*, 1–6. <https://doi.org/10.1109/M2VIP.2017.8211514>
- Lapczyk, I., & Hurtado, J. A. (2007). Progressive damage modeling in fiber-reinforced materials. *Composites Part A: Applied Science and Manufacturing*, 38(11), 2333–2341. <https://doi.org/10.1016/j.compositesa.2007.01.017>
- León B., J., Díaz-Rodríguez, J. G., & González-Estrada, O. A. (2020). Daño en partes de manufactura aditiva reforzadas por fibras continuas. *Revista UIS Ingenierías*, 19(2), 161–175. <https://doi.org/10.18273/revuin.v19n2-2020018>
- Leon Becerra, S., González-Estrada, O., & Pertuz, A. (2017). Influence of the boundary condition on the first ply failure and stress distribution on a multilayer composite pipe by the finite element method. *J. Phys.: Conf. Ser.* 1159 012013.
- León-Becerra, J., González-Estrada, O. A., & Quiroga, J. (2021). Effect of Relative Density in In-Plane Mechanical Properties of Common 3D-Printed Polylactic Acid Lattice Structures. *ACS Omega*, 6(44), 29830–29838. <https://doi.org/10.1021/acsomega.1c04295>

- León-Becerra, J. S., González-Estrada, O. A., & Pinto-Hernández, W. (2020). Mechanical characterization of additive manufacturing composite parts. *Respuestas*, 25(2). <https://doi.org/10.22463/0122820x.2189>
- Li, N., Li, Y., & Liu, S. (2016). Rapid prototyping of continuous carbon fiber reinforced polylactic acid composites by 3D printing. *Journal of Materials Processing Tech.*, 238, 218–225. <https://doi.org/10.1016/j.jmatprotec.2016.07.025>
- Liravi, F., Das, S., & Zhou, C. (2015). Separation force analysis and prediction based on cohesive element model for constrained-surface Stereolithography processes. *CAD Computer Aided Design*, 69, 134–142. <https://doi.org/10.1016/j.cad.2015.05.002>
- Lizut, M., & Wojs, M. K. (2017). Research on clutch lever of KTM motorcycle produced by using 3D printing. *Proceedings of the Institute of Vehicles*, 4(113), 63–74.
- Luo, H., Tan, Y., Zhang, F., Zhang, J., Tu, Y., & Cui, K. (2019). Selectively Enhanced 3D Printing Process and Performance Analysis of Continuous Carbon Fiber Composite Material. *Materials*, 12(21), 3529. <https://doi.org/10.3390/ma12213529>
- Mahajan, C., & Cormier, D. (2015). 3D Printing of Carbon Fiber Composites With Preferentially Aligned Fibers. *Proceedings of the 2015 Industrial and Systems Engineering Reserach Conference*, 2953–2963.
- Maimí, P., Camanho, P. P., Mayugo, J. A., & Dávila, C. G. (2007a). A continuum damage model for composite laminates: Part I - Constitutive model. *Mechanics of Materials*, 39(10), 897–908. <https://doi.org/10.1016/j.mechmat.2007.03.005>
- Maimí, P., Camanho, P. P., Mayugo, J. A., & Dávila, C. G. (2007b). A continuum damage model for composite laminates: Part II - Computational implementation and validation. *Mechanics of Materials*, 39(10), 909–919. <https://doi.org/10.1016/j.mechmat.2007.03.006>

- Malakhov, A. v., Polilov, A. N., Zhang, J., Hou, Z., & Tian, X. (2020). A Modeling Method of Continuous Fiber Paths for Additive Manufacturing (3D Printing) of Variable Stiffness Composite Structures. *Applied Composite Materials*, 27(3), 185–208. <https://doi.org/10.1007/s10443-020-09804-8>
- Mark, G. T., & Gozdz, A. S. (2015). Three dimensional printer with composite filament fabrication (U.S. Patent No. 20180345572A1). U.S. Patent and Trademark Office
- Matsuzaki, R., Ueda, M., Namiki, M., Jeong, T. K., Asahara, H., Horiguchi, K., Nakamura, T., Todoroki, A., & Hirano, Y. (2016). Three-dimensional printing of continuous-fiber composites by in-nozzle impregnation. *Scientific Reports*, 6(December 2015), 1–7. <https://doi.org/10.1038/srep23058>
- Matzenmiller, A., Lubliner, J., & Taylor, R. L. (1995). A constitutive model for anisotropic damage in fiber-composites. *Mechanics of materials* 20, 125–152.
- Mehdikhani, M., Gorbatikh, L., Verpoest, I., & Lomov, S. v. (2019). Voids in fiber-reinforced polymer composites: A review on their formation, characteristics, and effects on mechanical performance. *Journal of Composite Materials*, 53(12), 1579–1669. <https://doi.org/10.1177/0021998318772152>
- Mei, H., Ali, Z., Ali, I., & Cheng, L. (2019). Tailoring strength and modulus by 3D printing different continuous fibers and filled structures into composites. *Advanced Composites and Hybrid Materials* 2(June), 312-319. <https://doi.org/10.1007/s42114-019-00087-7>
- Melenka, G. W., Cheung, B. K. O., Schofield, J. S., Dawson, M. R., & Carey, J. P. (2016a). Evaluation and Prediction of the tensile properties of continuous fiber-reinforced 3D structures. *Composite Structures*, 1–35. <https://doi.org/10.1037//0033-2909.126.1.78>

- Melenka, G. W., Cheung, B. K. O., Schofield, J. S., Dawson, M. R., & Carey, J. P. (2016b). Evaluation and prediction of the tensile properties of continuous fiber-reinforced 3D printed structures. *Composite Structures*, *153*, 866–875. <https://doi.org/10.1016/j.compstruct.2016.07.018>
- Meneses, G. A., Pereira, A., & Menezes, I. F. M. (2018). Lattice structures design by means of topology optimization. *Mecánica Computacional*, *2111*–2120.
- Miikki, K., Karakoç, A., Rafiee, M., Lee, D. W., Vapaavuori, J., Tersteegen, J., Lemetti, L., & Paltakari, J. (2021). An open-source camera system for experimental measurements. *SoftwareX*, *14*, 100688. <https://doi.org/10.1016/j.softx.2021.100688>
- Mohammadizadeh, M., Fidan, I., Allen, M., & Imeri, A. (2018). Creep behavior analysis of additively manufactured fiber-reinforced components. *International Journal of Advanced Manufacturing Technology*, *99*(5–8), 1225–1234. <https://doi.org/10.1007/s00170-018-2539-z>
- Mohammadizadeh, M., Imeri, A., Fidan, I., & Elkelany, M. (2019). 3D printed fiber reinforced polymer composites - Structural analysis. *Composites Part B: Engineering*, *175*(June), 107112. <https://doi.org/10.1016/j.compositesb.2019.107112>
- Montalvo Navarrete, J. I., Hidalgo-Salazar, M. A., Escobar Nunez, E., & Rojas Arciniegas, A. J. (2018). Thermal and mechanical behavior of biocomposites using additive manufacturing. *International Journal on Interactive Design and Manufacturing*, *12*(2), 449–458. <https://doi.org/10.1007/s12008-017-0411-2>
- Naranjo-Lozada, J., Ahuett-Garza, H., Orta-Castañón, P., Verbeeten, W. M. H., & Sáiz-González, D. (2019). Tensile properties and failure behavior of chopped and continuous carbon fiber

- composites produced by additive manufacturing. *Additive Manufacturing*, 26(December 2018), 227–241. <https://doi.org/10.1016/j.addma.2018.12.020>
- Ning, F., Cong, W., Hu, Y., & Wang, H. (2017). Additive manufacturing of carbon fiber-reinforced plastic composites using fused deposition modeling: Effects of process parameters on tensile properties. *Journal of Composite Materials*, 51(4), 451–462. <https://doi.org/10.1177/0021998316646169>
- Olufsen, S. N., Andersen, M. E., & Fagerholt, E. (2020). µDIC: An open-source toolkit for digital image correlation. *SoftwareX*, 11, 100391. <https://doi.org/10.1016/j.softx.2019.100391>
- Oztan, C., Karkkainen, R., Fittipaldi, M., Nygren, G., Roberson, L., Lane, M., & Celik, E. (2019). Microstructure and mechanical properties of three dimensional-printed continuous fiber composites. *Journal of Composite Materials*, 53(2), 271–280. <https://doi.org/10.1177/0021998318781938>
- Papon, E. A., Haque, A., & Mulani, S. B. (2019). Process optimization and stochastic modeling of void contents and mechanical properties in additively manufactured composites. *Composites Part B*, 177(February), 107325. <https://doi.org/10.1016/j.compositesb.2019.107325>
- Parandoush, P., & Lin, D. (2017). A review on additive manufacturing of polymer-fiber composites. *Composite Structures*, 182, 36–53. <https://doi.org/10.1016/j.compstruct.2017.08.088>
- Parrado-Agudelo, J. Z., & Narváez-Tovar, C. (2019). Mechanical characterization of polylactic acid, polycaprolactone and Lay-Fomm 40 parts manufactured by fused deposition modeling, as a function of the printing parameters. *ITECKNE*, 16(2), 25–31. <https://doi.org/10.15332/iteckne.v16i2.2354>

- Pascual-González, C., Iragi, M., Fernández, A., Fernández-Blázquez, J. P., Aretxabaleta, L., & Lopes, C. S. (2020). An approach to analyse the factors behind the micromechanical response of 3D-printed composites. *Composites Part B: Engineering*, *186*, 107820. <https://doi.org/10.1016/j.compositesb.2020.107820>
- Pertuz, A. D., Díaz-Cardona, S., & González-Estrada, O. A. (2020). Static and fatigue behaviour of continuous fibre reinforced thermoplastic composites manufactured by fused deposition modelling technique. *International Journal of Fatigue*, *130*, 105275. <https://doi.org/10.1016/j.ijfatigue.2019.105275>
- Pyl, L., Kalteremidou, K. A., & Van Hemelrijck, D. (2018). Exploration of specimen geometry and tab configuration for tensile testing exploiting the potential of 3D printing freeform shape continuous carbon fibre-reinforced nylon matrix composites. *Polymer Testing*, *71*(September), 318–328. <https://doi.org/10.1016/j.polymertesting.2018.09.022>
- Pyl, L., Kalteremidou, K. A., & van Hemelrijck, D. (2019). Exploration of the design freedom of 3D printed continuous fibre-reinforced polymers in open-hole tensile strength tests. *Composites Science and Technology*, *171*(June 2018), 135–151. <https://doi.org/10.1016/j.compscitech.2018.12.021>
- Quelho de Macedo, R., Ferreira, R. T. L., & Jayachandran, K. (2019). Determination of mechanical properties of FFF 3D printed material by assessing void volume fraction, cooling rate and residual thermal stresses. *Rapid Prototyping Journal*, *25*(10), 1661–1683. <https://doi.org/10.1108/RPJ-08-2018-0192>
- Raju, B., Hiremath, S. R., & Roy Mahapatra, D. (2018). A review of micromechanics based models for effective elastic properties of reinforced polymer matrix composites. *Composite Structures*, *204*, 607–619. <https://doi.org/10.1016/j.compstruct.2018.07.125>

- Ravindrababu, S., Govdeli, Y., Wong, Z. W., & Kayacan, E. (2018). Evaluation of the influence of build and print orientations of unmanned aerial vehicle parts fabricated using fused deposition modeling process. *Journal of Manufacturing Processes*, *34*, 659–666. <https://doi.org/10.1016/j.jmapro.2018.07.007>
- Ravindrababu, S., & Makam, R. (2018). Discrete homogenization of fused deposition modeling parts using the finite element method. *Proceedings of the International Conference on Progress in Additive Manufacturing*, 2018-May, 589–594. <https://doi.org/10.25341/D4TS39>
- Rodríguez, J. F., Thomas, J. P., & Renaud, J. E. (2003). Mechanical behavior of acrylonitrile butadiene styrene fused deposition materials modeling. *Rapid Prototyping Journal*, *9*(4), 219–230. <https://doi.org/10.1108/13552540310489604>
- Ruiz-Morales, J. C., Tarancón, A., Canales-Vázquez, J., Méndez-Ramos, J., Hernández-Afonso, L., Acosta-Mora, P., Marín Rueda, J. R., & Fernández-González, R. (2017). Three dimensional printing of components and functional devices for energy and environmental applications. *Energy & Environmental Science*, *10*(4), 846–859. <https://doi.org/10.1039/C6EE03526D>
- Sinha, S., & Meisel, N. A. (2018). Influence of process interruption on mechanical properties of material extrusion parts. *Rapid Prototyping Journal*, *24*(5), 821–827. <https://doi.org/10.1108/RPJ-05-2017-0091>
- Sumio, M. (2012). *Continuum Damage Mechanics* (G. G.M.L., Ed.). Springer.
- Swolfs, Y., & Pinho, S. T. (2016). Designing and 3D Printing Continuous Fibre-Reinforced Composites with a High Fracture Toughness. American Society for Composites *Thirty-First Technical Conference, October*.

- Swolfs, Y., & Pinho, S. T. (2019). 3D printed continuous fibre-reinforced composites: Bio-inspired microstructures for improving the translaminar fracture toughness. *Composites Science and Technology*, *182*, 107731. <https://doi.org/10.1016/j.compscitech.2019.107731>
- Tasch, D., Schagerl, M., Wazel, B., & Wallner, G. (2019). Impact behavior and fractography of additively manufactured polymers: Laser sintering, multijet fusion, and hot lithography. *Additive Manufacturing* (29). <https://doi.org/10.1016/j.addma.2019.100816>
- Tian, X., Liu, T., Wang, Q., Dilmurat, A., Li, D., & Ziegmann, G. (2017). Recycling and remanufacturing of 3D printed continuous carbon fiber reinforced PLA composites. *Journal of Cleaner Production*, *142*, 1609–1618. <https://doi.org/10.1016/j.jclepro.2016.11.139>
- Todoroki, A., Oasada, T., Mizutani, Y., Suzuki, Y., Ueda, M., Matsuzaki, R., & Hirano, Y. (2019). Tensile property evaluations of 3D printed continuous carbon fiber reinforced thermoplastic composites. *Advanced Composite Materials*, *29*(2), 1–16. <https://doi.org/10.1080/09243046.2019.1650323>
- Türk, D. A., Brenni, F., Zogg, M., & Meboldt, M. (2017). Mechanical characterization of 3D printed polymers for fiber reinforced polymers processing. *Materials and Design*, *118*, 256–265. <https://doi.org/10.1016/j.matdes.2017.01.050>
- Valvez, S., Santos, P., Parente, J. M., Silva, M. P., & Reis, P. N. B. (2020). 3D printed continuous carbon fiber reinforced PLA composites: A short review. *Procedia Structural Integrity*, *25*, 394–399. <https://doi.org/10.1016/J.PROSTR.2020.04.056>
- van de Werken, N., Hurley, J., Khanbolouki, P., Sarvestani, A. N., Tamijani, A. Y., & Tehrani, M. (2019). Design considerations and modeling of fiber reinforced 3D printed parts.

- Composites Part B: Engineering*, 160(December 2018), 684–692.
<https://doi.org/10.1016/j.compositesb.2018.12.094>
- van de Werken, N., Tekinalp, H., Khanbolouki, P., Ozcan, S., Williams, A., & Tehrani, M. (2020). Additively manufactured carbon fiber-reinforced composites: State of the art and perspective. *Additive Manufacturing*, 31, 100962.
<https://doi.org/10.1016/j.addma.2019.100962>
- Vignoli, L. L., Savi, M. A., Pacheco, P. M. C. L., & Kalamkarov, A. L. (2019). Comparative analysis of micromechanical models for the elastic composite laminae. *Composites Part B: Engineering*, 174, 106961. <https://doi.org/10.1016/j.compositesb.2019.106961>
- Vyas, G. M., & Pinho, S. T. (2012). Computational implementation of a novel constitutive model for multidirectional composites. *Computational Materials Science*, 51(1), 217–224.
<https://doi.org/10.1016/j.commatsci.2011.07.038>
- Warnung, L., Estermann, S., & Reisinger, A. (n.d.). Mechanical Properties of Fused Deposition Modeling (FDM) 3D Printing Materials. *RTEjournal - Fachforum Für Rapid Technologien*, 2018(1), 1–18. <https://www.rtejournal.de/ausgabe-15-2018/4781>
- Wei Zhu¹, C. Y., Jiayi Yang, S. W., & Shi, Y. (2015). Parameter Optimization for Preparing Carbon Fiber/Epoxy Composites by Selective Laser Sintering. *Symposium of 2015 Annual International Solid Freeform Fabrication*, 2–4.
- Wisnom, M. R. (1999). Size effects in the testing of fibre composite materials. *Composite Science and Technology*, 59, 1937–1957. [https://doi.org/10.1016/S0266-3538\(99\)00053-6](https://doi.org/10.1016/S0266-3538(99)00053-6)
- Xu, P., Zheng, J. Y., & Liu, P. F. (2009). Finite element analysis of burst pressure of composite hydrogen storage vessels. *Materials and Design*, 30(7), 2295–2301.
<https://doi.org/10.1016/j.matdes.2009.03.006>

- Yanamandra, K., Chen, G. L., Xu, X., Mac, G., & Gupta, N. (2020). Reverse engineering of additive manufactured composite part by toolpath reconstruction using imaging and machine learning. *Composites Science and Technology*, 198(June), 108318. <https://doi.org/10.1016/j.compscitech.2020.108318>
- Yang, D., Wu, K., Wan, L., & Sheng, Y. (2017). A Particle Element Approach for Modelling the 3D Printing Process of Fibre Reinforced Polymer Composites. *Journal of Manufacturing and Materials Processing*, 1(1), 10. <https://doi.org/10.3390/jmmp1010010>
- Yurgartis, S. W. (1987). Measurement of small angle fiber misalignments in continuous fiber composites. *Composites Science and Technology*, 30(4), 279–293. [https://doi.org/10.1016/0266-3538\(87\)90016-9](https://doi.org/10.1016/0266-3538(87)90016-9)
- Zare-Rami, K., & Kim, Y.-R. (2019). MIDAS-VT-Pre: Software to generate 2D finite element model of particle/fiber embedded composites with cohesive zones. *SoftwareX*, 10, 100292. <https://doi.org/10.1016/j.softx.2019.100292>
- Zhan, Z., & Li, H. (2021). A novel approach based on the elastoplastic fatigue damage and machine learning models for life prediction of aerospace alloy parts fabricated by additive manufacturing. *International Journal of Fatigue*, 145(December 2020), 106089. <https://doi.org/10.1016/j.ijfatigue.2020.106089>
- Zhang, J., Wang, P., & Gao, R. X. (2019). Deep learning-based tensile strength prediction in fused deposition modeling. *Computers in Industry*, 107, 11–21. <https://doi.org/10.1016/j.compind.2019.01.011>
- Zhang, Y., Qiao, J., Zhang, G., Li, Y., & Li, L. (2021). Prediction of deformation and failure behavior of continuous fiber reinforced composite fabricated by additive manufacturing.

Composite Structures, 265(February), 113738.

<https://doi.org/10.1016/j.compstruct.2021.113738>

Zhang, Z., Shi, J., Yu, T., Santomauro, A., Gordon, A., Gou, J., & Wu, D. (2020). Predicting flexural strength of additively manufactured continuous carbon fiber- reinforced polymer composites using machine learning. *Journal of Computing and Information Science in Engineering*, 20(6), 1–9. <https://doi.org/10.1115/1.4047477>

Zhao, L., Li, Y., Zhang, J., Zhou, L., & Hu, N. (2018). A novel material degradation model for unidirectional CFRP composites. *Composites Part B: Engineering*, 135, 84–94. <https://doi.org/10.1016/j.compositesb.2017.09.038>

Zhou, W. D., & Chen, J. S. (2018). 3D printing of carbon fiber reinforced plastics and their applications. *Materials Science Forum*, 913, 558–563. <https://doi.org/10.4028/www.scientific.net/MSF.913.558>

Ziemian, C. W., Ziemian, R. D., & Haile, K. v. (2016). Characterization of stiffness degradation caused by fatigue damage of additive manufactured parts. *JMADE*, 109, 209–218. <https://doi.org/10.1016/j.matdes.2016.07.080>

Annexes

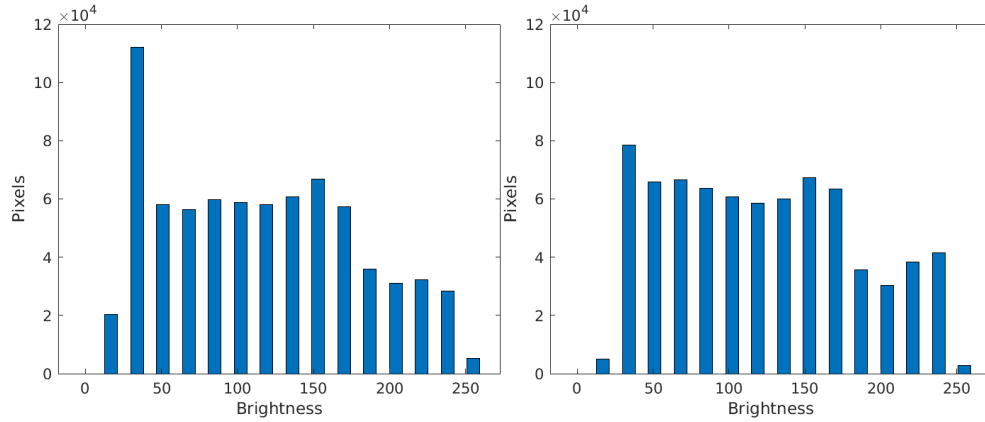
Appendix A. Python script for composite mechanics and data repository.

All the python scripts and raw data can be found in the attached compressed folder appendixA.zip

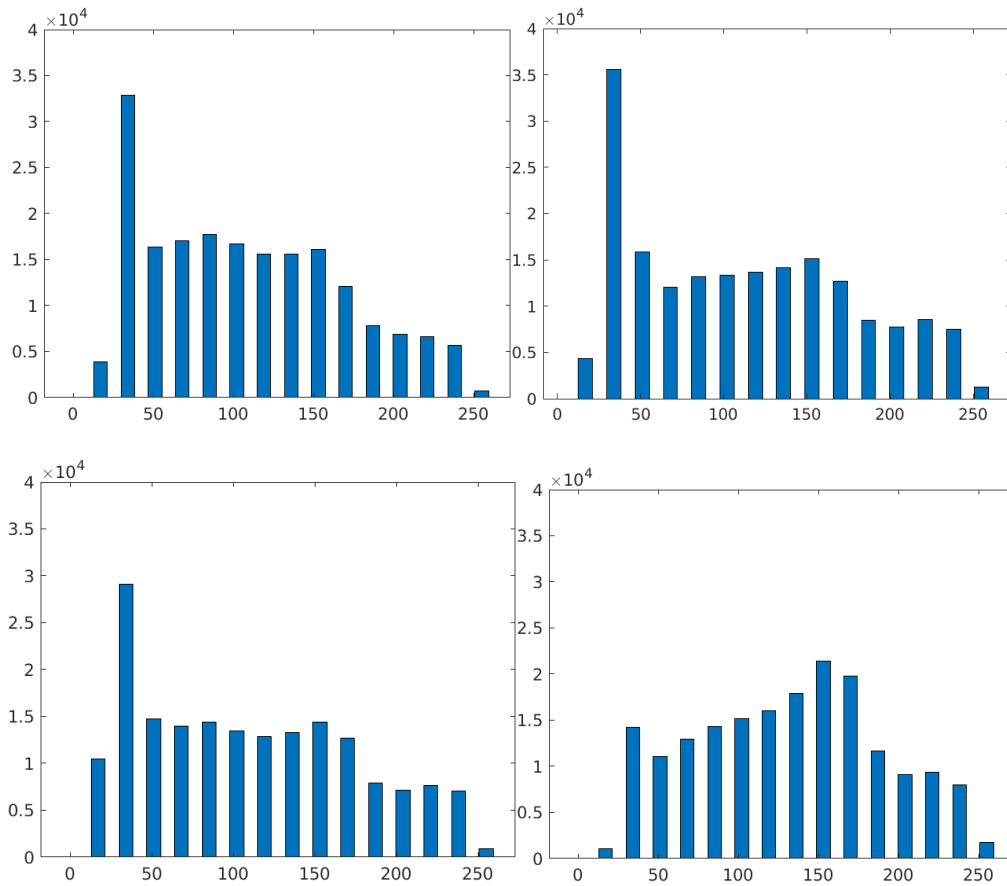
Appendix B. Histograms of the selected micrographs

In this appendix, the histograms of the reinforcements images are presented. In order to have a suitable RVE, all the histograms must be similar

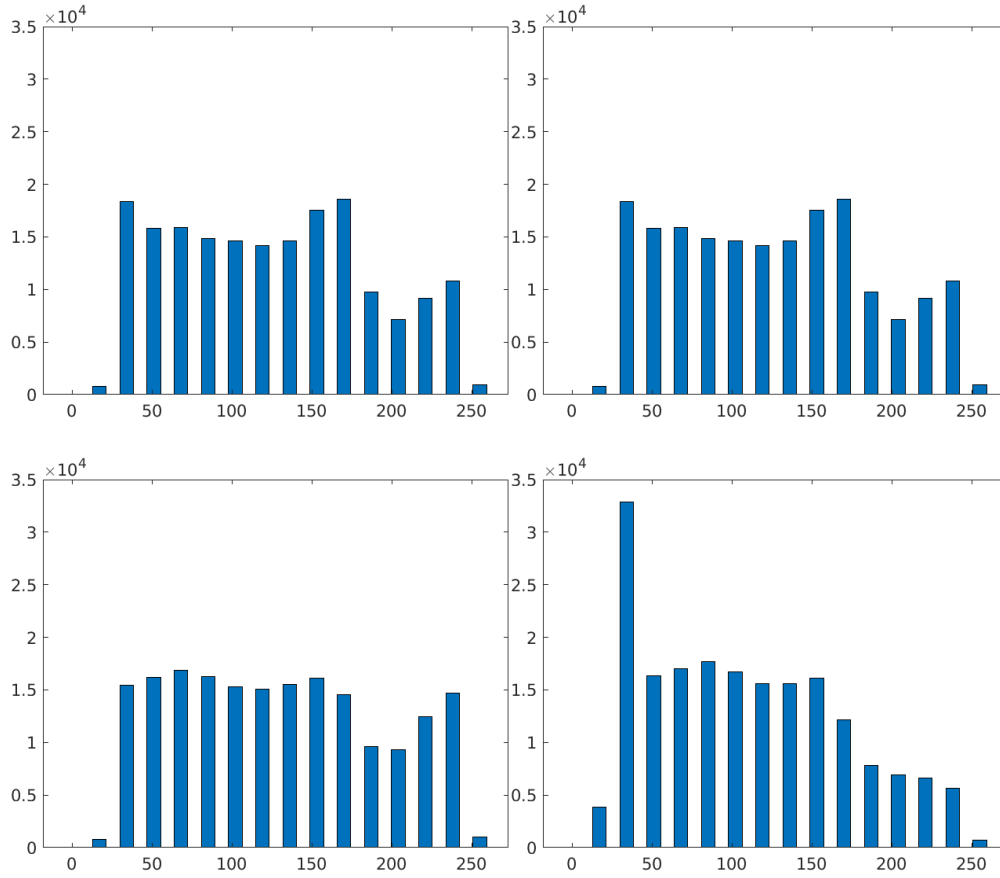
Continuous carbon fiber composites (big – two zones)



Continuous carbon fiber composites (medium-sized histograms)



Continuous carbon fiber composites (small-sized histograms)



Appendix C. Markforged materials datasheet

MATERIAL DATASHEET



Composites

Plastic Matrix	Test (ASTM)	Onyx	Onyx FR	Nylon W
Tensile Modulus (GPa)	D638	1.4	1.3	1.7
Tensile Stress at Yield (MPa)	D638	36	29	51
Tensile Strain at Yield (%)	D638	25	33	4.5
Tensile Stress at Break (MPa)	D638	30	31	36
Tensile Strain at Break (%)	D638	58	58	150
Flexural Strength (MPa)	D790 ¹	81	79	50
Flexural Modulus (GPa)	D790 ¹	3.6	4.0	1.4
Heat Deflection Temp (°C)	D648 B	145	145	41
Flame Resistance	UL94	—	V-0 ²	—
Izod Impact - notched (J/m)	D256-10 A	330	—	110
Density (g/cm ³)	—	1.2	1.2	1.1

Dimensions and Construction of Plastic Test Specimens:

- Tensile test specimens: ASTM D638 type IV beams
- Flexural test specimens: 3-pt. Bending, 4.5 in (L) x 0.4 in (W) x 0.12 in (H)
- Heat-deflection temperature at 0.45 MPa, 66 psi (ASTM D648-07 Method B)

All Markforged composite machines are equipped to print Onyx. Nylon White is available on the Mark Two and X7. Onyx FR is available on X3, X5, and X7.

Markforged parts are primarily composed of plastic matrix. Users may add one type of fiber reinforcement in each part, enhancing its material properties.

1. Measured by a method similar to ASTM D790. Thermoplastic-only parts do not break before end of flexural test.

2. Onyx FR is UL 94 V-0 Blue Card certified down to a thickness of 3mm.

Fiber Reinforcement	Test (ASTM)	Carbon	Kevlar*	Fiberglass	HSHT FG
Tensile Strength (MPa)	D3039	800	610	590	600
Tensile Modulus (GPa)	D3039	60	27	21	21
Tensile Strain at Break (%)	D3039	1.5	2.7	3.8	3.9
Flexural Strength (MPa)	D790 ¹	540	240	200	420
Flexural Modulus (GPa)	D790 ¹	51	26	22	21
Flexural Strain at Break (%)	D790 ¹	1.2	2.1	1.1	2.2
Compressive Strength (MPa)	D6641	320	97	140	192
Compressive Modulus (MPa)	D6641	54	28	21	21
Compressive Strain at Break (%)	D6641	0.7	1.5	—	—
Heat Deflection Temp (°C)	D648 B	105	105	105	150
Izod Impact - notched (J/m)	D256-10 A	960	2000	2600	3100
Density (g/cm ³)	—	1.4	1.2	1.5	1.5

Dimensions and Construction of Fiber Composite Test Specimens:

- Test plaques used in these data are fiber reinforced unidirectionally (0° Plies)
- Tensile test specimens: 9.8 in (L) x 0.5 in (H) x 0.048 in (W) (CF composites), 9.8 in (L) x 0.5 in (H) x 0.08 in (W) (GF and Kevlar* composites)
- Compressive test specimens: 5.5 in (L) x 0.5 in (H) x 0.085 in (W) (CF composites), 5.5 in (L) x 0.5 in (H) x 0.12 in (W) (Kevlar* and FG composites)
- Flexural test specimens: 3-pt. Bending, 4.5 in (L) x 0.4 in (W) x 0.12 in (H)
- Heat-deflection temperature at 0.45 MPa, 66 psi (ASTM D648-07 Method B)

Tensile, Compressive, Strain at Break, and Heat

Deflection Temperature data were provided by an accredited 3rd party test facility. Flexural data was prepared by Markforged, Inc. These represent typical values.

Markforged tests plaques are uniquely designed to maximize test performance. Fiber test plaques are fully filled with unidirectional fiber and printed without walls. Plastic test plaques are printed with full infill. To learn more about specific testing conditions or to request test parts for internal testing, contact a Markforged representative. All customer parts should be tested in accordance to customer's specifications.

Part and material performance will vary by fiber layout design, part design, specific load conditions, test conditions, build conditions, and the like.

This representative data were tested, measured, or calculated using standard methods and are subject to change without notice. Markforged makes no warranties of any kind, express or implied, including, but not limited to, the warranties of merchantability, fitness for a particular use, or warranty against patent infringement; and assumes no liability in connection with the use of this information. The data listed here should not be used to establish design, quality control, or specification limits, and are not intended to substitute for your own testing to determine suitability for your particular application. Nothing in this sheet is to be construed as a license to operate under or a recommendation to infringe upon any intellectual property right.

MATERIAL SPECIFICATIONS COMPOSITES



PLASTIC MATRIX	Test (ASTM)	Onyx	Nylon		
Tensile Modulus (GPa)	D638	1.4	0.94		
Tensile Stress at Yield (MPa)	D638	36	31		
Tensile Strain at Yield (%)	D638	25	27		
Tensile Stress at Break (MPa)	D638	30	54		
Tensile Strain at Break (%)	D638	58	260		
Flexural Strength (MPa)	D790 ¹	81	32		
Flexural Modulus (GPa)	D790 ¹	2.9	0.84		
Heat Deflection Temp (°C)	D648 B	145	49		
Izod Impact - notched (J/m)	D256-10 A	330	1000		
Density (g/cm ³)	—	1.2	1.1		
<p>Dimensions and Construction of Plastic Test Specimens:</p> <ul style="list-style-type: none"> Tensile test specimens: ASTM D638 type IV beams Flexural test specimens: 3-pt. Bending, 4.5 in (L) x 0.4 in (W) x 0.12 in (H) Heat-deflection temperature at 0.45 MPa, 66 psi (ASTM D648-07 Method B) <p>All Markforged machines are equipped to print Onyx. Nylon is a specialized material that can only be printed on the Mark Two and X7. Machines that print Onyx cannot also print Nylon due to machine conditioning.</p> <p>Markforged parts are primarily composed of plastic matrix. Users may add one type of fiber reinforcement in each part, enhancing its material properties.</p> <p>1. Measured by a method similar to ASTM D790. Thermoplastic-only parts do not break before end of Flexural Test.</p>					
FIBER REINFORCEMENT	Test (ASTM)	Carbon	Kevlar®	Fiberglass	HSHT FG
Tensile Strength (MPa)	D3039	700	610	590	600
Tensile Modulus (GPa)	D3039	54	27	21	21
Tensile Strain at Break (%)	D3039	1.5	2.7	3.8	3.9
Flexural Strength (MPa)	D790 ¹	470	190	210	420
Flexural Modulus (GPa)	D790 ¹	51	26	22	21
Flexural Strain at Break (%)	D790 ¹	1.2	2.1	1.1	2.2
Compressive Strength (MPa)	D6641	320	97	140	192
Compressive Modulus (MPa)	D6641	54	28	21	21
Compressive Strain at Break (%)	D6641	0.7	1.5	—	—
Heat Deflection Temp (°C)	D648 B	105	105	105	150
Izod Impact - notched (J/m)	D256-10 A	960	2000	2600	3100
Density (g/cm ³)	—	1.4	1.2	1.5	1.5

Dimensions and Construction of Fiber Composite Test Specimens:

- Test plaques used in these data are fiber reinforced unidirectionally (0° Plies)
- Tensile test specimens: 9.8 in (L) x 0.5 in (H) x 0.048 in (W) (CF composites), 9.8 in (L) x 0.5 in (H) x 0.08 in (W) (GF and Kevlar® composites)
- Compressive test specimens: 5.5 in (L) x 0.5 in (H) x 0.085 in (W) (CF composites), 5.5 in (L) x 0.5 in (H) x 0.12 in (W) (Kevlar® and GF composites)
- Flexural test specimens: 3-pt. Bending, 4.5 in (L) x 0.4 in (W) x 0.12 in (H)
- Heat-deflection temperature at 0.45 MPa, 66 psi (ASTM D648-07 Method B)

Tensile, Compressive, Strain at Break, and Heat

Deflection Temperature data were provided by an accredited 3rd party test facility. Flexural data were prepared by Markforged, Inc. The above specifications were met or exceeded.

Markforged tests plaques are uniquely designed to maximize test performance. Fiber test plaques are fully filled with unidirectional fiber and printed without walls. Plastic test plaques are printed with full infill. To learn more about specific testing conditions or to request test parts for internal testing, contact a Markforged representative.

Part and material performance will vary by fiber layout design, part design, specific load conditions, test conditions, build conditions, and the like.

This representative data were tested, measured, or calculated using standard methods and are subject to change without notice. Markforged makes no warranties of any kind, express or implied, including, but not limited to, the warranties of merchantability, fitness for a particular use, or warranty against patent infringement; and assumes no liability in connection with the use of this information. The data listed here should not be used to establish design, quality control, or specification limits, and are not intended to substitute for your own testing to determine suitability for your particular application. Nothing in this sheet is to be construed as a license to operate under or a recommendation to infringe upon any intellectual property right.

Appendix D. List of symbols by chapter

The arrays, tensors, and matrices are written in bolds and using square brackets, e.g., $[\mathbf{S}]$ is the compliance tensor, vectors are written in brackets and $\{\}$ in regular font, while scalars are written in Greek letters with no brackets. However, where the indicial notation is convenient, it is used and indicated.

Chapter 4.

ρ_s : Density of the bulk solid of a lattice structure

ρ^* : Density of the lattice structure

t : thickness of the lattice structure

l : length of the strut

E_s : Tensile modulus of the bulk solid.

G_s : Shear modulus of the solid.

E_1 : Elastic modulus in the longitudinal direction

E_2 : Elastic modulus in the transverse direction

E_3 : Elastic modulus in the out-of-plane direction

G_{12} : In plane shear modulus

H : Height

p_l : Porosity value

T : Thickness of the part

T_{layer} : Thickness of the layer

N_{floor} : Number of floor layers

W_{shell} : Width of the shell

l : Length

W : Width

V : Volume

V_f : Volumetric fraction

$[C]$: Elastic matrix

$[S]$: Compliance matrix

$[T]$: Transformation matrix

F : Total force

F_m : Force supported by the matrix

F_f : Force supported by the fiber.

α : Misalignment Weibull distribution parameter

σ : Stress (Cauchy stress tensor)

ε : Strain

ε_m : Matrix strain

E_{eq} : Equivalent elastic modulus

A : Area

G_m : Shear modulus of the matrix

G_f : Shear modulus of the fiber

ν_m : Poisson ratio of the matrix

ν_f : Poisson ratio of the fiber

L_{const} : Length of constituents

L_{RVE} : Length of RVE

L_{macro} : Length of macrostructure (laminate, part)

V : Volume

F_{1T} : longitudinal tensile strength

F_{fT} : apparent fiber tensile strength

V_f : Volumetric fiber fraction

α_σ : standard deviation of fiber misalignment

F_{2T} : Transverse tensile strength

G_{IC} : fracture toughness in mode I

t_t : transition thickness

F_{2C} : transverse compressive strength

F_{mC} : apparent compressive strength of the matrix

C_v : Empirical factor

V_V : Volumetric void fraction

F_6 : In-plane shear strength

G_a : Axial shear modulus of the fiber

F_4 : Intralaminar shear strength

α_0 : Fracture plane angle

$\{N\}$: Vector of forces per unit length

$\{M\}$: Vector of moments per unit length

\bar{Q}_{ij} : Stiffness matrix

t_k : thickness of the kth layer

z_k : Z coordinate of the kth layer

Chapter 5.

$[X]$: Design matrix also called training matrix, data matrix or input matrix.

y : Output or response.

w : Coefficients of the variables in the model

ε : Associated error with the model

b : Bias value.

\hat{y} : Prediction value of the model.

f_k : The function associated with the kth training example

$\mathcal{L}(\hat{y}, y)$: Error function

$J(w, b)$: Cost function

G_C : Energy dissipated per unit area

σ_e : Equivalent stress

u_e : Equivalent displacement

u_e^f : Ultimate equivalent displacement.

Chapter 6.

$[\sigma]$: Stress tensor

$[C]$: Stiffness tensor

$[\varepsilon]$: Strain tensor

$[\dot{\sigma}]$: Stress rate tensor

$[\dot{C}]$: Stiffness rate tensor

$[\dot{\varepsilon}]$: Strain rate tensor

$[D]$: Damage matrix

$[\dot{D}]$: Damage rate matrix

$[L^d]$: Damage multiplier tensor per strain

f : failure criterion function

Y : Thermodynamic force tensor

$[D]_d$: Damage matrix (shows the d dépendance)

\dot{d}_{ij} : Damage rate variables

ϕ_i : Dissipation potentials

W : Free energy of anisotropic damaged material

$\tilde{\sigma}$: Effective stress tensor

g_v : Regularized energy dissipated per unit area

L_e : Equivalent length

x_{ref} : X position in the reference configuration

y_{ref} : Y position in the reference configuration

\tilde{x}_{cur_i} : Estimated X position in the current configuration

u_{rc} : X displacement from the reference to the current configuration

v_{rc} : Y displacement from the reference to the current configuration

P : Displacement vector

C_{CC} : Correlation coefficient.

C_{LS} : Least square coefficient.

f : Reference image function

g : Current image function

$[E]$: Green strain tensor

η : Viscosity factor

$\dot{\gamma}$: Strain rate

E' : Storage modulus, real part of the complex modulus

E'' : Loss modulus, imaginary part of the complex modulus

E^* : Complex modulus